AAPM REPORT NO. 85

TISSUE INHOMOGENEITY CORRECTIONS FOR MEGAVOLTAGE PHOTON BEAMS

Report of Task Group No. 65 of the Radiation Therapy Committee of the American Association of Physicists in Medicine

Members

Nikos Papanikolaou (Chair) University of Arkansas, Little Rock, Arkansas
Jerry J. Battista London Regional Cancer Centre, London, Ontario, Canada
Arthur L. Boyer Stanford University, Stanford, California
Constantin Kappas University of Thessaly, Medical School, Larissa, Hellas
Eric Klein Mallinckrodt Institute of Radiology, St. Louis, Missouri
T. Rock Mackie University of Wisconsin, Madison, Wisconsin
Michael Sharpe Princess Margaret Hospital, Toronto, Ontario, Canada
Jake Van Dyk London Regional Cancer Centre, London, Ontario, Canada

August 2004

Published for the
American Association of Physicists in Medicine
by Medical Physics Publishing

DISCLAIMER: This publication is based on sources and information believed to be reliable, but the AAPM, the editors, and the publisher disclaim any warranty or liability based on or relating to the contents of this publication.

The AAPM does not endorse any products, manufacturers, or suppliers. Nothing in this publication should be interpreted as implying such endorsement.

Further copies of this report ($15 prepaid) may be obtained from:

Medical Physics Publishing
4513 Vernon Blvd.
Madison, WI 53705-4964
Telephone: 1-800-442-5778 or
608-262-4021
Fax: 608-265-2121
Email: mpp@medicalphysics.org
Web site: www.medicalphysics.org

International Standard Book Number: 1-888340-47-9
International Standard Serial Number: 0271-7344

Published by Medical Physics Publishing
4513 Vernon Boulevard, Madison, WI 53705-4964

Printed in the United States of America

TABLE OF CONTENTS

ABSTRACT

The human body consists of a variety of tissues and cavities with different physical and radiological properties. Most important among these, from a radiation dosimetry perspective, are tissues and cavities that are radiologically different from water, including lungs, oral cavities, teeth, nasal passages, sinuses, and bones. The dose distribution is affected by these tissue inhomogeneities and since treatments are becoming increasingly conformal, the opportunity for geographic misses of the target due to incorrect isodose coverage increases. In view of the inconsistent use of inhomogeneity corrections, the recent advances in the dose calculation algorithms, the improved 3D image acquisition and display capabilities, and the trend towards dose escalation in smaller target volumes, the Radiation Therapy Committee (RTC) of the American Association of Physicists in Medicine (AAPM) commissioned Task Group 65 (TG 65) to review this subject specifically for megavoltage photon beams. The specific objectives of this Task Group are: (a) to review the clinical need for inhomogeneity corrections and the currently available methodologies for tissue inhomogeneity corrections in photon beams; (b) to assess the known advantages and disadvantages of each of the currently available algorithms; (c) to make recommendations regarding the types of procedures that should be used to assess the accuracy of inhomogeneity correction procedures and the clinical application of specific inhomogeneity corrections for different anatomical regions. This report summarizes the findings of the Task Group and aims to provide the practicing clinical medical physicist with sufficient physical and mathematical insight into the inhomogeneity problem to be able to discern the capabilities and limitations of the particular method(s) available, to advise radiation oncologists as to the accuracy of the predicted doses and prescriptions, and to advise both so they are able to make informed decisions during the purchase of treatment planning systems.

I. INTRODUCTION

The human body consists of a variety of tissues and cavities with different physical and radiological properties. Most important among these, from a radiation dosimetry perspective, are tissues and cavities that are radiologically different from water, including lungs, oral cavities, teeth, nasal passages, sinuses and bones. In some instances, foreign materials, such as metallic prostheses, are also present. To maximize the therapeutic benefit of radiation therapy, it is essential that the absorbed dose delivered to all irradiated tissues in the presence of such inhomogeneities be predicted accurately.

Optimization of therapeutic benefit is dependent on maximizing the dose to the planning target volume while minimizing the dose to normal tissues. This optimization requires the accurate, three-dimensional localization of both the diseased target tissues and the sensitive normal tissues. In the last two decades, major progress in imaging technology has improved our ability to identify and to localize these critical volumes and to determine their densities *in vivo* on a voxel-by-voxel basis. Furthermore, radiation therapy treatment delivery systems have advanced to the point where volumes can be irradiated to millimeter precision. The combination of enhanced imaging procedures and beam modulation (aperture and intensity) techniques allow the radiation dose to be precisely conformed around the targeted tissues. One result of improved conformality is dose escalation studies in which the requirements/restrictions on the accuracy of the computed dose distributions are of even greater importance due to the potential for increased complication rates if the dose is inaccurately predicted.

The photon dose calculation problem is summarized in Figure 1. The accurate delivery of a prescribed dose to a well-defined target volume is dependent firstly on the accuracy with which the radiation beam can be calibrated under well-controlled reference conditions in a uniform water-like phantom (Figure 1a). Secondly, the dose at any point of interest within the patient must be calculated and correlated to the calibration dose. Figure 1b demonstrates some of the variables that must be considered in the photon beam dose calculation procedure, which is discussed below.

Until the 1970s, dose distributions were generally calculated by assuming that the patient was composed entirely of water. This was mainly due to the lack of patient-specific anatomical information. With the advent of computed tomography (CT), it became possible, for the first time, to actually derive electron density information *in vivo,* which could be incorporated into the dose calculation process. This, combined with tremendous advances in computer technology, resulted in much research with the aim of improving dose calculation procedures, which account for the complex physical processes associated with the irradiation of the heterogeneous human body.

Today, we are able to derive very precise three-dimensional information from a variety of imaging modalities including CT, magnetic resonance (MR), positron emission tomography (PET), single photon emission computed tomog-

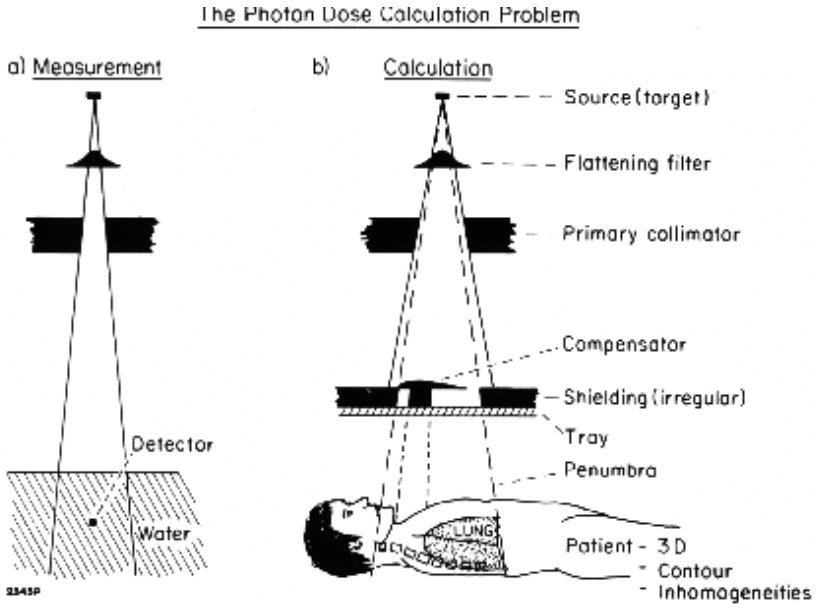

Figure 1. The photon dose calculation problem: (a) beam calibration in water and (b) calculation of the dose distribution in patient.

raphy (SPECT), digital angiography, and ultrasound. All this information can be processed for the improved delineation of diseased and normal tissues within the body. Computer workstations allow for the virtual simulation of the patient treatment by superimposing beam geometries at any orientation on the patient image set. This provides an environment for integrating 3D calculation and display tools into the treatment planning process.

Yet, in spite of this sophisticated technology, many radiation therapy departments have only achieved limited use of imaging data in the dose calculation process. In fact, many cancer centers still do not use patient-specific tissue density corrections. This may be due in part to the cost and effort of implementing new imaging technologies, limited access to these technologies in individual radiation therapy institutions, and the variability in the implementation and capabilities of tissue inhomogeneity corrections. These limitations complicate the standardization of dose delivery and contribute to uncertainties when comparing clinical outcomes, especially in the context of multi-center clinical trials. However, the judicious selection of proper calculation methods will improve dose standardization. Furthermore, dose coverage is also affected by tissue inhomogeneity, leading to additional variability. Because treatments are becoming increasingly conformal, the opportunity for geographic misses of the target due to incorrect isodose coverage prediction increases. This report will provide guidance to clinical physicists, dosimetrists, and radiation oncologists who aim

to improve the accuracy of absolu e dose prescriptions and dose distributions for the patient. The report assumes that the inhomogeneity corrections will be applied to patient-specific CT data and not to external, contour-based description of the patient.

In view of:

- the inconsistent use of inhomogeneity corrections,
- the recent advances in the dose calculation algorithms,
- improved 3D image acquisition and display capabilities, and
- the trend towards dose escalation in smaller target volumes,

the Radiation Therapy Committee (RTC) of the American Association of Physicists in Medicine (AAPM) commissioned Task Group 65 (TG 65) to review this subject specifically for megavoltage photon beams. The specific objectives of this Task Group were:

1. To review the clinical need for inhomogeneity corrections.
2. To review currently available methodologies for tissue inhomogeneity corrections in photon beams.
3. To assess the known advantages and disadvantages of each of the currently available algorithms.
4. To make broad recommendations on the use of inhomogeneity corrections in the clinical environment.

This report summarizes the findings of the Task Group and will provide the practicing medical physicist with sufficient physical and mathematical insight into the inhomogeneity problem to be able to discern the capabilities and limitations of the particular method(s) available, to advise radiation oncologists as to the accuracy of the predicted doses and correct prescriptions, and to advise both as to make informed decisions on the purchase of new treatment planning systems.

II. NEED FOR INHOMOGENEITY CORRECTIONS

A. Required Dose Accuracy

Radiation therapy is a complex process involving many steps with the accuracy of each step having a potential impact on tumor control or normal tissue complications. The sources of geometric and dosimetric uncertainties are known, but because of variations in tumor and normal tissue response, it is difficult to quantify the impact of these uncertainties in the clinical setting. A statement of the accuracy in dose required in clinical radiation therapy is generally predicated by four considerations:

1. The slope of dose-effect curves.
2. The level of dose differences that can be detected clinically.
3. Statistical estimates of the level of accuracy needed for clinical studies.
4. The level of dose accuracy that will be practically achievable.

1. Slopes of dose-effect curves

It is well established that both tumor control probabilities (TCP) and normal tissue complication probabilities (NTCP) have a sigmoidal dependence on radiation dose.[1,2,3,4,5] TCP and NTCP model calculations may be used in a relative manner to evaluate and optimize three-dimensional (3D) treatment plans.[6,7] Important parameters to describe the response are D_{50} (the dose yielding a response (TCP or NTCP) in 50% of a patient population), and the normalized dose gradient γ.[8] The parameters D_{50} and γ (or as it applies to the Linear Quadratic model the α/β ratio) are organ and injury (endpoint) specific and can be calculated only from clinical data. In general the D_{50} value for tumor control increases with tumor size while for normal tissue injury, it decreases with larger irradiated volumes.[9,10,11] There is a large variation in the reported slopes of dose-effect curves for the different tumors and normal tissues depending on their separate radiobiological characteristics. However, it has been extensively reported that the slopes of the dose-response curves appear to be steeper for normal tissues than for tumors, which mainly stems from their differences in their intrinsic radiobiology and internal structural organizations.[5,8,12,13] The delayed introduction of radiobiological treatment planning in the clinical routine stems from the fact that there are significant problems in the determination of the actual parameters to be used in the models[14,15] but also the foundations of the biological models that at present are subject to some controversy.[16] To improve the state of the art, high accuracy and quality must also be enforced in dose reporting.[17,18] In an attempt to quantify the actual accuracy needed, Boyer and Schultheiss[19] studied the influence of dose uncertainty on complication-free tumor control and concluded that a 1% accuracy improvement results in 2% increase in cure rate for early stage tumors. While the importance of dosimetric accuracy depends on the absolute dose delivered (i.e., the region of the dose-effect curve), the mid-range represents the steepest portion of this curve and will require the greatest dosimetric accuracy. At this point, a 5% change in dose may result in a 10% to 20% change in tumor control probability at a TCP of 50%. Similarly, a 5% change in dose may result in a 20% to 30% impact on complication rates in normal tissues. The results mentioned above refer to changes caused by homogeneous dose distributions covering the whole tumor or organ at risk considered, which is characterized by certain D_{50} and γ values. Nevertheless, they demonstrate the potential impact that a certain change in dose to the clinical outcome may have.

2. The level of dose differences that can be detected clinically

At least two examples[20] have been reported where a 7% difference in dose delivered to different groups of patients was discovered independently by a radiation oncologist through clinical observations. Two experiences from the Institut Gustave Roussy are reported: one was related to tumor regression, the other related to normal tissue reactions.

The first study (carried out in the early sixties) was intended to demonstrate that high-energy photons or electrons give the same effects on tumors for the same dose. Patients with squamous cell carcinoma of the tonsil were randomized and three observers recorded the tumor regression during the treatment. They reported a significant difference between electron and photon treatments nominally identical in dose (18 fractions of 2.5 Gy in 40 days). The small number of patients (20) that was studied in each arm of the trial was enough to show a definitely smaller efficiency of the electron treatment. This led to the discontinuation of the trial. A new calibration of the dosimetry for both photons and electrons was achieved with ferrous sulphate during the following months and showed for the high-energy calibration, a departure from the cobalt-60 calibration that had been used during the trial. The new calibration led to a 7% difference between the doses of electrons and photons. This could explain the difference observed in tumor regression between the two kinds of treatment.

The second experience was described in an internal report as follows: The radiotherapist (i.e., radiation oncologist) in charge of gynecological patients treated with high-energy photons (25 MV) on the Sagittaire (CGR MeV linac) mentioned to the physics department that he suspected an error in dosimetry because he observed reactions on patients which were more severe than usual. These were skin reactions on the skin folds and also diarrhea in patients irradiated to a prescribed tumor dose equal to 50 Gy to the whole pelvis 5 times a week for 5 weeks. After a careful rechecking of the linac, the physics department found an underestimation of the calibration factors of the monitor chamber leading to a systematic overdosage of the patients; the reason was the misuse by a junior physicist of the correction factors applied to the ionization chamber. The overdosage was estimated to be 10% between September and November 1970 and 7% between November 1970 and March 1971. The number of patients who had been overdosed for a part or for the full course of their treatment was 21 between September and November 1970 and 67 between November 1970 and March 1971. Fifty patients out of the eighty-eight overdosed had finished their treatment course over 2 months before the radiotherapist (i.e., radiation oncologist) suspected the error. No striking reaction was observed on the other (non-gynecological) patients.

Thus it could be concluded that at least a 7% difference in dose delivered is manifested in the patient's response to radiation treatment and is detectable clinically by a radiation oncologist.

3. The level of accuracy needed for clinical studies

The level of dose accuracy required for clinical trials depends on the ability to demonstrate a statistically significant improvement in clinical outcome as the dose is altered. Some authors[5,8,13,21,22] have looked at the steepness of dose-effect curves to estimate the required accuracy (as discussed above) while others have

analyzed dose distributions and treatment plans done with and without inhomogeneity corrections in lung.[23,24,25,26,27]

A side benefit but important consequence of including inhomogeneity corrections is the impact on the number of patients required in clinical trials. Orton and co-workers[28] have evaluated the difference in the number of patients required to demonstrate a statistically significant difference in the probability of tumor control (TCP) between two arms of a dose-escalation study and its dependence on the level of uncertainty in delivered dose. They have demonstrated the importance of making lung corrections even if the correction algorithms are not absolutely accurate. They presented the case of a dose-escalation study where inhomogeneities are present and no correction is applied (example 1) and when approximate correction is applied (example 2). For both examples it is assumed that a 10% change in TCP results from a 5% change in dose. Further, it is assumed that the standard error in TCP is 10%.

In the first example (no correction) an extra standard error in TCP due to lung attenuation is added which is also 10% (equivalent to a 5% standard error in dose). Then the overall standard error is $\left(10\sqrt{2}\right)\%$, since standard errors propagate in quadrature, i.e. the standard error in observed TCP is increased by a factor of $\sqrt{2}$ due to lung attenuation variations. Hence, for the same confidence level, the new number of patients required n' is given by $n' = a^2 n$, where a is the overall standard error and n the initial number of patients required. In this example $n' = 2n$, i.e., twice as many patients are needed in order to discriminate between the control probabilities in each arm of the clinical study.

In the second example (approximate correction) it is assumed that the approximate lung correction reduces the additional standard error in TCP due to lung attenuation from 10% to 5%, the overall standard deviation reduces from $\left(10\sqrt{2}\right)\%$ to $\left(10\sqrt{1.25}\right)\%$. Hence $n' = 1.25n$, i.e., only 25% more patients are needed.

Furthermore, inhomogeneity corrections reduce the uncertainty in absolute dose, yielding a more controlled study with less variability in absolute dose delivery. Thus far, two clinical trials for the treatment of lung cancer have been performed through the Radiation Therapy Oncology Group (RTOG):

- The RTOG-8808[29] trial, which closed in 1993, required treatment plans to be performed with a retrospective heterogeneity correction. These patients were treated, however, according to prescriptions and dose distributions based on dose in water. The isodose calculations were then repeated with heterogeneity corrections and absolute dose distributions were computed using the homogeneous dose prescriptions in water. In addition, an independent calculation of delivered dose to the isocenter using the Batho correction method was performed. Of the 490 patients enrolled, a total of 322 patients have been documented in this manner. This study found that for all fields the mean inhomogeneity correction factor at the isocenter was 1.05±0.05 (SD) with an overall range of 0.95 to 1.28, i.e., a 33% spread in the dose delivered (an inhomogeneity correction factor is applied to

make adjustments to the uncorrected distribution to account for variations in tissue density).

- In the RTOG 88-08 study, the treatment plans were however limited to a single central plane. The RTOG[30] initiated a three-dimensional (3D) treatment planning study for lung cancer. RTOG 93-11 is a dose escalation study that is similar to RTOG 8808, requiring institutions to submit uncorrected and corrected dose distributions. Again, the patients were treated according to uncorrected treatment plans. Doses are taken to the maximum level of 90.3 Gy based on calculations for water. RTOG 93-11 will then provide additional information in the 3D context. Clearly, the correct implementation of inhomogeneity corrections methods can reduce the dose uncertainty, remove ambiguity in the interpretation of outcomes, and subject fewer patients to clinical trials.

Earlier reports that are not based on clinical trials data also cite specific numerical examples of the effects of inhomogeneity corrections on dose. Mah and Van Dyk[23] previously reviewed, quantitatively, dose distributions for 100 patients who had thoracic irradiation for a variety of malignancies. The general conclusions were:

(1) within lung, correction factors are significant in the majority of patients,
(2) within the target volume, correction factors can also be quantitatively significant for many situations,
(3) dose uniformity in lung is worse when the distributions are corrected for inhomogeneities, and
(4) in approximately 80% of the patients studied, the probability of radiation-induced lung damage would be underestimated by at least 5% if lung corrections were not applied. These conclusions are consistent with the later review of the RTOG trials data.

In the literature many authors cite reasons for and against the use of lung corrections.[23,24,25,26,28,31] It has been argued by some that tissue inhomogeneity corrections should not be used at all since current clinical practice and dose prescriptions are largely based on historical experience with tissue response to dose in water. However, the clinical data above indicate that even for simple anterior-posterior parallel-opposed fields encompassing the mediastinum and lung regions, the corrections at the reference target point could range between 0.95 and 1.16, and are even larger for oblique or lateral fields. Because the entire dose distribution can be distorted by tissue inhomogeneity, not only is the dose to the target volume affected, but also so are the doses to nearby organs at risk. For example, the dose to the spinal cord will increase due to lung transmission, and simultaneously decrease due to absorption of surrounding upstream vertebral bodies, and further decrease because of the decreased scatter due to the adjacent low-density lung.

Today, many dose escalation clinical trials limit the target dose levels according to the dose to organs at risk. Therefore accurate assessment of dose

distributions, in addition to absolute point dose, is vital. The proper choice and implementation of inhomogeneity corrections methods reduces the uncertainty, and allows dose prescriptions to be optimized for each patient accordingly. Furthermore, correction of the relative dose distributions is important for the optimization of the field size in achieving tumor coverage in conformal radiotherapy. For example in lung cancer, where there is an enlargement of the irradiated volume[32,33,34,35,36,37,38,39] caused by the excessive lateral diffusion of electrons [see section III.C.(b)], the field dimensions should be adjusted according to the dose distribution with inhomogeneity correction.

4. The level of dose accuracy that will be practically achievable

A statement of dose accuracy goals should be based on what is realistically achievable, in light of the magnitude and relative importance of all other uncertainties known at the present time. Various authors[5,8,20,40,41,42,43,44,45,46,47] have reviewed uncertainties associated with the dose delivered to the patient by examining the individual steps within the dose determination process. Their estimates are summarized in Table 1. It is important to appreciate the impact that different sources of error have on the overall uncertainty, excluding the dose calculation step. When 2% to 3% errors in the dose computation are factored into the total uncertainty, the overall error is ≅5% or larger. The above estimates are valid when a complete and comprehensive quality assurance (QA) program is followed. Larger errors should be expected when more complex treatment techniques are applied. However, with the anticipated reductions in overall uncertainties in the near future due to improved imaging and radiation

Table 1. Estimates of Uncertainty (in terms of one standard deviation) in absolute dose in the patient for the complete treatment procedure using megavoltage photons, today and in the future.

Source of Uncertainties	Uncertainty at Present (%)	Uncertainty in Future (%)
Dose at the calibration point in water	2.5	1.0
Additional uncertainty for other points	0.6	0.3
Beam Monitor stability	1.0	0.5
Beam flatness	1.5	0.5
Patient data	1.5	1.0
Patient set up and organ motion	2.5	2.0
Overall (excluding dose calculation)	4.3	2.5
Dose calculation algorithm (multiple levels)	1.0 / 2.0 / 3.0 / 5.0	1.0 / 2.0 / 3.0
TOTAL	4.4 / 4.7 / 5.2 / 6.6	2.7 / 3.2 / 3.9

technology, it becomes evident that even more accurate dose calculation algorithms will become desirable.

B. Recommended Accuracy in Tissue Inhomogeneity Corrections

As indicated in Table 1, there are many considerations in the uncertainty estimation of the dose delivered to the patient. Accepting that (in terms of one standard deviation) the present overall desired accuracy is 5% in the dose delivered to a volume (or point) and that it may be realistic to expect 3% to be achievable in the near future, then the accuracy of computed dose distributions should be between 1% to 2%. Since relative dose calculations have conventionally comprised two steps: (i) a calculation in a homogeneous medium, and (ii) a tissue inhomogeneity correction, each of these independent components, if divided evenly, would have to be determined with an uncertainty of less than 1.4%. For computational methods, which do not require an *a priori* calculation of dose in water, the overall uncertainty in the directly computed dose distribution should be less than 2%.

As will be shown later (in section V), this level of accuracy is very difficult to achieve with many existing algorithms. Some traditional methods produce systematic errors of much greater magnitude, (well in excess of 10% in the thorax for example), especially when charged particle equilibrium is not assured. However, this limitation should be balanced against the inadequacy of performing no corrections at all.

For situations other than lung, the clinical impact and need for accuracy has not been assessed as extensively. This is true for bone and various smaller cavities throughout the body. The effects of metallic prostheses are of particular interest due to their high attenuation characteristics and large dose interface effects. The AAPM report of Task Group 63[48] reviews and makes recommendations on the effects of metallic hip prostheses. While the overall clinical impact may not be well understood, the general principle of 3% accuracy in dose delivery with the corresponding need for better than 2% accuracy in correcting for inhomogeneities is a reasonable, albeit challenging, goal.

Clearly, the standardization of absolute dose delivery cannot be achieved if the uncontrolled variability caused by the anatomy, geometry, and density associated with individual patients is not accounted for. Accurate dose determination including inhomogeneity corrections is an essential component of dose optimization and the objective analysis of clinical results, especially with the advent of 3D precision conformal radiotherapy and with the extension of intensity-modulated radiation therapy (IMRT) treatments to structures that have not been irradiated before.

We now review the underlying radiation physics of tissue inhomogeneity corrections. This knowledge is especially important in understanding the strengths and limitations of the existing dose algorithms.

III. RADIATION PHYSICS RELEVANT TO PHOTON INHOMOGENEITY CALCULATIONS

This section provides a summary of the major physical processes that underlay the absorption of photon energy in different tissues. More details of the physics involved can be found in several excellent textbooks.[49,50] Our goal in this section is therefore only to summarize the key concepts to assess the basis, strengths, and limitations of tissue inhomogeneity calculations presented later. Our starting point is a spatial, spectral, and directional distribution of photon fluence entering the patient's surface as one would get from a Monte Carlo simulation of a treatment machine.[51,52,53]

The deposition of energy in tissue from a photon beam is fundamentally a two-step process:

(1) the photons interact in the medium to impart kinetic energy to charged particles (i.e., the TERMA step, see paragraph III.A.)
(2) charged particles then deposit their given energy through ionization and excitation events along a finite track (i.e., the DOSE step, see paragraph III.B.).

If charged particle equilibrium (CPE) is established, then there is a linear relationship between TERMA (total energy released per unit mass) and dose[49] and the two steps are effectively blended into a single calculation. However, if this condition does not hold (e.g., at tissue interfaces and beam edges), this simplification is invalid and the two steps must be more clearly distinguished.

A. Photon Interactions: The TERMA Step

The initial photon interactions within tissue are characterized by a linear attenuation coefficient (μ) which is the probability of a photon interacting per unit distance. This probability depends on: (i) the incident photon energy; E (MeV), (ii) the tissue density, ρ (g/cm^2); and (iii) the effective atomic number (Z) of the tissue.

In a therapeutic photon beam, a large number of photons are incident on the patient,[54] each with energy E (MeV). The ensemble of photons reaching a point in the patient is characterized by an energy fluence (MeV cm^{-2}).

For a given energy fluence, the total energy *released* per unit mass, TERMA[55] is given as the product of the total mass attenuation coefficient $\left(\frac{\mu}{\rho}\right)$ and the energy fluence (ψ) at a point.[56]

The kinetic energy released to *charged particles only* per unit mass is the KERMA (<TERMA), and the kinetic energy released and subsequently locally absorbed along the charged particle tracks per unit mass is the collision

$KERMA_c$ (<KERMA). Bremsstrahlung events are excluded since the photons produced do not deposit their energy locally.

These quantities are all related to the photon energy fluence by the mass attenuation, mass energy transfer, and mass energy absorption coefficients, respectively (Table 2).

The removal of photons from the radiation therapy beam is dominated by three competing interactions with the atoms of tissue: the photoelectric effect, the Compton effect and pair production. Figure 2 summarizes the **dominance** of the Compton effect for different photon energies and for absorbers with different atomic number (Z).

- In *water-like tissues* (Z = 7.5), the probability of Compton events dominates (>80%) for energies between 0.05 MeV and 10 MeV. Thus, accurate modeling of Compton scattering events is an essential ingredient of any method of inhomogeneity correction for megavoltage photon beams.
- For *higher atomic number materials*, such as bone (Z = 13), the energy range of Compton dominance is reduced (0.08 to 7 MeV). At orthovoltage and superficial therapy energies, the photoelectric effect is strongly dependent on atomic number ($\sim Z^3$), and thus the dose to bone relative to the dose to water will be **increased,** for a given photon fluence. Similarly, for x-ray energies between 10 and 25 MV the dose to bone is accentuated compared with water due to a higher incidence of pair production events.
- Similar considerations apply to *ultra-high atomic number materials* such as metallic prostheses implanted in the patient, except that, because of additional electrons set in motion with the metal,[48] the interest is focused at the tissue in the vicinity and shadow of the metal rather than the metal itself.

B. Charged Particle Interactions: The DOSE Step

All the photon interactions release some energy to recoil charged particles including photoelectrons, Compton electrons, and electron-positron pairs, which are ultimately responsible for energy deposition in tissue. The charged particles are launched with a spectrum of initial energies and directions. These particles then slow down through multiple Coulomb collisions, which deposit

Table 2. Interrelationships between radiation quantities.

Common units	**cm^{-1}**	**cm^2/g**	**MeV/g**
SI units	**m^{-1}**	**m^2/kg**	**Gy**
Attenuation	μ	μ/ρ	TERMA
Transfer	μ_{tr}	μ_{tr}/ρ	KERMA
Absorption	μ_{en}	μ_{en}/ρ	$KERMA_c$

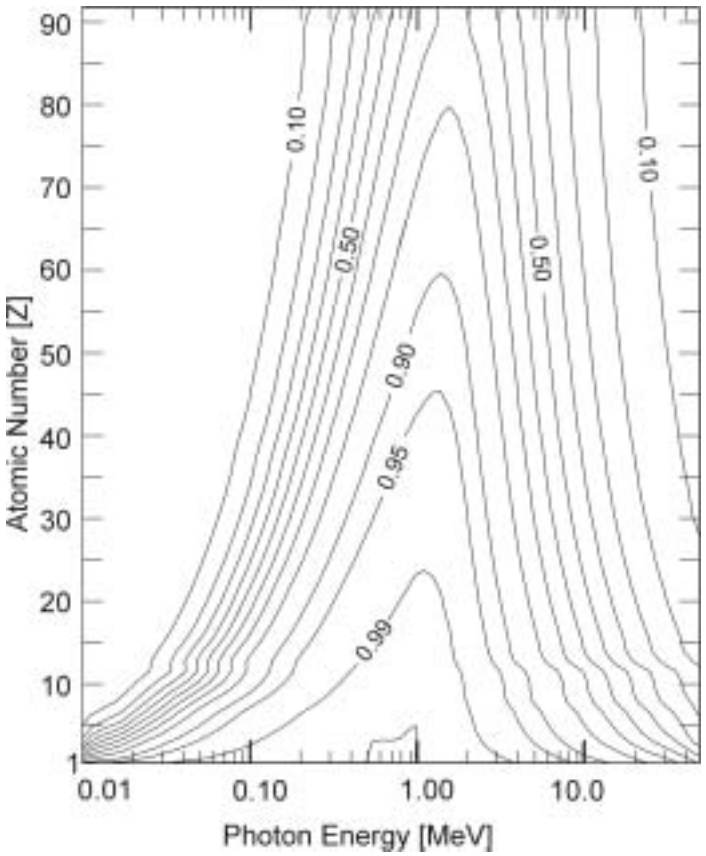

Figure 2. The fraction of interacting photons that undergo Compton scattering as a fraction of photon energy and the atomic number of the absorbing medium.

energy locally along the particle track and occasional radiative *bremsstrahlung* events that carry energy remotely away from the charged particle track. To include only local energy deposition, the mass collisional stopping power[49] is thus more relevant to the energy deposited locally along the path of a charged particle:

$$\frac{S_{col}}{\rho} = \frac{d\bar{E}}{\rho dl} \qquad \left(\frac{MeV \cdot cm^2}{g} \right) \tag{1}$$

where an average energy, $d\bar{E}$, is lost locally to the medium per unit density and per path length traversed, dl. The mass collisional stopping power depends on the energy and charge of the decelerating particle, and the atomic number of the stopping medium and is nearly density independent (see section III.D.1). In reality, charged particles lose a variable burst of energy for each interaction, but this statistical energy straggling[56,57] is often ignored and "continuous slowing down approximation (CSDA)" is assumed. This allows for the determination of a unique "CSDA range" of the charged particle:

$$R_{CSDA} = \int_0^E \left(\frac{d\bar{E}}{\rho dl} \right)^{-1} \cdot dE \qquad \left(\frac{g}{cm^2} \right) \tag{2}$$

In addition to slowing down, the charged particles are also deflected through multiple scattering events, which redirects their energy and changes their dose deposition patterns. This scattering is enhanced in higher atomic number materials. The detailed calculations of multiple scattering of electrons require complex analytical or Monte Carlo methods and these have been developed elsewhere for *electron* beams.[53,58,59,60,61,62,63,64,65,66,67] However, because secondary charged particles produced by photon beams are of lower energy than the photons and have relatively shorter ranges, a simpler treatment of electrons is often acceptable for photon beams. In the simplest models, recoil electrons are often assumed to be "absorbed on the spot" for low energy photon beams. For higher photon energies, the particle ranges are significantly longer (i.e., centimeters) and the spreading of the energy of charged particles launched by photons needs to be modeled (Table 3).

Table 3. Particle ranges and corresponding energies for different tissues and initial photon energies. σ_{tr} is the energy transfer cross section for the Compton effect and σ is the total energy cross section for the Compton effect.

Photon energy (MeV)	T_{max} (MeV)	R_{CSDA}(cm) muscle	lung	bone
1.25	0.59	0.23	0.92	0.14
2	1.06	0.44	1.76	0.26
4	2.4	1.2	4.8	0.72
6	3.86	1.9	7.6	1.16

assumes ρ_{lung}=0.25 g/cc, ρ_{bone}=1.85 g/cc

$$T_{max} = h\nu \cdot \frac{\sigma_{tr}}{\sigma}$$

C. Charged Particle Equilibrium

Charged particle equilibrium (CPE) occurs when there is a "steady state" between the charged particles entering and leaving a small region of dosimetric interest (in reference to the electron R_{CSDA} range). Equivalently, within a small volume of interest partial electron tracks can be paired to form complete ranges. The track segments are said to be complementary and the situation is as if the entire track energy were deposited on the spot.[68] Thus, if pure CPE holds, the primary dose (see equation 8) becomes exactly *equal* to the collision KERMA (Table 4). CPE is an energy balance in three-dimensional space. Pure equilibrium can develop if the photon fluence is sufficiently uniform in the vicinity of the sampling volume that charged particles are also released uniformly with a constant energy and angular spectrum. The surrounding shell of material must be uniform over a minimum thickness equal to the maximum range of charged particles launched therein by the photons from the point under consideration.

Satisfying the condition of uniform charged particle fluence is strictly *impossible* for photon beams because of beam divergence and photon attenuation.[69] For example, the extent of disequilibrium can be quantified by considering the photon attenuation along the beam direction over the maximum range of secondary electrons, as shown in Table 4.[49]

Fortunately, *transient* charged particle equilibrium (TCPE) is much easier to achieve than pure equilibrium.[49] In brief, TCPE is achievable along the central ray in a uniform absorber at depths which exceed the maximum forward range of the particles launched, provided the half-width of the radiation field also exceeds their maximum lateral motion (i.e., lateral equilibrium). In this case, the beam attenuation can cause a systematic shift between collision KERMA and dose: the absorbed dose becomes *proportional* to (but not equal to) the collision KERMA (as in Table 4). For CPE and TCPE, a calculation of dose is greatly simplified since it requires no detailed tracking of electron trajectories. Many of the simpler methods of inhomogeneity correction assume implicitly CPE or TCPE and thus avoid dealing with the complexity of charged particle transport.

Table 4. Parameters related to achieving charged particle equilibrium (CPE).

Incident photon energy [MeV]	Photon attenuation [%] in thickness of medium equal to maximum electron range	Mean depth of energy deposition, $\bar{x}$ [cm]	Ratio of Primary Dose to collision KERMA
0.1	0	0.000853	1.000146
1	1	0.0768	1.00545
10	7	1.60	1.0365
30	15	4.53	1.082

As noted earlier, CPE is a three-dimensional phenomenon. For simplicity here, we have separated its components into the longitudinal direction along the beam axis and in the lateral directions perpendicular to the beam axis.

1. Longitudinal TCPE

First consider the familiar build-up dose along the central ray of a broad beam of megavoltage photons for a beam sufficiently large to achieve lateral equilibrium. The fluence of charged particles builds up to a maximum at a depth equal to the most probable range of the charged particles, R_p. Beyond the maximum range of charged particles, R_{max}, only TCPE exists and the dose exceeds the collision KERMA because the energy launched by photons is actually deposited downstream by an off-set distance, $\bar{x}$. The proportionality constant (ratio of dose to kerma) is a scalar larger than unity for points along the central axis (beyond d_{max}) of a beam incident on a uniform water absorber and is given in column 4 of Table 4. A simple way to relate primary dose to collision KERMA (beyond d_{max}) in a uniform absorber is to use[70,71]:

$$D_P(x) = e^{\mu\bar{x}} K_c(x) \approx (1 + \mu\bar{x}) \cdot K_c(x) \tag{3}$$

where $D_p(x)$ is the primary dose and $K_c(x)$ is the collision KERMA at depth x, and the exponential term corrects for the downstream attenuation along the mean distance between energy launch and energy deposition points. Table 4 lists some representative values for and for the resultant proportionality constant for monoenergetic primary photons interacting in water.[72]

For shallow depths less than d_{max}, where disequilibrium is obvious, the transport of charged particles must be explicitly taken into account. Considering only the primary dose for the moment, ignoring beam contamination, and assuming a field size large enough to achieve lateral CPE (see section 2. below), the depth-dose curve can be obtained through a convolution of the collision KERMA with the spread of electron energy.[73]

$$D_P(x) = N \int_0^x K_c e^{-\mu x'} \beta e^{-\beta(x - x')} dx' \tag{4}$$

where:

D_P is the primary dose as a function of depth, x.

N is a dose normalization factor

K_c is the incident collision $KERMA_c$, which is attenuated exponentially with depth, x, according to μ, the linear attenuation coefficient [cm^{-1}] for the photons

$\beta (= 1/\bar{x})$ is a linear coefficient [cm^{-1}] describing the longitudinal energy deposited downstream by "response" electrons launched from every upstream point x'. The drop-off in dose is assumed to be a steep exponential due to the divergence of electrons away from a site of photon interaction.

The primary dose reaches its peak value for the usual condition:

$$\frac{dD_P}{dx} = 0 \tag{5}$$

from which we can obtain the value of d_{max}.

$$d_{\max} = \frac{1}{(\beta - \mu)} \ln(\beta / \mu) \tag{6}$$

For deeper locations (i.e., $x >> d_{max}$), transient TCPE is established[49] and assuming $\beta >> \mu$, equation (4) reduces to the following form:

$$D_P(x) = \frac{NK_0\beta}{(\beta - \mu)}\left(e^{-\mu x} - e^{-\beta x}\right) \tag{7}$$

These equations provide a good introduction to convolution techniques and to the basic concept of equilibrium. In real radiotherapy beams, the shape of the actual depth-dose curve, however, will differ from that predicted by these simple equations. In addition to the inverse square law effect, the contributions of contaminant radiation incident on the patient, the photon scattering within the patient, and lateral disequilibrium must also be taken into account.

2. Lateral TCPE

As stated above, TCPE can be achieved at depths beyond the maximum projected range, R_{max} of the charged particles provided the field area is sufficiently large to achieve electron equilibrium in all the lateral directions.[74,75] Figure 3a shows how the dose and the collision KERMA change with depth and with field size for an 18 MV x-ray beam. These computations demonstrate clearly how longitudinal and lateral equilibrium conditions (Figure 3b) must *both* be satisfied for TCPE to become established in 3D. At shallow depths and for narrow field sizes, more energy leaves a region of interest than enters it, creating a reduction in dose, compared with the dose in full build-up regions. Table 5 summarizes the minimum equilibrium depths (d_{max}) and radii required to achieve TCPE in a uniform water absorber for a variety of photon beams. If both conditions are satisfied (i.e., depths > d_{max}, and field size > R_{min}), TCPE is achieved in the water absorber. The data show that as an approximate rule-of-thumb, the lateral electron range is about one-third of the forward range.

D. Influence of Tissue Density and Atomic Number

1. Density scaling

The mass attenuation and absorption coefficients, which describe photon interactions, are, by definition, independent of mass density. Similarly, the

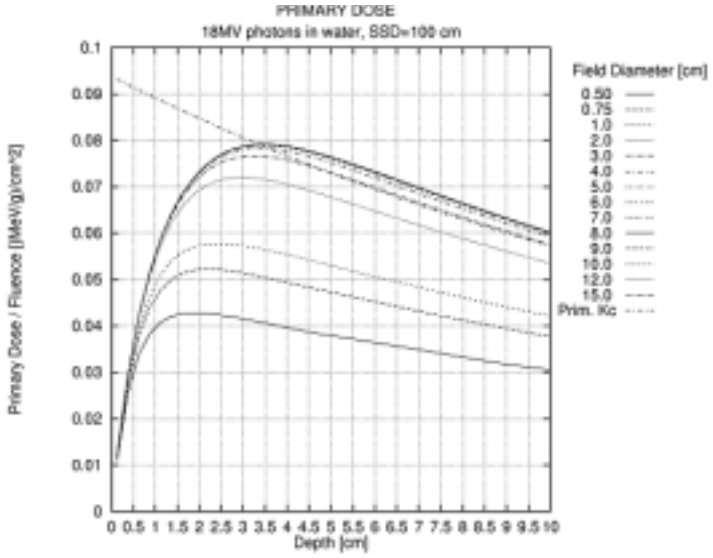

Figure 3a. Primary depth-dose per unit fluence for 18 MV x-rays for a family of field sizes ranging from 0.5 to 15 cm in diameter. The primary collision kerma is also shown to illustrate how CPE or TCPE must be satisfied in three dimensions to achieve a proportional relationship between collision kerma and absorbed dose.

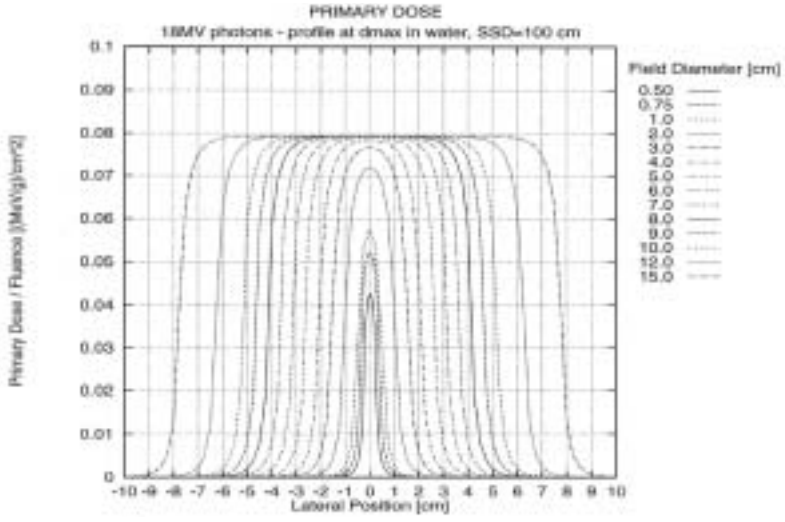

Figure 3b. Primary dose profile at d_{max} per unit fluence for 18 MV x-rays for a family of field sizes ranging from 0.5 to 15 cm in diameter.

Table 5. Minimum equilibrium depth (d_{max}) and radius (r) required to achieve TCPE in a uniform water absorber for a variety of photon beams.

Photon Energy	Water	
	Minimum Equilibrium Depth (d_{max})	Minimum Equilibrium Radius (r)
100 keV	0.15 mm	0
1 MeV	4.5 mm	1.5 mm
10 MeV	5 cm	2 cm

(Reprinted from: M.Tubiana, J Dutreix, A. Dutreix, and P. Jockey, "Bases Physiques de la radiotherapie et de la radiobiologie", Editions Masson (1963) with permission from Editions Masson.)

mass stopping powers that describe the transport of charged particles set-in-motion are quasi-independent of density in solid materials, except for the polarization effect. In dealing with geometric dimensions of beams and patients, corresponding linear coefficients are often needed and they are obtained by density multiplication (e.g., $\mu = \mu/\rho \bullet \rho$). In a heterogeneous medium, the attenuation of photons in a layer of tissue (of length t) can be calculated using the "radiological-pathlength" thickness, ρt, (g/cm^2) of each tissue inhomogeneity. Such adjustments in inhomogeneity correction methods are often referred to as density scaling. Since most interactions are Compton events, such scaling should be done in accordance with the *electron density* relative to water, rather than mass density.

The electron density (e^- per cm^3) is given by the product $N_A(Z/A)\,\rho$, where N_A is Avogadro's number and ρ is the mass density. The *relative electron density* is normalized to the electron density of water, which is 3.34×10^{23} e/cm^3. This density can be measured easily for water-like tissues *in vivo* using x-ray computed tomography,[76,77,78] but it can only be estimated for materials of unknown atomic number such as bone *in vivo*.[79]

Fano and O'Connor's Theorems

The dosimetric data used in treatment planning are mainly derived from water. The existence of two important theorems of radiation transport (for photons and for charged particles) by O'Connor and Fano enables density scaling of data for water to "water-like media" with arbitrary densities.

Fano's theorem[80] states that when an infinite medium of varying density but constant atomic composition is exposed to a uniform photon fluence (i.e., CPE conditions), differential in energy and direction, then the fluence of charged particles launched by the photons is also constant and not affected by density variations. This constant fluence of secondary electrons equals the fluence generated under conditions of charged particle equilibrium (CPE) for a given fluence of photons. Consequently, the absorbed dose across any area of density

variations would be constant. This is intuitively plausible since density not only modulates the number of electrons launched per unit volume, but also rescales their linear range.

The main assumption in Fano's theorem[81] is that the interaction cross sections per unit mass are independent of the density of a medium of identical atomic composition.

Strictly, in order to apply Fano's theorem to external photon beams, one must assume that the:

- primary photon attenuation,
- the stopping power density effect, and
- the release of secondary photons

can be neglected in an equilibrium layer surrounding a dose point of interest.

Ignoring photon attenuation essentially means that the mean free paths of primary photons must be much larger than the maximum ranges of the released secondary electrons. This first condition can be fulfilled in clinical beams, with photon energies less than 1 to 3 MeV and applies to points in an externally irradiated medium that are sufficiently far from boundaries.[82]

Density or polarization effects (within the density range of human tissues) are generally small for clinical beams and the production of secondary photons is not problematic as long as their mean free paths are larger than the ranges of secondary electrons. For the above reasons Fano's theorem provides an important test of dose calculation algorithms.[83]

While Fano's theorem applies to situations of charged particle equilibrium, the *density-scaling theorem* by O'Connor[84] relates the dose in two media of different density but equal atomic composition, both irradiated by the same external beam. According to this theorem, the ratio of the secondary scattered photon fluence to that of primary photon fluence is constant in the two media provided all geometric distances, including field sizes, are scaled inversely with density. This means that the dose at corresponding points in two media is the same if all dimensions in the irradiation geometries are scaled inversely with density.

While these two theorems provide good insights into the problem of changing density, they should not be applied without recognizing their basic inherent assumptions. They have limited applications to heterogeneous tissues since both density and atomic composition are likely to change simultaneously (e.g., bones, prostheses).[85] Fano's theorem is also implicitly built on the same assumptions that underpin charged particle equilibrium; this requirement has sometimes been understated and overlooked.[82]

Both Fano's and O'Connor's theorems rely on a common assumption that the interaction probability (per electron) is independent of density variations between media. The common foundations and relations between these two theorems were analyzed and unified mathematically within a general framework by Bjarngard.[86]

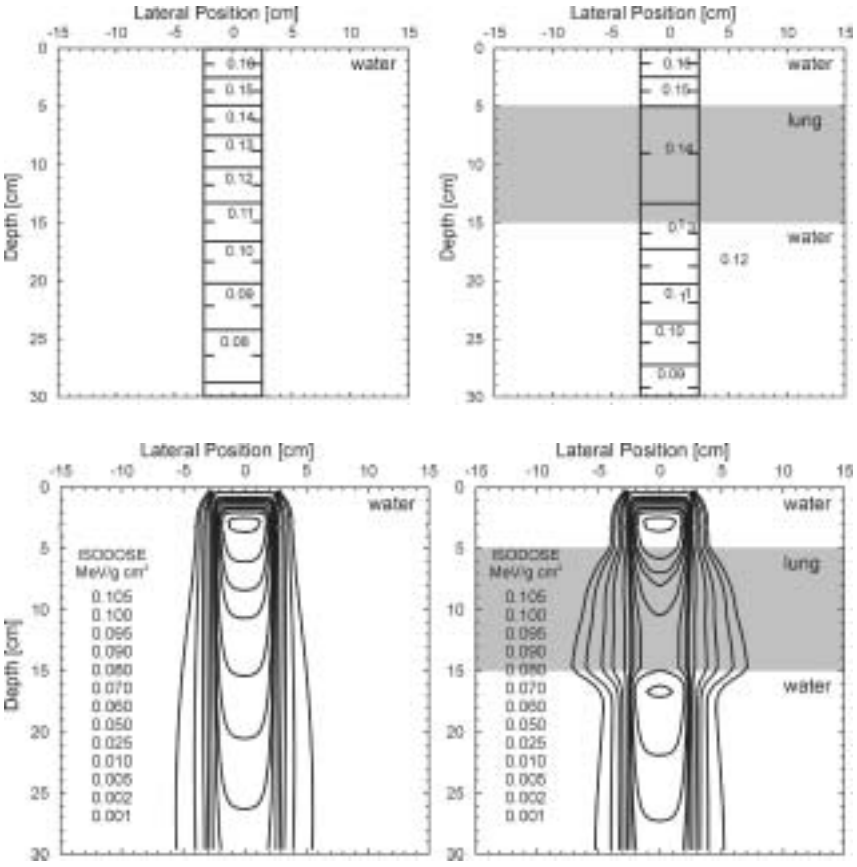

Figure 4. Fluence and DOSE distributions for a beam of 5.0 MeV photons (5×5 cm^2 field) incident on a water phantom (a and c) and a slab phantom with a cork insert (b and d). Fluence distribution in a water-cork-water phantom (b). DOSE distribution in a water phantom (c). DOSE distribution in a water-cork-water phantom (d). Note the dose reduction in the central region of the cork and the penumbral flaring of the beam. (Reprinted from J. J. Battista and M. B. Sharpe110, "True three-dimensional dose computations for megavoltage x-ray therapy: a role for the superposition principle," *Australas. Phys. Eng. Sci. Med.* 15:159–78 (1992) with permission from the Australasian College of Physical Scientists in Medicine.)

The influence of electron density on photon fluence and dose is illustrated independently in the low-density slab phantom exposed to monoenergetic 5 MeV photons (Figure 4). The changes in photon transport can be easily calculated using density scaling of the layers (Figure 4a and 4b). However, the range

of recoil electrons is significant, such that they can be released in one medium and absorbed in a different downstream material. The initial "build-up" of dose in water is followed by a "build-down" within the low-density region and a "rebuild-up" occurs in the distal water section (Figures 4c and 4d). Figures 5 and 6 isolate the contributions from electrons launched in different density regions and explain the complex shape of the depth-dose curve. In such a case (high energy, small field, low density), inhomogeneity corrections based solely on photon fluence or attenuation would be inadequate (see Figure 6). On the other hand, simpler calculations based solely on photon fluence can be quite accurate for lower photon energies where primary photon fluence, KERMA, and TERMA are linearly related (see section F. below). Unfortunately, it is not always easy to predict *a priori* which tissue regions are prone to disequilibrium for a 3D irradiation of a heterogeneous absorber.

While this section has emphasized the effect of density on central axis values of photon fluence and of dose, density can also affect the beam penumbra in tissue,[87] due to a lateral loss of TCPE at the field edge. Thus the beam edge is blurred in low-density absorbers due to the increased lateral motion of charged particles, as seen in Figure 4. Monte Carlo calculations have shown that the primary penumbra width is inversely proportional to tissue density whereas the density has the opposite effect on the scatter penumbra, since the

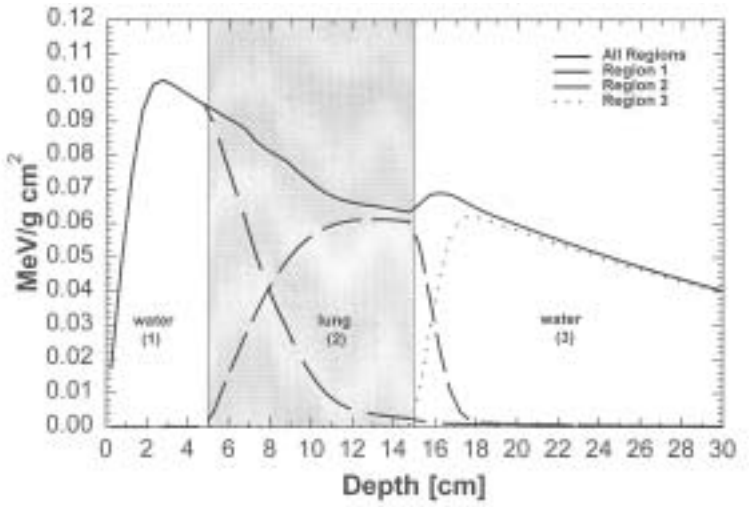

Figure 5. Isolation of electron contributions launched in different density regions. In such a case (high energy, small field, low density), lung inhomogeneity corrections based solely on photon fluence or attenuation would be inadequate.

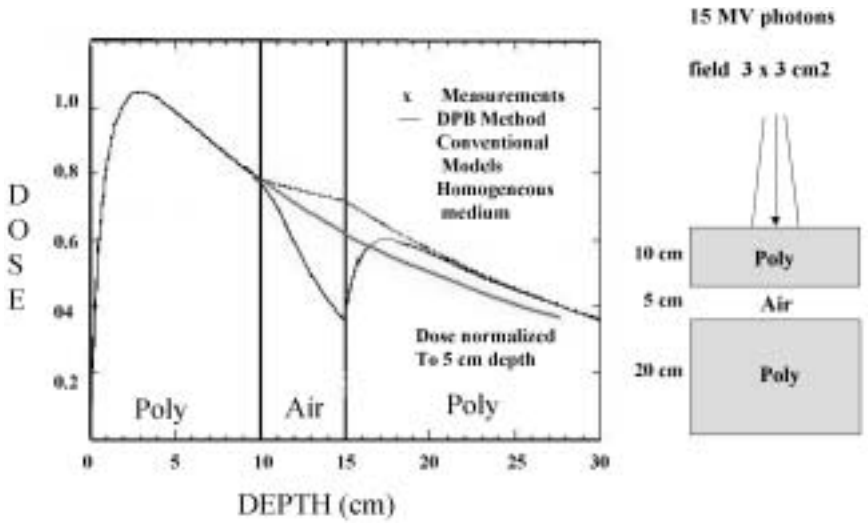

Figure 6. Significant electronic non-equilibrium effects occur at the interfaces between media of different densities for fields whose sizes are of the same order of magnitude as the range of electrons. (Reprinted from R. Mohan, C.-S. Chui, and L. Lidofsky,[108] "Differential pencil beam dose computation model for photons," *Med. Phys.* 13:64–73 (1986) with permission from the American Association of Physicists in Medicine.)

scatter dose decreases with the decrease of density. Therefore, the inverse proportionality of penumbra width with density does not hold for the total dose.[34] For an 18 MV x-ray beam, the penumbra width (80%–20%) was measured to be 2.4 times bigger in lung-density phantom than in water phantom, whereas for a 4 MV beam, the penumbra width has been measured slightly smaller in the low-density medium.[33]

This penumbral degradation effect should be carefully considered when 3D conformal radiotherapy is intended to assure coverage of the planning target volume.[88] The effects need to be considered in the context of multiple overlapping fields.

2. Effects of atomic number

The pattern of dose distributions in the presence of high atomic number inhomogeneities is perturbed due to a number of complex effects:

(a) The opportunity for competing photon interactions (e.g., pair production, which increases with atomic number) may reduce the proportion of Compton-scattered photons (Figure 2). Secondly, pair production affects the spectral distribution of the secondary charged particles as well as

Table 6. Mass attenuation coefficient dependence on atomic number

Atomic number, ***Z***	**Mass attenuation coefficient at low photon energy, (cm^2/g)** $\left(\frac{\mu}{\rho}\right)_{le}$	**Mass attenuation coefficient at high photon energy, (cm^2/g)** $\left(\frac{\mu}{\rho}\right)_{he}$	**(cm^2/g)** $\left(\frac{\mu}{\rho}\right)_{le} - \left(\frac{\mu}{\rho}\right)_{he}$
1 to 10	3.5 (for Z=1) to 1.9 (for Z=10) decreases with increasing Z	2.7 (for Z=1) to 1.4 (for Z=10) decreases with increasing Z	0.8 (for Z=1) 0.5 (for Z=10)
11 to 60	0.9 (for Z=11) to 7.0 (for Z=60) increases with increasing Z	0.4 (for Z=11) to 1.0 (for Z=60) increases with increasing Z	0.5 (for Z=11) 6.0 (for Z=60)
61 to 92	7.1 (for Z=61) to 4.4 (for Z=92) decreases with increasing Z	0.1 (for Z=61) to 2.8 (for Z=92) increases with increasing Z	7.0 (for Z=61) 1.6 (for Z=92)

(From the National Institute of Standards and Technology—NIST, http://www.physics.nist.gov/Divisions/Div846/Gp2/gp2.html.)

their range. The stopping of positrons may also generate tertiary annihilation photons.

(b) The mass attenuation coefficient depends on atomic number (Table 6), thus exponential attenuation of photon fluence and TERMA is greatly accentuated. Severe attenuation can spoil the uniformity of photon fluence in "shadowed" regions, violating a necessary condition for charged particle equilibrium.

(c) The mass energy absorption coefficient depends on atomic number, and thus the collision KERMA is changed locally within the absorbing material. This is well known in kilovoltage x-ray dosimetry, where a factor is used to calculate the enhancement of dose to bone for a given photon fluence, assuming CPE. For megavoltage photons, the collision KERMA can similarly be used to estimate the local dose, but only if a sufficient mass of material allows CPE or at least TCPE to become established. This is generally not the case for small bone regions and such dose enhancement calculations based on K_c ratios are not very accurate in bone.

(d) With increasing atomic number, a more detailed inclusion of electron transport is needed for megavoltage x-ray beams. Multiple scattering of

charged particles by the nucleus[89] is accentuated producing a local variation in their angular distributions, which can also spoil the equilibrium conditions, yielding "hot/cold spots".[90,91] For example, back scattering from higher atomic number materials yields a significant contribution to the electron fluence and dose at the interface between soft tissue and a material of higher atomic number. For metallic interfaces encountered in prosthetic implants, dose increases of up to 50% are measured in the backscatter direction within the range of electrons set in motion by 18 MV x-rays. At such higher energies, the transition zone extends over several centimeters and can affect a significant volume of adjoining tissue, with a potential for adverse clinically observed reactions.[85,92,93]

In summary, the most general solution to inhomogeneity corrections should account for changes in electron density as well as atomic number of the tissues traversed by primary photons and all secondary photons and charged particles. Because of the dominance of water-like soft tissues and of Compton and Coulomb interactions within them, the electron density of tissues is the most important parameter and has merited the greatest attention. However, we remind the reader that special considerations for elevated atomic number are sometimes needed for bone or for metallic prostheses, especially in the upper range (greater than 10 MV) of megavoltage energies.[48]

E. Concept of Primary and Scattered Dose Components

The primary and secondary particle contributions to dose (photons and electrons) exert their influence over a different range and they are individually affected to different extents by tissue inhomogeneities and beam boundaries. It is common to decompose the total dose into two components referred to as the "primary" and "scattered" dose components. Generally, this separation has been done empirically using conventional dosimetry instrumentation, but more recently Monte Carlo simulations have aided in the more rigorous definition of "primary" and "scatter" separation.[94] Simplified point source models have been extended to include extra focal radiation.[95,96,97]

Those photons that are incident upon the surface of the patient (or phantom) are termed *primary.* Some of those have traveled directly from the radiation source: others have been produced as a result of interactions within the structures comprising the treatment head. Most of these interactions are Compton-scattering events, which generate secondary electrons in addition to scattered photons. In addition, pair production can occur if the incident photon has sufficient energy (i.e., above 1.02 MeV), resulting in the generation of electron-positron pairs and subsequent generation of photons of 0.51 MeV from positron annihilation. Since these occur mostly in structures in the head of the machine (some occur in the intervening air) we refer to the photon component as *head-scattered photons,* but they still belong to the "incident" or "primary" group. The dose from primary photons to the central axis of an open beam at depth in

a phantom will depend upon: (i) distance from the source; (ii) head-scatter, which will depend upon collimator setting and other beam defining parts (block, wedges); (iii) attenuation, i.e., absorption and scattering in the phantom, determined by depth and beam energy. At any depth, the dose contribution from primary photons is determined by the collimator setting, and not by the size of the radiation field at that depth.[98]

The first time such photons interact with the medium, they contribute to primary dose through recoil electrons. *Scattered component* is that part of the dose which is deposited by photons which have previously interacted at least once in the medium. The proportion of dose due to scattered photons depends upon photon energy and the volume of patient irradiated (field size, depth, and patient thickness).

The total dose along the central axis can then be decomposed into:

$$D\ (x,\ \mathrm{r}) = D_p\ (x) + D_s\ (x,\ \mathrm{r}) \tag{8}$$

where *r* refers to the radial distance to the field edge. Extrapolating the dose *versus* field size curve to a small pencil beam field size isolates the primary dose. The limiting field size chosen will determine if the primary component includes or excludes the primary electrons and this leads to some ambiguity about the definition of a "pencil beam".[94,99] This is because two effects simultaneously reduce the central dose: (i) a reduction in the photon fluence; and (ii) a reduction in the electron fluence generated by the primary dose component. As the pencil size progressively shrinks, the dose rapidly changes in a non-linear way due to the combination of these effects, and the extrapolation value needs to be decided. It is possible to clarify and standardize the definition of the primary component more precisely by using auxiliary Monte Carlo calculations.[99,100] If the small "0×0" field is limited to an equilibrium pencil beam, then the scattered component can be considered as due to scattered photons only (see Woo et al.[94], Figure 7). In this case, the pencil dimension should be small enough to avoid incorporation of scattered photons, but yet large enough to preserve charged particle equilibrium (CPE) in the lateral dimension.[101,102,103]

The primary dose is essentially the primary collision KERMA, which is the dose deposited from charged particles set in motion by primary photons only. The scatter dose is then attributed to all secondary radiations, including Compton-scattered photons, annihilation photons, and bremsstrahlung. Figure 8 shows the spread of energy by secondary radiations away from the photon interaction point. From such "dose spread functions," also known as "scatter kernels," "point kernels,"[104,105,106] "dose spread arrays,"[72,107] "differential pencil beams"[108] or "influence functions,"[70,74,109] it is possible to quantify their relative contributions to dose at a point under full scattering conditions (i.e., within an infinite medium irradiated by an infinitely broad beam). Using the reciprocity theorem,[49] the contribution from each component is simply the summation of all pixel values in each dose-spread image. Figure 9 shows the results of such a calculation,[87,110,111] and indicates

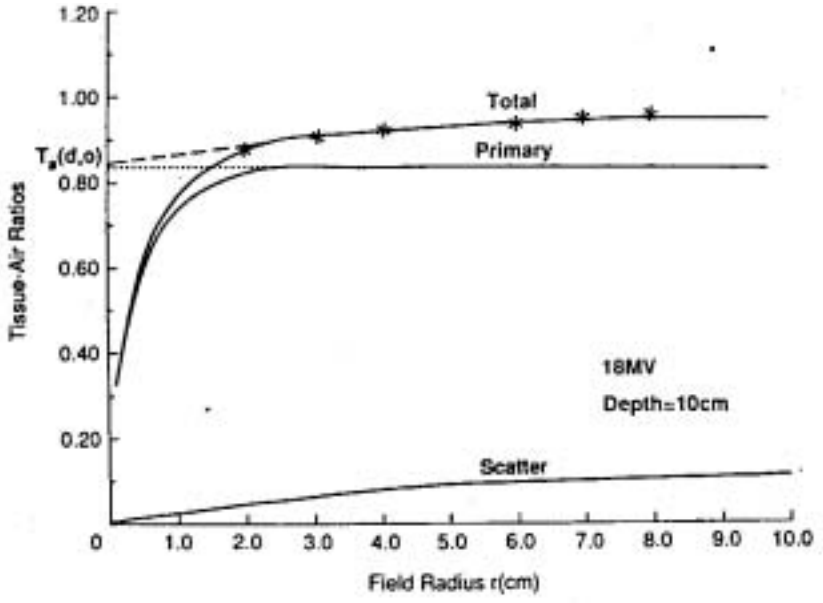

Figure 7. Tissue-air-ratios for an 18 MV photon beam at a depth of 10 cm in water, as a function of field radius r. The asterisks represent the measured data. The solid curves are generated using Monte Carlo, normalized to the measured tissue-air ratio at 3 cm (Reprinted from M. K. Woo, J. R. Cunningham, and J. J. Jeziorenski,[94] "Extending the concept of primary and scatter separation to the condition of electronic disequilibrium," *Med. Phys.* 17:588–595 (1990) with permission from the American Association of Physicists in Medicine.)

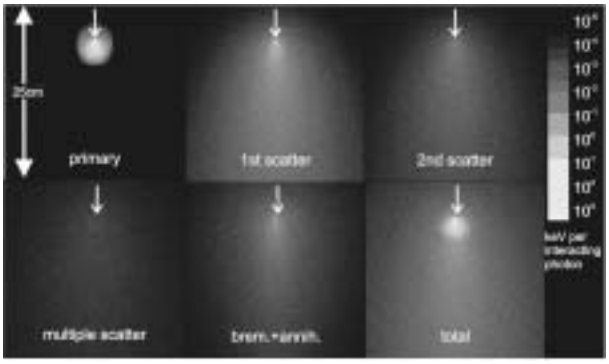

Figure 8. Intensity map of the distribution of the primary and varying orders of scatter in water from a 6 MeV photon pencil beam.

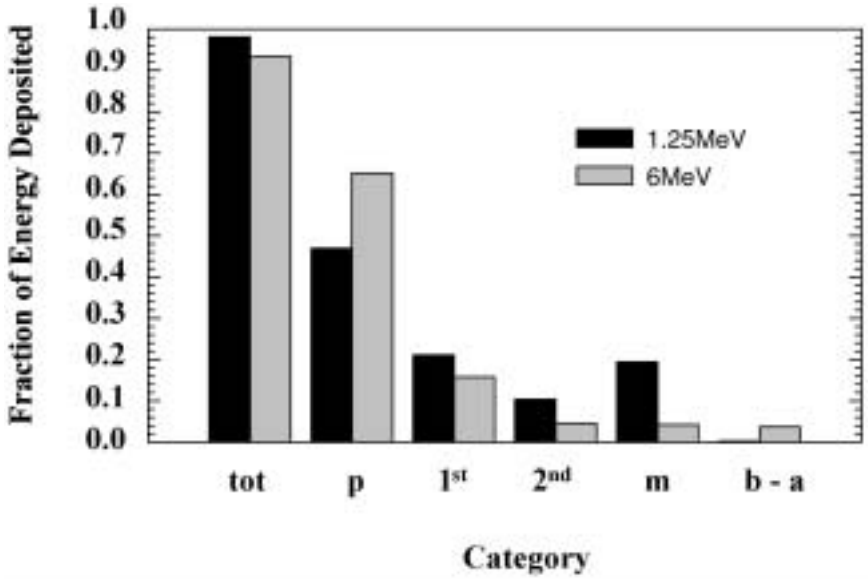

Figure 9. Quantification of the relative importance of all interaction processes (for a 1.25 MeV and a 6.00 MeV beam) to dose at a point under full scattering conditions. The contribution from each component is simply the summation of all pixel values in each dose spread image.

the relative importance of all interaction processes for a 1.25 MeV and a 6.00 MeV beam. Similar data have also been previously obtained by both measurements in a water absorber,[109,112,113] and by analytical calculations of the first and second Compton scattering components.[114,115,116]

F. Introduction to the Superposition and Convolution Principles

The superposition principle is very general and widely used in many branches of physics and engineering. It can serve as a universal basis and aid in the understanding and categorization of tissue inhomogeneity correction methods within a common framework.[55,117,118,119,120,121]

In this context, the initial sites of photon interactions can be viewed as "sources" of energy and the "point kernels" are the energy spreading functions or blurring functions as just described (Figure 10). For an external beam of radiation, a downstream shower of secondary radiation is triggered from every primary interaction point in the patient. The magnitude of the primary photon impulse is the energy released at each interaction site, or total energy released per unit mass (TERMA), and is dependent upon the primary photon fluence. The pattern of energy spread away from an energy release point, per unit

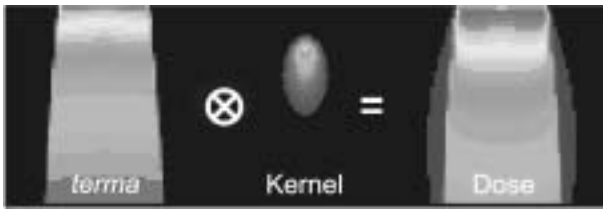

Figure 10. A schematic illustration of the superposition method of dose calculation. The dose distribution is a superposition of dose spread kernels that are modulated by the amount of energy released at each irradiated point; i.e., the TERMA distribution.

TERMA, is the total dose spread function or kernel. Inhomogeneity corrections are essentially aimed at modifying the primary TERMA values, based on attenuation of the photon fluence, and at also modifying the dose spread functions at each point in the patient. More accurate methods use a variety of kernels for each possible interaction mechanisms (e.g., single Compton scattering), and each kernel is corrected individually for the effect of inhomogeneity.

This superposition approach to dose calculations was first suggested for external beams of radiation by Roesch,[70] who described an "influence function". The concept was also explored semi-empirically[71] in order to explain the build-up portion of depth-dose curves for higher energy x-ray beams from an early betatron. The notion of such response functions, however, remained dormant until Cunningham and Beaudoin developed the concept of voxel scatter strengths based on differential scatter-air ratios,[112] Sontag and Ray[122] used scatter weights. O'Connor and Malone also derived primary dose spread arrays from measurements for a cobalt-60 beam,[113] and Wong et al.[123] attempted to determine iso-influence data experimentally using an air void in water. More detailed response functions, which segregate the different interaction processes, have since been calculated using analytical[114,124,125] or Monte Carlo methods.[72,108,119,126,127,128,129,130,131,132]

Mathematically, the dose is obtained from the most general superposition integral:

$$D(\vec{r}) = \int T(\vec{r}\,') \cdot K(\vec{r};\vec{r}\,')d^3\vec{r}\,' \tag{9}$$

where $T(\vec{r}\,')$ describes the total energy released by primary photon interactions per unit mass, or TERMA, at $\vec{r}\,'$ and $K(\vec{r};\vec{r}\,')$ is the dose spread kernel which describes the fraction of energy deposited at $\vec{r}$ by secondary particles originating at $\vec{r}\,'$ and is allowed to be spatially variant. This is a computationally intensive operation since every point in the irradiated volume (r′) contributes to each dose point ($\vec{r}$) one pair ($\vec{r}$; $\vec{r}\,'$) at a time. In the special case of a spatially *invariant* kernel (i.e., $K(\vec{r};\vec{r}\,') = K(\vec{r} - \vec{r}\,')$ such as in a homogeneous absorber,

the superposition collapses to a convolution integral because the dose contribution depends only on the *relative position* of the dose and scattering point pairs. It may be evaluated in real space as an integral or in Fourier space as a simpler multiplication:

$$D(r) = F^{-1}[F\{D\} = F\{T\} \cdot F\{K\}] \tag{10}$$

where F and F^{-1} denote the Fourier Transform and inverse operation. This convolution approach relies on several assumptions[111,133] but it greatly reduces the computation time when the dimensionality of the integral is high (e.g., 3D) and if the Fast Fourier transform (FFT) is applied.[111,134,135]

IV. INHOMOGENEITY CORRECTION METHODS

Dose calculation methods that account for tissue density variations can take two general forms.[136] In the most conventional form, a relative dose distribution is first calculated assuming a patient consisting of homogeneous water-like density. The link between those relative distributions and absolute dose is the machine-calibrated output that is defined at some reference point in water. Then an inhomogeneity correction factor (ICF) is applied which makes adjustments to the uncorrected distribution to account for variations in tissue density. The ICF is thus defined as:

$$ICF(r) = \left(\frac{dose\ in\ heterogeneous\ medium}{dose\ at\ same\ point\ in\ homogeneous\ medium} \right) \tag{11}$$

Alternatively, the dose can be calculated to a point in a heterogeneous medium directly using a model of radiation transport that would yield absolute dose *a priori*. Relative dose distributions can then be constructed by normalizing to a reference point.

In treatment planning where the ICF method is used, there are three steps necessary for correcting a dose distribution for tissue density variations:

- The dose is calculated in a water-like medium which adequately reproduces beam data measured in water and which is capable of modeling other effects such as irregularly shaped fields, patient surface contour, and primary beam intensity modulators
- Tissue density and atomic number information must be available for the anatomy of the patient in question
- An inhomogeneity correction method is required to account for variations in tissue density and atomic number.

These components are intricately connected and, at times, difficult to separate. For example, the correction for external patient contour shape can be part

of the homogeneous dose calculation but it is sometimes considered instead as part of the inhomogeneity correction, using air voxels near the patient's surface. In this report we focus on inhomogeneity corrections internal to the patient and will therefore mostly involve the latter two steps above.

Most radiation therapy clinics should have access to three-dimensional (3D) CT patient density information,[137,138,139,140,141] although many patients might still be planned using only 2D single-slice input information.

With either 2D or 3D density information, all inhomogeneity methods begin with a primary beam ray-tracing procedure. This incorporates an explicit calculation of the changes in TERMA or photon fluence due to changes in density along the primary beam rays from the radiation source to every point of calculation within the patient.

From there, the methods differ mainly in the way they address the scattered photon contribution and scattered primary electrons, and in the sampling of anatomical 3D density information. A classification scheme based on these considerations is shown schematically in Figure 11 and forms the order in which different correction methods that will be reviewed in this report. Table 7 summarizes the various methods presently available and categorizes them according to the physical considerations of Figure 11.

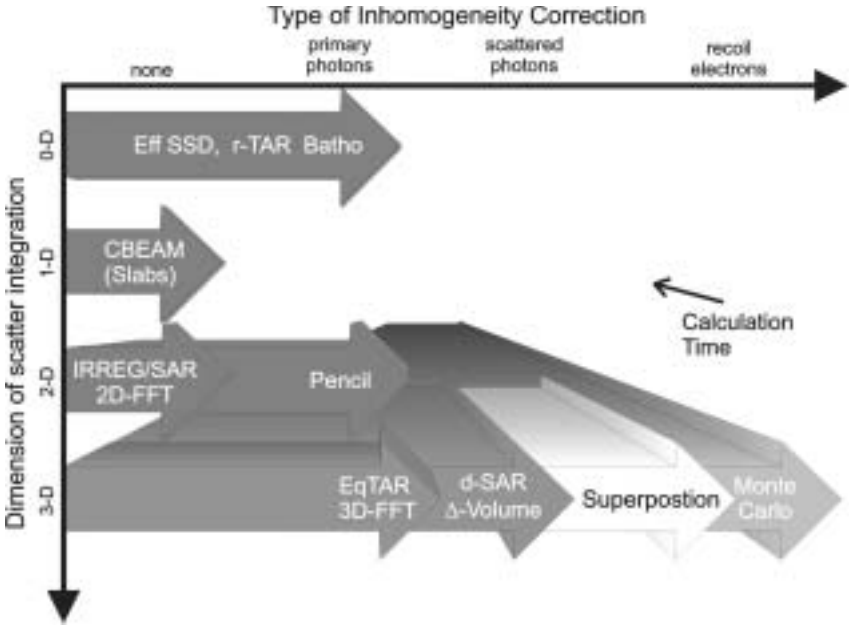

Figure 11. Classification of inhomogeneity correction algorithms according to their ability for scatter integration and to calculation time.

Table 7. Categorization of different inhomogeneity correction algorithms according to the level of anatomy sampled (1D or 3D) and the inclusion or exclusion of electron transport.

	TERMA	DOSE
	Local energy deposition (No electron transport)	*Non-local energy deposition (Electron transport)*
1D	**Category 1**	**Category 3**
	1.1 Linear attenuation 1.2 Ratio of TAR (RTAR) (Equivalent path length, effective SSD, isodose shift) 1.3 Power law (Batho)	3.1 Convolution (pencil beam) 3.2 FFT techniques
3D	**Category 2**	**Category 4**
	2.1 Equivalent TAR (ETAR) 2.2 Differential SAR (DSAR) 2.3 Delta volume (DVOL) 2.5 3D Beam Subtraction Method	4.1 Superposition/Convolution 4.2 Monte Carlo 2.4 Differential TAR (dTAR)

There are numerous reviews on inhomogeneity correction methods in the literature categorizing them according to various criteria:

- Some classification schemes focus attention on the detail of the scatter calculation. For example, methods can be distinguished coarsely according to whether they "sense" the proximity and lateral dimension of an inhomogeneity and whether the scattered electrons are considered explicitly.[142] Others, categorized methods according to their ability to consider anatomical information (e.g., 2D or 3D geometry) in predicting scattering effects,[143] and CT density information they use.[144,145,146,147,148] It is important to consider whether the full 3D voxel data set is actually sampled per calculation point or whether only a subset (e.g., 1D ray-tracing) enters the scatter calculation.[117,120]
- A mathematical classification criterion is based on the integral used to sum the scatter from elements such as slab, pencil, or voxel scatter kernels.[55,81,117,118] The physics described by these kernels and how they are each adjusted for tissue inhomogeneity are distinguishing features in terms of accuracy and speed of an algorithm. The most accurate methods independently adjust the energy released from a voxel by scattered electrons and photons.

In this report, we chose to categorize the available methods in accordance with their ability to treat primary TERMA and electron transport separately (i.e., TERMA and DOSE) and whether the anatomy is being sampled along one-dimensional primary rays (1D) or the full three dimensions (3D). Table 7

includes methods in increasing order of complexity and accuracy (from category 1 to category 4), at the expense of more input anatomy data sampling and slower performance (CPU time per point per beam). The different methods of inhomogeneity correction will now be reviewed individually.

Category 1: Local Energy Deposition (No Electron Transport); 1D Density Sampling

This elementary class of inhomogeneity correction methods was originally developed in the late 1960s and later modified to incorporate pixel density data when CT became available.[78,79,144,149,150,151,152,153,154,155,156,157,158,159,160,161,162,163,164,165,166] These methods deserve some attention because (i) they are the most predominant methods that have been used in 2D or 3D commercial treatment planning systems for decades, (ii) for practical considerations, they will remain in clinical use for some more years, and (iii) despite the use of full simulation models in modern treatment planning systems, simple approaches are still needed and will most likely be further refined for independent checks of the treatment planning results. These models assume that:

- the patient consists of a semi-infinite slab geometry per calculation point, and
- all energy from the photon interactions is deposited at the site of interaction.

Only primary ray-tracing is used to calculate the dose to a point. This also results in an implicit adjustment of the scattered photon contribution. An illustration[167] of the semi-infinite slab approximation along with examples of primary and first order scatter ray tracing is shown in Figure 12. For the primary fluence calculation, a primary ray trace is exact and identical for 1D, 2D and 3D geometries provided that the density sampling follows the proper trajectory of the divergent ray. 2D planning in a single CT slice with 1D ray tracing does not take into account the geometry and density information from the whole irradiated volume, resulting in erroneous scatter estimation. Typically, cylindrical symmetry is assumed and the single patient slice is extended in the longitudinal direction to build a “3D” patient volume. Attention should be paid when using these kinds of algorithms in selection of the beam dimensions and beam weights, which may implicitly include or exclude the inhomogeneity correction factor. In the case of non-coplanar beams using one or few CT slices, primary ray-tracing is not always possible due to the lack of density information along oblique raylines which cut through missing adjacent CT slices. When calculating dose far away from an inhomogeneity, this elementary class of inhomogeneity correction methods gives results with less than 5% error, but for a complex heterogeneous medium and for dose calculations within or in the near vicinity of an inhomogeneity, errors larger than 5% can occur.[167]

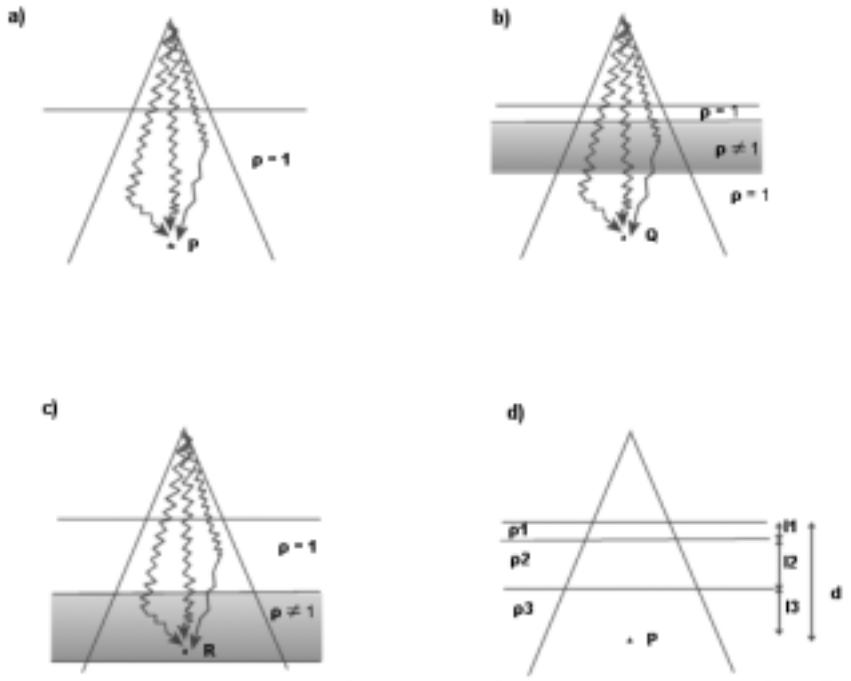

Figure 12. The dose to point P in a homogeneous tissue-equivalent medium (a) is a result of both primary and scattered radiation. Introduction of an inhomogeneity (b) and (c) alters the attenuation of the primary as well as the magnitude of scatter; the former a function of thickness of the inhomogeneity, while the latter is also a function of the position and lateral dimensions of the inhomogeneity. Traditional methods (d) consider only effects on the primary by calculating an effective thickness.

Method 1.1: Linear attenuation

The simplest form of inhomogeneity correction is to adjust the dose at a point on the basis of the overlying thickness of the inhomogeneity and using a "percent per cm" correction (Table 8). This method is very crude and is useful only for a quick estimation of the dose adjustment:

$$ICF = (\%\ \text{per}\ cm) \times \textit{inhomogeneity thickness} \quad (cm) \qquad (12)$$

Clearly, this does not include patient-specific densities nor any consideration of the geometric treatment beam parameters (e.g., field size).

Table 8. Simple correction (percent per cm) of the dose according to photon energy and tissue density.

Energy	%/cm Correction	
	Lung	Bone
Cobalt-60	+4.0%	–2.5%
4–6 MV	+3.0%	–2.0%
10 MV	+2.5%	–1.5%
18–25 MV	+1.5%	–1.0%

Method 1.2: Effective attenuation coefficient

A slightly more sophisticated version of a similar concept uses the effective attenuation coefficient and the point correction is given by

$$ICF = e^{\mu'(d-d')} \tag{13}$$

where:

μ' is the effective attenuation coefficient of water for a particular beam quality,

d is the physical depth from the surface to the point of calculation, and

d' is the "radiological depth," "equivalent depth," or "equivalent path length" and is given by

$$d' = \sum_i \left(\Delta d_i\right) \cdot \rho_i \tag{14}$$

where Δd_i are the thicknesses of tissues with different relative electron densities ρ_i lying above the point of calculation. In this method, patient specific densities can be used in the evaluation of d', but treatment beam parameters are still ignored.

Method 1.3: Ratio of tissue-air ratios (RTAR)

This method was one of the most commonly used methods in older commercial treatment planning systems and is still used by many physicists for manual "spot checks" of dose. Other names have been given to this method such as "effective SSD" or "isodose shift" but these essentially have the same foundation. This correction method is given by

$$ICF = \frac{TAR(d', W)}{TAR(d, W)} \tag{15}$$

where d' is the equivalent path length given by equation (14), d is the physical depth, and W represents the field size at the level of the point of interest. Here the primary ray trace produces a radiological depth, which is used for looking up a revised tissue-air ratio (TAR) value. In this manner, this method provides an exact correction for the primary fluence, or dose if the condition of electron equilibrium (CPE) is met. Correction to the scattered photon contribution is implicit although approximate in that only a modified depth is chosen for the TAR [and thus implicitly scatter-air ratio (SAR)] value. The ratio of tissue-maximum ratio (TMR) values could be used instead of TAR values as this is formally identical [since the backscatter factor (BSF) values are canceled out]. The popularity of this method is primarily due to its simplicity and its ability to approximately account for some scatter changes due to field size and effective depth.

The major weakness of the RTAR method is its compromised modeling of the lateral component of the scattered photon contribution that results in an over-correction when the density is less than that of water and an under-correction when the density is greater than water. This can be shown with the simple consideration of a homogeneous medium of density, $\rho < 1$. Here the RTAR corrected result of TAR(ρd, r) would be higher than TAR(ρd, ρr) which is the exact solution as given by the O'Connor scaling theorem.[84]

Method 1.4: Power law (Batho)

Batho in 1964,[168] and Young and Gaylord in 1970[169] proposed an empirical correction factor method for points lying within water and distal to an inhomogeneity by raising tissue-air ratios to a power that depends on density. This was generalized by Sontag and Cunningham[167] in order: (i) to include points within an inhomogeneity and (ii) to handle arbitrary densities and non-water-like materials. The correction factor is given by:

$$ICF = \frac{TAR\left(d_1, W_d\right)^{\rho_1 - \rho_2}}{TAR\left(d_2, W_d\right)^{1-\rho_2}} \tag{16}$$

where:

- ρ_1: relative electron density of the medium in which the point of calculation lies,
- ρ_2: relative electron density of the overlying material,
- d_1: depth within this medium, and
- d_2: distance to the upper surface of overlying material

A further modification of this method by Webb and Fox,[170,171] and Cassel et al.[172] allowed it to be adopted for CT tissue densities and is given by:

$$ICF = \prod_{m=1}^{m=N} TAR(X_m)^{(\rho_m - \rho_{m-1})/\rho_o} \left(\mu_{en} / \rho\right)_N / \left(\mu_{en} / \rho\right)_W \qquad (17)$$

where:

N:	number of layers of different densities above the point of calculation,
m:	layer number,
x_m:	distance from point of interest to the surface of the m^{th} layer,
ρ_μ, ρ_0:	electron density of the mth layer, and that of water,
$(\mu_{en}/\rho)_N$:	mass energy absorption coefficient of the material in layer N.

Equations (16) and (17) show that in the semi-infinite geometry, the effect of an inhomogeneity with density ρ is modeled as a compounding of TAR values. With the power law, the multiplicative relationship in the depth direction, shown in equation (17), is easy to understand for slab geometry. The model is sensitive to the proximity of the inhomogeneity and provides a first order approximation to changes in both primary and scattered photon fluencies in the slab geometry.

Some improvement has been demonstrated when tissue-maximum ratios (TMR) or tissue-phantom ratios (TPR) are used instead of TAR. El-Khatib and Battista,[173] Kappas and Rosenwald,[174] and Thomas[175] have found marked improvement by nearly 5% in the accuracy of dose calculated within lung when they substituted TMR values instead of TAR values for Co-60 radiation. El-Khatib and Battista173 provided measurements of the ICF for Co-60 and 6 MV energies. A cork thickness of 10 cm was used to simulate lung. The ICF was plotted as a function of the distance of the measurement point and the "top" of the cork slab. Results were obtained for small (5 cm × 5 cm), medium (10 cm × 10 cm) and large (50 cm × 50 cm) fields. Inside cork and for both energies they found that the maximum deviation of the TMR-Batho method from measured values was 3%. The deviation from measured values was consistently worse for the TAR-Batho method and can be as high as 9% for large fields. The authors give also a partial physical explanation why TMR-Batho method should give better agreement with measurements: (i) the TMR values include no inherent backscatter; (ii) the TAR value includes inherent backscatter, (iii) in lung of density 0.3 g/cm^3, backscatter is reduced and (i) is more appropriate.

For higher energies than Co-60 and when the point of calculation lies in the rebuild-up region (either inside the heterogeneity or in the water-like medium beyond it) the power law correction factor is undefined. For this case the above mentioned authors suggest a simple modification of the formula by adding systematically the build-up distance z_m to all depths before calculating the TMR. In this way one ensures that only TMR values from the equilibrium portion of the curve beyond z_m are used.

Many authors,[25,146,173,175,176,177,178,179,180,181,182,183,184,185,186,187,188,189,190] have demonstrated experimentally or by theoretical analysis the advantages and the limitations of the initial and the multiplicative generalized Batho method and/or compared it with other correction methods. According to them, the generalized power-law method:

(a) Provides an acceptable approximation below a single inhomogeneous layer with an extent larger than that of the field size and electron density less than that of tissue.
(b) Within an inhomogeneous layer, generalized corrections perform well when the relative electron density of the inhomogeneity is less than unity, but results become progressively worse for denser layers and larger field sizes.
(c) If the electron density (relative to water) of the inhomogeneous layer is greater than unity, the method overestimates the dose. In the extreme situation of a large inhomogeneity and large field sizes, the method has been proved to be inadequate with errors up to 10%.
(d) For very large radiation fields such as those used to cover the entire thorax or for half or total body irradiation, the method underpredicts the correction factor by as much as 12% in the middle of the lung.[178,179]
(e) It is a better model than that of the RTAR method and does provide better agreement with measurements in the slab geometry for small to medium field sizes.[173]
(f) The method is limited by the requirement of lateral charged particle equilibrium. Recent results[177] confirmed that dose errors in the calculated depth dose arise also from the neglect of electron transport. This effect increases as the field size decreases, as the density of the inhomogeneity decreases, and with the energy of incident photons, i.e. small fields of high-energy beams in lung may cause very large errors.[173,175]
(g) In clinical geometries which are rarely slab-like,[180] the Batho calculations do not appear to be much superior to those of the RTAR method. Artifacts arise in the calculations when applying the power law method to downstream positions near a lung-chest wall boundary. The contribution from the first layer of water-like tissue is canceled by the multiplicative model and the correction is erroneous because TAR values in the build-up region are used, despite an already established electron equilibrium condition in the lung. This erroneous result can be improved by using TARs that are exponentially extrapolated to shallow depths from larger depths to approximate the KERMA-depth curve instead of the depth-dose curve [see discussion of equation (4)].
(h) In contrast to the RTAR results, the Batho power law calculations in slab geometry have been shown analytically to undercorrect when the density is less than that for water and overcorrect when the density is greater than that for water.[182]

The above models were all developed in an era of radiation therapy when photon energies tended to be lower in the cobalt-60, 4 MV, and 6 MV x-ray energy range. The approximation of electron equilibrium was acceptable and thus TAR data could be used and adjusted directly. However, all these methods have been difficult to extend to situations where electron equilibrium does not exist.[36,191] Furthermore the handling of scattered photon radiation was approximate and indirect, accounting only for field size differences and effective depths in water. These were major weaknesses and necessitated the development of alternative methods.

Category 2: Local Energy Deposition (No Electron Transport); 3D Density Sampling

The assumption of slab-like geometry is inadequate for many clinical situations where the inhomogeneity intercepts only a portion of the radiation beam. Inhomogeneity correction methods described in this category provide a solution by including 3D density information in an explicit calculation of the scattered photon dose, but they still assume electron equilibrium or that electrons are absorbed at the point where they are created ("on the spot" absorption).

Method 2.1: Equivalent tissue-air ratio (ETAR)

The equivalent tissue air ratio method (ETAR[152,192]) was widely implemented in commercial treatment planning systems during the 1980s and is still in use on a number of modern systems. It can be considered as the first practical dose calculation method using the full CT data set for computerized treatment planning.

Principle of the method: According to the density scaling theorem,[84] the tissue-air ratio (TAR) in a field of radius r at depth d in a *uniform* medium of density ρ relative to water, is equal to TAR(ρd, ρr), i.e., the tissue-air ratio in a unit density medium for field size ρr and depth ρd. The ETAR correction factor for homogeneous, non-unit-density water-like medium is defined as

$$ICF = TAR(\rho\, d, \rho\, r) \,/\, TAR(d, r) \tag{18}$$

The application of ETAR method to *heterogeneous* geometries is given by:

$$ICF = TAR(d', \tilde{r}) \,/\, TAR(d, r) \tag{19}$$

where d' and $\tilde{r}$ are the "scaled" or "effective" values of d and r respectively for the energy of the radiation being used.

d' is derived by averaging CT values along primary photon ray paths [similar to the effective pathlength methods, see equation (14)]. In the original ETAR method, the derived electron density matrix, which comprises 256×256 elements, is reduced to 128×128 elements by averaging adjacent pixels. The

summation is carried out in this 128 × 128 matrix, which coincides with the plane of calculation.

The scaled beam radius is given by

$$\tilde{r} = r \cdot \tilde{\rho} \tag{20}$$

with

$$\tilde{\rho} = \frac{\sum_i \sum_j \sum_k \rho_{ijk} W_{ijk}}{\sum_i \sum_j \sum_k W_{ijk}} \tag{21}$$

where the summation is over the whole of the irradiated volume. The ρ_{ijk} is the relative electron density of an element (pixel) in each of the 32 × 32 (reduced) matrices (CT images). The coordinate system has been set up such that the Y-axis is parallel to the central ray of the radiation beam and the origin of the coordinate system is at the center of the region of interest. Indices i, j, k refer to X, Y, and Z coordinate, respectively.

Determination of Weighting Factors

The W_{ijk} is a weighting factor, proportional to an element's contribution to the scattered radiation arriving at the point of calculation. Wijk will, in general, be largest for voxels (volume elements) that are close to and in front of the point of calculation and smallest for pixels that are far away or behind. The weighting factors depend on the conditions of irradiation, the irradiated medium, and the location of the point of calculation. Thus, a different set of weighting factors is needed for every point of calculation. No general set exists (i.e., the weights are not spatially invariant in the language of the superposition principle).

Several approaches might be used to determine values for weighting factors. In Sontag and Cunningham work[109,192] use is made of differential scatter-air ratios (dSAR). The procedure is facilitated by separately determining the first and multiple scatter components. The weighting factor is a set equal to a sum of the two components:

$$W_{ijk} = \Delta S_1(d, r) + \Delta S_M(d, r) \tag{22}$$

where ΔS_1 and ΔS_M denote the first and multiple scatter components respectively. The first scatter estimate is derived from the Klein-Nishina Compton scattering probabilities and the multiple scatter component is based on measured SAR values.[109]

Determination of the average density $\tilde{\rho}$ requires a summation such as in equation (20) over the entire irradiated volume each time a point is calculated would necessitate use of all of the (32 × 32) matrices. In the development of a dose calculation system to be used routinely in the clinic, such a summation is

possible but was deemed impractical because of excessive computer memory requirements and calculation times (in 1970s).

As a result, an **approximate** procedure needed to be developed in which the volume is divided into parallel and contiguous slices, perpendicular to the Z-axis (along the patient's superior-inferior axis). Every volume element in a given slice has the same k coordinate. It is assumed that the weighting factor $W_{i,j,k}$, which is a function of the X, Y, and Z positions of the volume element, can be approximated by a product of two independent weighting factors, both determined for a water medium. This has allowed the reduction of the volume summation to a planar summation and is also compatible with the use of data obtained from CT slides:

$$W_{i,j,k} = W_k \,.\, W_{i,j} \tag{23}$$

W_k is a function of the Z position (i.e., assumed constant with respect to X and Y) and is intended to express the relative importance of the kth slice's contribution to the scatter dose at the point of calculation. $W_{i,j}$ expresses the relative importance as a function of the X and Y positions (i.e., assumed constant with respect to Z). Thus, W_{ijk} values are evaluated by decomposition into Wk for each CT slice and W_{ij} within the effective scattering slice.

Since W_k is taken as constant (with respect to i and j) $\tilde{\rho}$ could be written as

$$\tilde{\rho} = \frac{\sum_i \sum_j \tilde{\rho}_{ij} W_{ij}}{\sum_i \sum_j W_{ij}} \tag{24}$$

with,

$$\tilde{\rho}_{ij} = \frac{\sum_k \tilde{\rho}_{ijk} W_k}{\sum_k W_k} \tag{25}$$

Determination of $\tilde{\rho}_{ij}$ results in a "coalescing" procedure, in which the volume (all the density data of adjacent CT slices) has been reduced to a single effective slice from a photon scatter perspective (unshaded slice on the right portion of the Figure 13). The final ICF was therefore determined from integration of scattered contribution of an area rather than the actual volume.

W_k is determined by taking the difference between two scatter-air ratios for water, so that:

$$W_k = S(d_{ref}, r_2) - S(d_{ref}, r_1) \tag{26}$$

where r_2 and r_1 are the radii of "equivalent" circular beams, related to Z and X, the width of the beam in the plane of calculation. d_{ref} has been arbitrarily

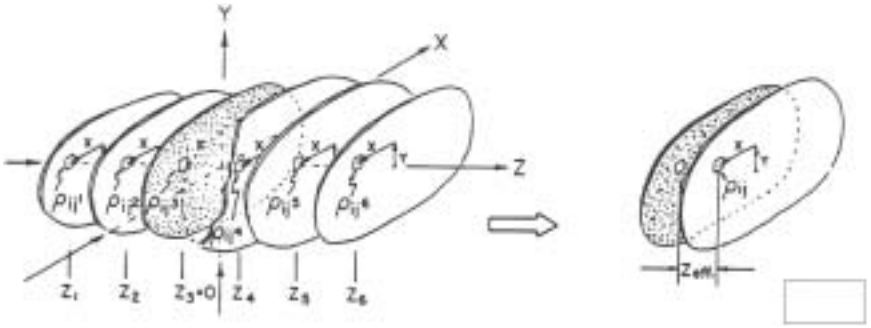

Figure 13. Schematic diagram to illustrate the steps taken in evaluating the "average density" for scattered radiation. In practice, slices are chosen to cover the entire irradiated volume. Here, six slices are shown and are irradiated from above. The densities in all six slices first are coalesced to form an effective slice as shown by the non-shaded slice on the right. This slice is made up of density elements ρ_{ij} and is considered to be at distance Z_{eff} away from the plan of calculation. For the final step, a weighted average is formed for each point of calculation from all of these elements. (Reprinted from M. R. Sontag and J. R. Cunningham,[152] "Clinical application of a CT based treatment planning system," *Comput. Tomogr.* 2:117–30 (1978a) with permission from Pergamon Press.)

chosen as an average depth, to be 10 cm (however even for extreme cases, the correction factor calculated will vary by less than 1%, regardless of the d_{ref} chosen).

This coalesced slice of varying mean density is assumed to be positioned at a distance Z_{eff} away from the plane of calculation. Z_{eff} is the position within the irradiated volume at which the scatter dose to the point of calculation from all the volume elements with a Z coordinate less than Z_{eff} is equal to the scatter dose from all the volume elements with a Z coordinate greater than Z_{eff}. Thus, Z_{eff} can be interpreted as the mean position from which scatter originates: by assigning a weighting factor, w_k, to each slice with the result that the coalesced slice consisted of pixel values with the weighted average of all pixel values along lateral axes lines that have the same *i* and *j* indices. It is further assumed that the inter-space between the effective scatter slice and the calculation plane is composed of water.

Z_{eff} is thus calculated as follows:

$$Zeff = \frac{\sum_k Z_k W_k}{\sum_k W_k} \tag{27}$$

where the summation is over k, those slices actually irradiated by the beam, and Z_k is the distance from the plane of calculation to the k^{th} slice.

The "coalescing" procedure needs to be performed only one time for each beam of radiation. In contrast, the calculation of the weighted average and the corresponding equivalent beam radius and, therefore, the equivalent tissue-air ratio must be repeated for each point of calculation within the plane of calculation: a summation is performed for all the elements of density $\tilde{\rho}_{ij}$ in the effective scattering plane over X and Y, yielding the weighted average density, $\tilde{\rho}$. As such, for a given energy, a set of weighting factors unique for each depth and field size must be calculated.

In most software implementations, the coalescing of adjacent CT slices renders a 3D problem into a 2.5D form. More recently, the W_{ijk} factors have not been decomposed and the full 3D CT data set is retained, without coalescence (Theraplan-Plus, MDS-Nordion). This is expected to improve the performance of the method if the W_{ijk} weights are determined by more detailed ray tracing through the inhomogeneous CT voxels.

Scatter Kernels: the "scatter kernel" or spatial pattern of energy which is spread (mainly) downstream from an interaction voxel resembles a water droplet in its shape (see Figure 14). This can be interpreted from two points of view: (1) as iso-contributions from upstream scattering points to a destination dose point (i.e., a receiver's viewpoint) as used by Sontag and Cunningham[192] or (2) as the energy spread from a scattering point to downstream voxels (i.e., a sender's viewpoint).

Using reciprocity,[49] it can be shown that for a particular mechanism of energy spread, such as single Compton scattering in water, the scatter kernels are indeed equivalent to the scatter weights ($W_{i,j,k}$). The scatter kernels for an all-water absorber can be derived from either theoretical considerations,[114] Monte Carlo simulations[72,108] or empirical data.[112] The real challenge therefore is to correct these kernels, or equivalently the $W_{i,j,k}$ weights for the effects of the varying density and atomic number of neighborhood tissues. Many of the methods discussed below have approached this problem starting from a different database and using one of the two equivalent perspectives of "receiver" or "sender" of scattered radiation.

The ETAR method has been reduced from a complex and time-consuming calculation into a practical and useful method by making a number of assumptions. These assumptions have been assessed in some detail by Yu and Wong[193] and Martel et al.[194] The methodology always predicts a decrease in scatter when the density is less than unity and an increase in scatter when the density is greater than unity.[195] This is not always true, especially with small low-density cavities upstream that can increase the primary fluence in shadowed voxels causing an indirect increase in scatter. Nevertheless, the ETAR model is powerful because it guarantees that the calculation will be correct for any homogeneous medium of non-unit density (i.e., satisfies O'Connnor's theorem as a constraint), provided that the effects due to atomic number variations are negligible.

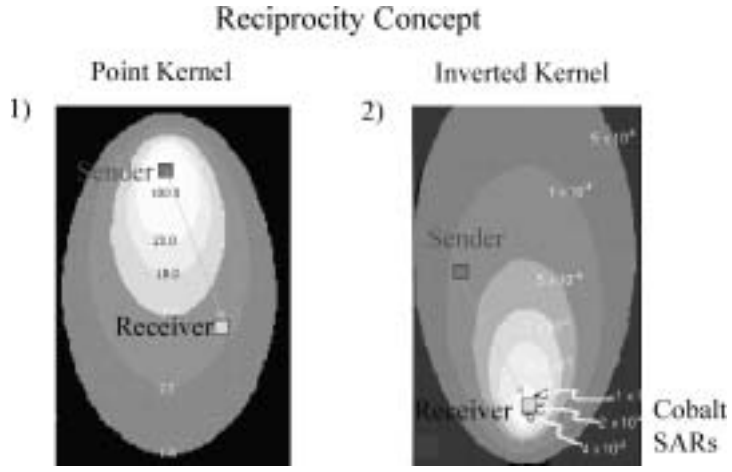

Figure 14. The "scatter kernel" or spatial pattern of energy which is spread (mainly) downstream from an interaction voxel resembles a water drop in its shape. This can be interpreted from two points of view: (1) as iso-contributions from upstream scattering points to a destination dose point (i.e., a receiver's viewpoint) or (2) as the energy spread from a scattering point to downstream voxels (i.e., a sender's viewpoint).

While the ETAR method is superior, in some instances, to the RTAR and power law methods, it is much slower in speed performance. Speed enhancement of the ETAR method has been proposed by Yu and Wong.[193] By assuming the invariance of the weighting factors, W_{ijk}, these investigators have been able to make fast 3D ETAR calculations using the fast Fourier transform (FFT) technique which improves the practical application of the method for 3D treatment planning. In this approach, the W_{ijk} are essentially the scatter kernels for an all-water absorber used in a convolution integral. The CT voxel densities are, however, used fully in correcting for the changes in TERMA.

Recently, Engelsman et al.[196] have tried to assess the limitations of treatment planning of lung tumors, calculated by some simple tissue inhomogeneity correction algorithms including the ETAR method. Single multileaf collimator-shaped photon beams of 6, 8, 15, and 18 MV nominal energy were used to irradiate a 50 mm diameter spherical solid tumor, simulated by polystyrene, which was located centrally inside lung tissue, simulated by cork. One of the main findings of their study is the quantification of the difference between the actual penumbra broadening and that calculated by ETAR, Power Law, and EPL correction algorithms. Those algorithms predict almost no penumbra broadening independent of the photon beam energy. Wong et al.[197] studied the

effects of air cavities on x-ray dose distribution at 6 and 25 MV. Measured dose was then compared to calculated dose using Clarkson sector integration and ETAR algorithms. Both algorithms show errors in dose calculation at the distal surface of air cavities mainly because they fail to account for the effect of electron disequilibrium. Du Plessis et al.[185] have compared the Batho and ETAR dose calculation methods in CT based head/sinus, lung, and prostate patient models for 2×2, 5×5, and 10×10 cm^2 open x-ray beams. The EGS4-based BEAM code was used to construct a generic 8 MV accelerator to obtain a series of x-ray field sources. Their results indicated that the Batho and ETAR methods contained inaccuracies of 20% to 70% in the maxillary sinus region in the head model. Large lung inhomogeneities irradiated with small fields gave rise to absorbed dose deviations of 10% to 20%. It is also shown for a 10×10 cm^2 field that the program DOSXYZ models lateral scattering in lung, which is not modeled by the Batho and ETAR methods. All the calculations were evaluated against the Monte Carlo simulations.

Method 2.2: Differential scatter-air ratio (dSAR)

As early as 1968, Beaudoin[198] showed that it was possible to use scatter-air ratios, cast in a differential form, to calculate the dose to a point in an inhomogeneous medium. In this method the scatter contribution that arises from voxels within the irradiation volume is determined by a scatter-air ratio table, which has been differentiated numerically in the depth and lateral r directions. The scatter from such an elemental volume ΔV is dependent on five parameters[199]: (i) the attenuation of the primary *en route* to the scattering volume ΔV; (ii) the number of photons per electron of ΔV emitted; (iii) the attenuation and geometrical dispersion of the scattered photons; (iv) the absorbed dose per unit fluence; (v) the electron density of the volume ΔV.

The integration that is performed is very analogous to a first scatter integration over volume except that differential scatter-air ratios are used in place of scattering cross sections.[109] When developed in 1968, this method was well ahead of its time, years prior to CT scan availability. However, due to the slowness of computers, the time required to do a three-dimensional integration and the lack of availability of patient-specific CT density data, the method was never implemented clinically.

Method 2.3: Delta volume (DVOL)

Wong and Henkelman,[116] and Wong et al.[200] proposed a further improvement on the semi-empirical approach of the dSAR method in 1983. They first considered a primary and an analytical first scatter calculation and, then, a term containing SARs and a residual scatter component determined experimentally. They proposed two limiting conditions that should be met by all photon dose calculation algorithms: accurate prediction of dose for: (i) the effect of a small

air void within a unit density medium (i.e., their experimental setup); and (ii) the homogeneous, non-unit density medium (i.e., O'Connor's theorem).

The first order scatter ray tracing is, in principle, more complete than the ETAR density scaling scatter model. DVOL calculations have been shown to agree with measurements to better than 3% for complex mediastinum geometries in which the dose point is in between two laterally placed lung volumes, if the condition of electron equilibrium holds. Unfortunately, the improved accuracy comes with very long calculation times due to the nature of 3D volume integration and the relatively low computational power of the 80s.[201] To the best of our knowledge, this method is not used clinically.

Method 2.4: Differential tissue-air ratio method (dTAR)

Kappas and Rosenwald,[199,202] have found that a simplification of the differential scatter-air ratio method (dSAR) proposed by Beaudoin[198] applied to a slab geometry gives more accurate results than the original method. Thus, a method, which takes advantage of this simplification has been developed, called the "differential tissue-air ratio method (dTAR)". The simplification of the dSAR method essentially consists in suppressing the multiplicative factor $K(\theta, \mu) = \exp[(\mu_0 \cos\theta - \mu_1(\theta)](\underline{b} - b)$ which accounts for the lateral distance between the primary interaction and the calculation point. The quantities μ_0 and $\mu_1(\sigma)$ are the linear attenuation coefficients in water of the primary and of the first-order scattered photons arriving at point after a scattering of angle q; b is the path length *en route* to point M (in the waterlike medium) and $\underline{b}$ is the corresponding effective path length (in the heterogeneous medium). Consequently, for a density less than unity, if one uses $K(\theta, \mu) = 1$ for all volume elements, the total first scatter contribution (first and multiple arising from each voxel ΔV in the medium) will be reduced compared to the original dSAR method.

The dTAR method:

- does not require any specific measurements or predetermination of voxel scatter data, the only data actually needed being geometrical distances and standard TAR values.
- it is an additive approach accounting for all the layers located in front of the calculation point, one layer at a time.
- leads to calculation times not significantly longer that the conventional methods.
- provides similar results to the power law (Batho) method, although it seems to be slightly better for large fields within lung inhomogeneities.

The method generally shows an agreement better than 1.5% for on-axis points and for the majority of situations as long as the electron equilibrium is achieved. The dSAR method makes the assumption that the introduction of an inhomogeneity causes the first and multiple scatter components of radiation to change by the same ratio. Thus, for very large fields and depths and when the

overlying tissue is thick (over 5 cm), the discrepancy between measurements and calculations is greater than 2% but less than 6%.[202]

Method 2.5: 3D beam subtraction method

The 3D beam subtraction method (3D-BSM) proposed by Kappas and Rosenwald,[183,202] tries to ameliorate the methods of category 1 by taking into account that (i) the point of calculation is not necessary located on the beam-axis, (ii) the primary is not always affected by the presence of the inhomogeneity, (iii) the lateral dimensions of the inhomogeneity could be smaller than the field dimensions. The method consists of using a mathematical combination of on-axis conventional (category 1) correction factors. Each factor is calculated according to the actual size and position of the inhomogeneity relative to the calculation point and the beam geometry. The method is originally based on Day's formula,[203] where in a rectangular 2X*2Y field the dose at any off-axis point P can be computed as the average between the dose contributions from four independent rectangular sections located around P.

The 3D-BSM is characterized by the fact that: (i) it assumes that the patient's internal structure can be represented in terms of macroscopic volumes of tissues of different but uniform "effective" densities (i.e., contoured or segmented regions); (ii) the shapes of inhomogeneities are approximated by parallelepipeds; (iii) the algorithm defines several "inhomogeneous" parallelepipeds (alternatively crossed or not crossed by the primary ray) for each inhomogeneity; (iv) their limits are adjusted as a function of the relative position of the calculation point and the inhomogeneity according to the beam direction.

The global correction factor is therefore

$$ICF = 1 + \frac{\sum_{i=1}^{2}(-1)^{i}\sum_{j=1}^{2}(-1)^{j}\left[\varepsilon'_{ij}\left(c_{ij}-1\right)D_0^w\left(U_i,W_j\right)\right]}{\sum_{i=1}^{2}\sum_{j=1}^{2}\varepsilon_{ij}D_0^w\left(x_i,y_j\right)} \qquad (28)$$

where ε'_{ij} is the sign of the product U_i,W_j, U_i and W_j represent the algebraic distances from point P to the inhomogeneity limits, $D_0^w\left(U_i,W_j\right)$ is the dose at the center of the corresponding rectangular field in the absence of the inhomogeneity. C_{ij} is the on-axis conventional correction factor (category 1) for the field U_i and W_j.

Using the described method, observed errors between experimental data and calculated correction factors are attributed, on one hand, to the accuracy of the on-axis correction factor (C_{ij}) and on the other hand, to the simplifications specific to this method.

It is assumed that the scatter arising laterally from the homogeneous regions is not modified by the presence of the inhomogeneity. This assumption is less and less valid as the inhomogeneity is larger and its electron density more dif-

ferent from unity. In the case of $\rho_{het} < 1$, the importance of the lateral scatter is thus theoretically underestimated and so is the corresponding correction factor.

On the other hand, if one considers a parallelepiped located laterally at proximity from an inhomogeneity ($\rho_{het} < 1$), the interaction between this parallelepiped and the inhomogeneity results in a lack of scatter (second order scatter and above). This is not taken in account in this method, which assumes that, each parallelepiped behaves independently from the others. It should therefore result in an overestimation of the calculated correction factor.

The method is very fast and comparable in performance with the Batho method with no additional data requirements. The 3-D BSM method is implemented in the "3D-ISIS" treatment planning system ("Technologie Diffusion", Institute Curie, Paris, France).

Category 3: Non-Local Energy Deposition (Electron Transport); 1D Density Sampling

The methods of category 1 and 2 are more applicable to photon beams with energies less than 6 MV where electron equilibrium is assumed to hold and where the photon scatter contribution is greater. However, they are not well suited for higher energy photon beams where the scatter contribution is less important and the effects of electrons set in motion by the photons can lead to very high dose changes locally.

Method 3.1: Convolution techniques

Several models,[107,119,125,129,204,205,206,207,208,209,210,211,212,213] have been developed in recent years that focus on the transport of secondary electrons arising from primary photon interactions. Analytic approximations or Monte Carlo simulations are used to model the energy deposition distribution from the site of photon interaction in water, forming a dose spread kernel that is then adjusted for the inhomogeneous patient medium. Scattered photon dose kernels are also generated with or without the assumption of local energy deposition.

Convolution techniques get their name from the mathematical expression (section IIIF) that governs the dose calculation algorithm. In essence, the energy fluence distribution is convolved with the scatter spread kernel to obtain dose. Energy deposition kernels represent the response of the medium; commonly water, to an incident elementary radiation. Pencil beam kernels have long found widespread applications in electron dose calculation algorithms. For a monoenergetic photon beam the energy deposition by secondary particles from the primary interaction site is independent of the geographic location of the site (in homogeneous media) and thus convenient to be described by a kernel. Although three-dimensional in nature, the kernels can be integrated (prior to the convolution) in one or two dimensions, giving rise respectively to a pencil beam kernel and a planar spread function (Figure 15). This is analogous to the

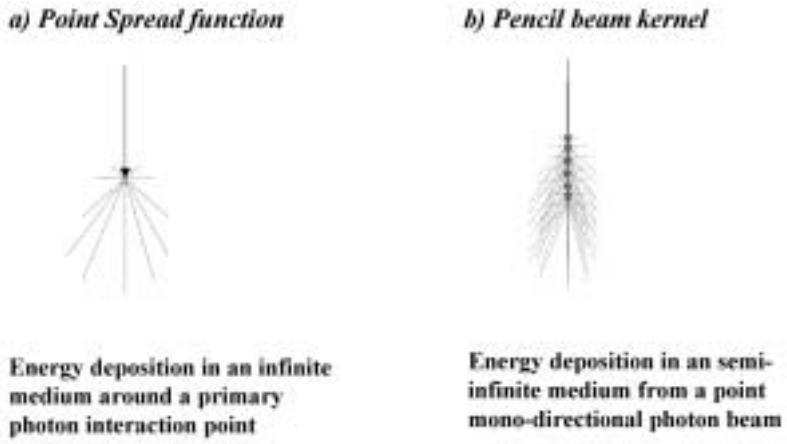

Figure 15a. Scatter kernels of different dimensions.

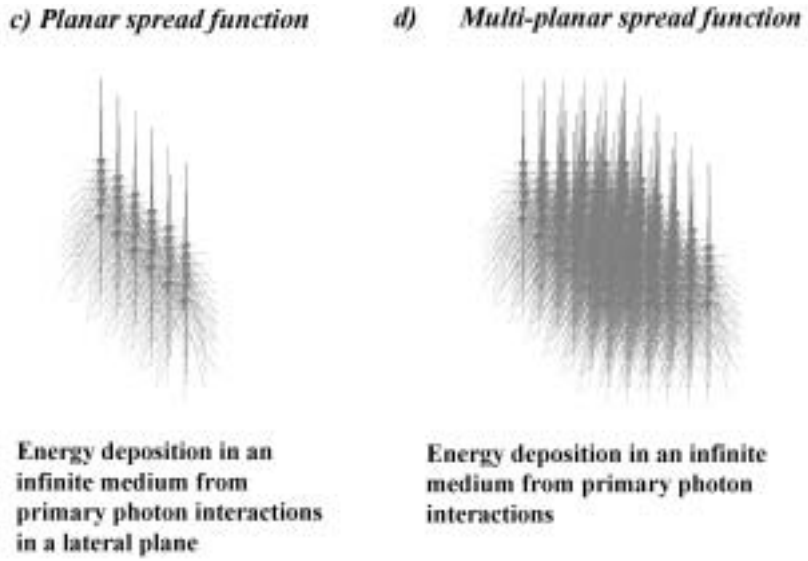

Figure 15b. Scatter kernels of different dimensions.

collapsed ETAR implementation that was discussed earlier, and aims to simplify the calculation and reduce the computation time at the expense of reduced accuracy in the presence of inhomogeneities. An example of such a photon pencil beam algorithm is now used commercially (Bruinvis, Nucletron, MDS Nordion) for external beam dose calculations.

Method 3.2: Fast Fourier Transform (FFT) convolution

The FFT convolution method introduced by Boyer et al.[134] is given for a polyenergetic beam spectrum as

$$D(\vec{r}) = \sum_{n} \int_{v} \Phi_n(\vec{r}\,') \cdot K_n(\vec{r} - \vec{r}\,') dV' \tag{29}$$

where:

$K_n(\vec{r} - \vec{r}\,')$ is the dose spread kernel for the nth energy interval, and

$\Phi_n(\vec{r}\,')$ is the spectrally weighted primary fluence given by equation (25).

$$\Phi_n(\vec{r}\,') = \Phi_n^o(\vec{r}\,') \cdot e^{-\int_0^r \mu_n(\vec{r}) d\vec{r}} \tag{30}$$

where:

$\Phi_n^0(\vec{r}\,')$ is the primary energy fluence.

In the inhomogeneous medium, a relatively simple 1D anatomy-sampling model is used which corrects for the primary fluence or TERMA. The first scatter-spread kernel is adjusted for the primary fluence at the point of interaction and for the density of the interaction site. The same 1D information is used for making a first order adjustment of the first and higher order scattered photon dose contributions. In the Boyer FFT method, the separation of the primary and scattered corrections provides noticeably improved results over the earlier 1D models. In the semi-infinite slab inhomogeneous geometries irradiated with cobalt-60, the calculations rival those using ETAR or DVOL methods. Poor results were observed with aluminum inhomogeneity because the effects of atomic number changes are not addressed by the model. Recent refinements to this model scheme have been introduced independently by various workers.[193,214,215,216,217,218,219,220]

With simplifying approximations, the convolution (assuming invariant kernels) can be implemented using techniques such as the FFT algorithm to greatly reduce computation time. These methods can compute the dose very accurately in areas of electronic disequillibrium due to build-up and build-down effects (e.g., entrance and exit dose, dose at the edge of the radiation field, and dose under the beam blocks). While these are not internal inhomogeneity effects, they are significant, especially as the radiation fields become more collimated both in conformal and in IMRT planning and delivery.

Category 4: Non-Local Energy Deposition (Electron Transport); 3D Density Sampling

This category of inhomogeneity correction methods employs complex models to incorporate 3D density CT information for the transport of both scattered

photons and electrons. These methods include the dose spread array (DSA) method by Mackie et al.[107], the differential pencil beam (DPB) method by Mohan et al.[108], the convolution method using total energy released in the medium (TERMA) concept of Ahnesjo et al.[55] and the forward and backward scatter transport model of Iwasaki[221,222,223] (in 1D). More recently Woo et al.[94] extended the ETAR method to include electron transport in what has been now implemented in Theraplan-Plus (MDS-Nordion).

Method 4.1: Superposition-convolution methods

A number of authors have studied the application of the superposition and convolution principles to dose calculations in radiotherapy. The underlying challenge is to account for tissue inhomogeneities that deform both the TERMA distribution and the dose spread kernels. Tissues that lie along the primary ray lines from the radiation source(s) directly influence the TERMA at each point in the patient. Most methods of dose calculation account correctly for this variation in primary energy fluence. The primary beam penetration is calculated by ray-tracing[151,160,224] through the voxel densities in the 3D volume along divergent beam ray paths.

Figure 4 showed how photon energy fluence (and hence the TERMA) and the dose could be quite different and how these differences can be explained by the superposition principle.[56,110,225,226] This example showed distributions for a small field (5×5 cm) of 5.0 MeV x-rays incident on an all-water phantom and a slab phantom consisting water, low-density cork (=0.3g/cm^3), and water. An increased penetration through the low-density material is observed (Figure 4b vs. Figure 4a). The fluence distributions exhibit very sharp field edges because the blurring due to scattering in the phantom is not yet included in this first stage (TERMA) of the calculation. In the second stage (DOSE), the spread of energy by secondary particles is considered. The fluence patterns (Figure 4c and Figure 4d) become blurred by the energy spreading within the phantom, exhibiting an initial build-up region starting at the beam entrance surface, and a penumbra developing near to the beam edge. In this heterogeneous medium, the spatial extent and shape of the dose spread kernels $K(r';r)$ is deformed by the local density environment for each superposition point, and the dose distribution is considerably broadened in the low-density zone (Figure 4d vs. Figure 4c). Furthermore, an unexpected effect in which the central dose is actually reduced within the lung, in opposition to the elevated fluence (Figure 4d vs. Figure 4b) is also observed. This build-down effect is due to a disruption of charged particle equilibrium. Because the lateral range of charged particles increases in the low-density medium, more electron energy is "out-scattered" laterally than is "in-scattered" because of the small field size (5 cm $\times$ 5 cm). This effect is strongly influenced by the beam energy and the density of the tissues irradiated and to a smaller extent by the finite size of the x-ray source.[96] The overall effect upon a single beam dose distribution is illustrated in 3D for an 18 MV x-ray beam (5 cm $\times$ 5 cm) in Figure 16. This figure shows a simu-

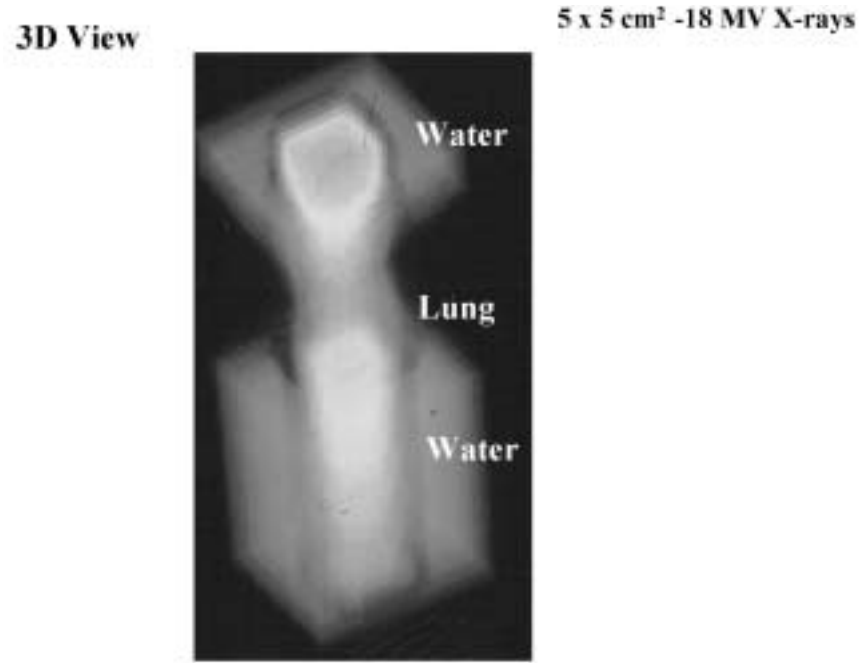

Figure 16. 3D single beam dose distribution for an 18 MV x-ray beam (5 cm × 5 cm). Because the lateral range of charged particles increases in the low-density medium, more electron energy is "out-scattered" laterally than is "in-scattered" because of the small field size.

lated water/lung/water phantom where the beam is incident perpendicularly from the top. The colors correspond to relative units of dose in a thermal scale, red being the highest level. Reliance on a simple consideration of the primary radiation alone (i.e., TERMA only in Category 1 and 2 algorithms) can yield misleading dose predictions under some clinical situations, such as lung exposed to small fields of high-energy (> 10 MV) x-rays.[35,227]

As was described earlier, the convolution/superposition calculation has two elements to it. The TERMA part that describes the distribution of the energy that is released at a primary interaction site and is available for consumption in the medium and the kernel part that describes the distribution of the scatter from a primary interaction; in essence the kernel dictates how the TERMA is going to be distributed in the medium. Starting with Monte Carlo or analytically generated dose spread kernels as input, both the primary and first order scatter ray tracings are used to process the 3D density information. The equation for the TERMA element (T) of the convolution method is given by

$$T(\vec{r}\,') = \frac{\mu}{\rho}(\vec{r}\,') \cdot \Psi(\vec{r}\,') \tag{31}$$

The convolution/superposition is then simply the integration of the TERMA distribution multiplied by the kernel over the entire patient volume. Since the indexing is performed in radiological space (density*distance) the mathematical expression of the integral is:

$$D(\vec{r}) = \int T(\vec{r}' \cdot \rho') \cdot K(\vec{r} \cdot \rho; \vec{r}' \cdot \rho') d^3\vec{r}' \tag{32}$$

In general, the effective density calculated along the scattered ray path is used to change secondary particle contributions or to look up the appropriate value in the scatter kernel using density scaling. The latter holds for all orders of photon scatter and is a good approximation of electron transport. These methods are by far the most complete of all inhomogeneity correction methods discussed thus far. Excellent results have been demonstrated for a variety of difficult low-density inhomogeneous media. The 3D implementation of convolution superposition algorithm can operate in three modes that include electron transport where: (i) both the TERMA and the kernel are scaled by density (equation 32); (ii) only the TERMA includes the density distribution, while the kernel does not; and (iii) both TERMA and the kernel assume that the patient is homogeneously made of water. Some clinically relevant results are shown in Figure 17.

Several computation time reduction schemes have been implemented from the use of variable calculation resolutions to the "collapsed cones"[106] for reducing the scatter ray trace burden. TERMA distributions are generated and calculated and then convolved with either analytical or Monte Carlo generated kernels that account for scattered photons and transport of charged particles.[72,209] The TERMA array is weighted to account for the polyenergetic nature of the beam,[228] as is correction for kernel tilting with beam divergence.[209]

Figure 17. 3D implementation of convolution superposition algorithm: (i) both the TERMA and the kernel are scaled by density [Equation (32)]; (ii) only the TERMA includes the density distribution, while the kernel does not; and (iii) both TERMA and the kernel assume that the patient is homogeneously made of water.

The collapsed cone convolution method uses an analytical kernel represented by a set of cones, the energy deposited in which is collapsed onto a line (hence the name). In practice, the method utilizes a lattice of rays, such that each voxel is crossed by one ray corresponding to each cone axis. TERMA is calculated at regular points along each ray and the resulting energy directed into the associated cone is used to increment the dose deposited at points along the ray (via the kernel parameters for that ray angle). Dose at a point is the sum of contributions from each such ray (one for each cone angle), where dose due to each ray is an accumulation of the effect of TERMA at all points on the ray. The polyenergetic spectrum is accounted for in the TERMA calculation via an effective attenuation coefficient, and there is an empirical correction to account for the fact that the kernel parameters do not vary as the primary beam hardens with depth.[209] Adaptive and full collapsed cone options exist. The adaptive variant uses a dose gradient difference method to reduce the time of calculation.

The collapsed cone method proposed by Ahnesjo[106] applies an angular discretization of the kernel that enables an efficient approach for energy transport and deposition. The geometry is shown schematically in Figures 18a and 18b.

In order to simplify the use of kernels, analytical fitting has been proposed for point kernels[106,229] and for pencil kernels by Ahnesjo et al.[128] The approach used by Ahnesjo for polyenergetic point kernels was to model the kernel as mediated by rectilinearly transported particles with exponential attenuation and inverse square divergence according to

$$h(r) = \frac{\mathrm{A}_\theta e^{-\alpha_\theta} + \mathrm{B}_\theta e^{-b_\theta}}{r^2} \tag{33}$$

where A_θ, a_θ, B_θ, and b_θ are fitting parameters depending on the scattering angle θ. The first term mainly describes the primary and the second term the scatter dose fraction.

Angular discretization of a parameterized point kernel yields, for each discrete angular sector (cone) Ω_i, the energy deposition per radial distance as

$$\iint_{\Omega_i} \frac{h_{\rho_0}}{\rho}(r,\Omega) r^2 d^2\Omega = \mathrm{A}_{\Omega_i} e^{-\alpha_{\Omega_i} r} + \mathrm{B}_{\Omega_i} e^{-b_{\Omega_i} r} \tag{34}$$

Notice that the inverse square of the radius cancels due to the increasing cross section of the cone Ω_i with increasing radius. When the angular discretized kernel is convolved with the terma distribution, all energy released into the cone direction Ω_i from volume elements on the cone axis is approximated to be rectilinearly transported, attenuated, and deposited in volume elements on that axis; i.e., the cones are collapsed onto their axes (see Figure 18a). A lattice of transport lines, representing cone axes, is constructed to cover the irradiated volume such that each direction intersects every calculation voxel. This requires a parallel subset of lines for each discrete direction of the "collapsed" kernel, which can be arranged in several ways.[104,106,230,231]

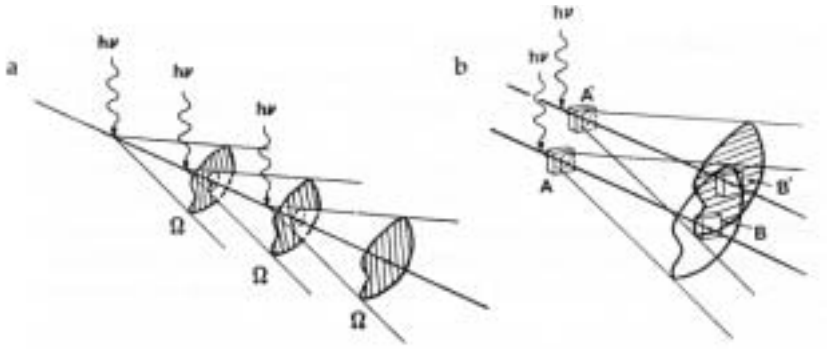

Figure 18a. A consequence of the collapsed cone approximation to transport the energy along a discrete axis is that the energy that should have been deposited in voxel B′, from interactions at the vertex of the lower cone, is deposited in voxel B and vice versa. This displacement grows with distance; however, the first scatter fraction decreases with increasing distance, making the approach acceptable as the total energy deposited is conserved. Most energy is deposited close to where it is released, making displacement errors less important since it takes place mainly within voxels, as shown by the voxels A and A′ (Reprinted from A. Ahnesjo,[106] "Collapsed cone convolution of radiant energy for photon dose calculation in heterogeneous media," *Med. Phys.* 16:577–92 (1989) with permission from the American Association of Physicists in Medicine.)

Because of the exponential description of the kernel, the energy transport along a line can be expressed analytically resulting in recursive formulae that only need to be evaluated once for each voxel on that line. Kernel scaling for the heterogeneities is performed during the recursion, both for the primary and scatter dose kernels [i.e., both terms in equations (33) and (34)]. The recursions pass each voxel at least once per direction. When each point is calculated individually, the number of operations will be proportional to MN^4, where M is the number of conical sectors (angular bins). If instead the dose is calculated in one sequence for a bulk of N^3 points, the total number of operations needed in heterogeneous media is proportional to MN^3. In a similar method Reckwerdt and Mackie[231] bypassed the exponential parameterization by using the result of an initial ray-trace along each transport line to look up the radiological distance between each pair of release/deposition points. This results in an MN^4 algorithm, because for each point the other points on the same line have to be visited separately. The collapsed cone method has been implemented in commercial systems (e.g., MDS-Nordion, Helax).

Figure 18b. Example of a simple lattice of cone axes made to cover the $3 \times 3 \times 3$ calculation voxels with the 26 discrete cone directions used in this case. In this example all transport lines intersect at each voxel center but this is not required as long as each voxel is intersected by each direction (Reprinted from A. Ahnesjo,[106] "Collapsed cone convolution of radiant energy for photon dose calculation in heterogeneous media," *Med. Phys.* 16:577–92 (1989) with permission from the American Association of Physicists in Medicine.)

Method 4.2a: Monte Carlo method: overview

The Monte Carlo method provides a bridge between measurements and analytically based numerical calculations (see reviews of Monte Carlo applications in medical physics by Andreo,[232] Rogers and Bielajew,[233] and Mackie[234,235]). These three techniques provide complementary descriptions and each would be less useful or credible without the contribution of the other two. Experimentation and simulation result in the distillation of insight by a careful choice of parameters to be measured in one case and "scored" or tabulated in the other. Monte Carlo calculations provide a benchmark for analytic calculations and a verification of results obtained in difficult measurement situations. In turn, Monte Carlo calculations are built on the foundations of measured and

calculated probability distributions, for example, those describing fundamental scattering processes and energy loss.

Monte Carlo modeling is often done in situations in which physical measurements are difficult or impossible. It is possible to "synthetically measure" significant but almost un-measurable quantities such as the contribution of dose from different orders of photon scattering. While, in principle, the spectra of high-energy clinical linear accelerators can be measured, such measurements are often difficult to realize. The main difficulties in such reconstructive techniques based on measured depth dose distributions or attenuation measurements are:

(a) depth dose distributions from monoenergetic photons calculated by Monte Carlo must be available.
(b) the use of *different* constraints on the spectral shape is necessary to handle numerical conditioning problems.
(c) the dose from charged particle contamination in the build-up region complicates the use of data from that region including the depth of dose maximum.

Some authors suggest ways to unfold the accelerator spectrum from measurements; either from monoenergetic depth dose distributions[126,129,236,237,239] or based on attenuation measurements.[240,241,242,243,244,245,246]

On the other hand, Monte Carlo spectra can now be obtained relatively easily. Several workers performed Monte Carlo simulations of the treatment head for modeling radiation treatment machine heads, and generating the energy spectra and angular distributions of photon beams produced by linear accelerators and Co-60 teletherapy machines, and for studying other characteristics of photon beams.[52,53,247,248,249] This approach assumes a detailed knowledge of the materials and geometry of the contents of the accelerator head being used clinically.

The Monte Carlo technique of radiation transport consists of using knowledge of probability distributions governing the individual interactions of electrons and photons to simulate their transport through matter. The resultant distributions of physical quantities of interest from a large number of simulated particles (called "histories") provide a description on the average transport properties and the associated distributions such as the dose deposition. This is done, in general, in the following way (referring to photon interactions): from the exponential attenuation distribution, the appropriate cumulative distribution can be evaluated and the distance s between interactions in a medium (step length) is determined by:

$$s = -\lambda \ln(1 - \xi) \tag{35}$$

λ being the mean free path at the photon energy at the beginning of the step and ξ a random number, $0 \leq \xi \leq 1$. For the production of "true" random numbers, the so-called **R**andom **N**umber **G**enerators (RNGs) have been developed. All

RNGs are based upon specific mathematical algorithms, which are sequential and repeatable with a very long period. As such, the numbers are *pseudorandom*. Nevertheless, when the generator is "well-behaved," even if the sequence of numbers is used more than once, the probability of having more than one particle history starting in the same event position is practically negligible. This means that when the end of a sequence is reached, it will be started again during some of the sampling procedures used along the simulation.

The type of interaction event occurring after the step s is sampled from the appropriate relative probabilities p_i (ratios of single cross-sections to the total cross-section), using their cumulative distribution function P_i. Another random number ξ selects the interaction event $i(\xi)$ such that:

$$\sum_{i=1}^{j-i} p_i = P_{j-1} \leq \xi < \sum_{i=1}^{j} p_i = P_j \tag{36}$$

where $i(\xi)$ is the Rayleigh, photoelectric, Compton or pair production effect at the corresponding photon energy.

Different techniques exist to sample from the probability distributions describing photon interactions after the distance s. The small number of interactions that take place when photons traverse through matter has motivated the development of variance reduction techniques[53] to decrease uncertainties that can be evaluated by statistical methods. In such techniques the "natural physics" is manipulated in a number of different ways so as to increase the relative occurrence of certain events. Forced interactions, importance sampling Russian roulette, and particle splitting are commonly used techniques.

Monte Carlo techniques have become widely used in medical physics because of the massive increase in computing power in the last decades and because of the availability of powerful codes such as BEAM, EGSnrc, PENELOPE, and ETRAN/ITS/MCNP. Both trends can be expected to continue so that Monte Carlo techniques for radiation transport will only continue to increase in importance in the next decade. In the short term, the commercial application of codes such as DPM,250 MCDOSE,[251,252] or VMC++,[63] should start to make Monte Carlo a useful technique in clinical treatment planning. The VMC++ code developed by Kawrakow making use of some highly innovative variance reduction techniques including photon splitting, electron history repetition, Russian Roulette, and a technique called STOPS[253] (Simultaneous Transport of Particle Sets), can do an electron beam calculation in about 35 s on a 500 MHz machine (4 times faster machines are available today for a very affordable cost) and photon beam calculations take about 360 s.[235] DPM is capable of computing 3D dose distributions (in 1 mm^3 voxels) which agree to within 1% in dose maximum with widely used and exhaustively benchmarked general-purpose public-domain MC codes in only a fraction of the CPU time. A representative problem, the simulation of 1 million 10 MeV electrons impinging

upon a water phantom of 128(3) voxels of 1 mm on a side, can be performed by DPM in roughly 3 min on a modern desktop workstation.

Furthermore, improvements in Monte Carlo calculation speed demonstrated by the project "PEREGRINE" of Lawrence Livermore Laboratory[254] showed that real-time Monte Carlo dose calculation could be possible for all modalities, including photons. Based on the EGS4 code, Wang et al.[255] proposed to improve efficiency through the use of variance reduction techniques and density thresholding, the latter to speed up the ray-tracing calculations.

Method 4.2b: Monte Carlo: dosimetry in heterogeneous media

There are two types of tissue interface most significant in radiotherapy; namely between any low-density inhomogeneity and soft tissue and between bone and soft tissue. Interface dosimetry for prosthetic implants is the subject of a different task group report[48] although the physical processes of the interactions and the observed dosimetric changes are of the same nature. Dose perturbations at an interface are due to a number of complex effects.[75,90,91,217,256,257,258] The attenuation coefficients, the mass energy absorption coefficients, and the mass collision stopping powers are different on either side of the interface. For Monte Carlo simulation accurate charged-particle transport is important because charged particles set in motion on one side of the interface can migrate to the other side and deposit energy. Inadequate treatment of charged-particle transport will result in inaccurate prediction of the resultant "hot/cold spots" spurious effects.

Several Monte Carlo codes have been used with success in supporting, testing, or guiding the development of dose calculations for radiotherapy applications, especially for complex tissue interface problems.[64,177,181,217,257,259,260,261,262,263,264,265,266,267,268,269,270,271,272,273,274]

Mackie et al.[275] utilized the EGS code to model the dose distribution both within and distal to simulated regions of lung in order to test the ratio of tissue-air ratios (TAR), Batho, and equivalent TAR methods. Figures 19 and 20 show the central-axis dose correction factor when a 15 MV x-ray beam irradiates a heterogeneous slab phantom. When the field size is decreased, electron disequilibrium causes the central axis dose to be reduced considerably. This is observed experimentally (solid lines) and in the Monte Carlo simulation (Figure 19), but not with simpler dose algorithms (Figure 20). The curve trends are similar for the measured and Monte Carlo results (Figure 19), but there is an offset approximately 2% between measured and computed data. This discrepancy is attributed to a combination of small effects, including the use of the ion chamber under conditions of charged particle disequilibrium, mismatch of x-ray spectra, or differences in the assumed (0.25 g/cm^3) and actual density of cork. The agreement among the Monte Carlo calculation, analytical calculations, and measurements[181,259] is within about 2%. Allen Li et al., systematically studied the dose perturbation near planar and cylindrical air cavities in a water medium irradiated by megavoltage x-ray beams. The combined set of Monte Carlo calculations showed that the dose reduction near an air cavity is greater

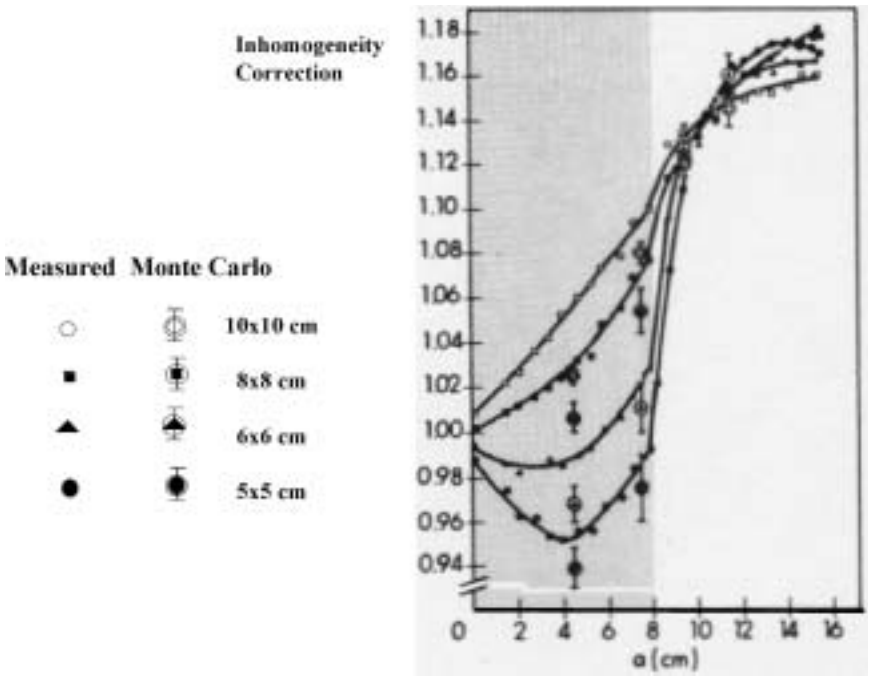

Figure 19. Comparison of inhomogeneity correction factors produced by a Monte Carlo calculation with measured data for 15 MV x-ray fields of different sizes. The solid lines are measured data while the isolated points are those obtained by a Monte Carlo calculation. Charged particle equilibrium is not established for field sizes of less than 10×10 cm^2, and there is considerable underdosage within cork. (Reprinted from T. R. Mackie, E. El-Khatib, J. J. Battista, J. Scrimger, J. Van Dyk, and J. R. Cunningham,[275] "Lung dose corrections for 6 MV and 15 MV x-rays," *Med. Phys.* 12:327–332 (1985) with permission from the American Association of Physicists in Medicine.)

for: (i) smaller x-ray field size; (ii) higher x-ray energy; (iii) larger air-cavity size; and (iv) smaller depth in water where the air cavity is situated. Notice that there is no sharp rise in dose at the first tissue-lung interface as reported by Webb and Parker.[276] Indeed, there is a small reduction in dose attributable to decreased backscatter from the low-density region. The field size was 10 cm in diameter, which is large enough to establish lateral electron equilibrium at the central axis. Therefore, the reduction of dose could not have been due to lack of lateral equilibrium.

Lateral disequilibrium of electrons can produce perturbations in dose in low-density regions in heterogeneous phantoms. Mackie et al.[275] used the EGS code to model a 0.25 g/cm^3 slab of water-like material simulating lung embedded in a water phantom. They showed that there is a reduction in dose in the

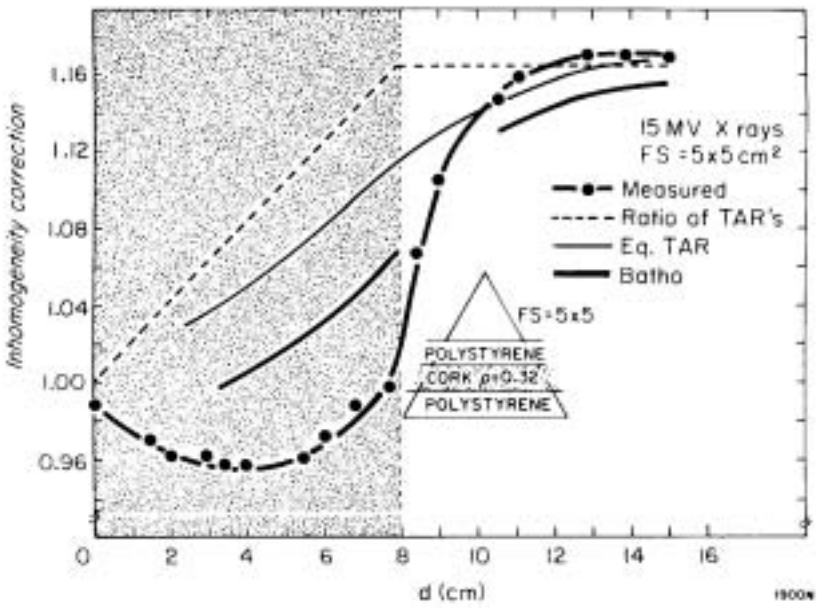

Figure 20. Results for irradiation with 15 MV x-rays and 5×5 cm^2 field. Dose measured and calculated at points along the central axis in both a homogeneous and a heterogeneous phantom composed of slabs of waterlike and lunglike materials. (Reprinted from T. R. Mackie, E. El-Khatib, J. J. Battista, J. Scrimger, J. Van Dyk, and J. R. Cunningham,[275] "Lung dose corrections for 6 MV and 15 MV x-rays," *Med. Phys.* 12:327–332 (1985) with permission from the American Association of Physicists in Medicine.)

low-density medium if the distance from the field boundary is smaller than the lateral range of electrons (see Figures 19 and 20). There is a corresponding increase in the dose outside the field.

Figure 21a shows isodose curves produced by a monoenergetic pencil beam of 5-MeV photon beam incident on homogeneous and heterogeneous phantoms. In the lung region, the lower-valued isodose lines "bulge" laterally. This could have occurred because the electrons or the scattered photons have an increased range in the lower-density medium. To prove that the effect is due to an increased electron range, the Monte Carlo calculation was repeated without and with electron transport (Figure 21b): the KERMA and the dose were calculated at a position midway into the low-density region as a function of distance from the central axis. KERMA was obtained by "turning off" electron transport; i.e., by making the cut-off energy higher than any possible electron energy. This forced the charged-particle kinetic energy to be deposited on the spot where the particle originated. The lateral spreading is attributable mainly to electrons, since the KERMA curves for heterogeneous and homogeneous phantoms are very similar.

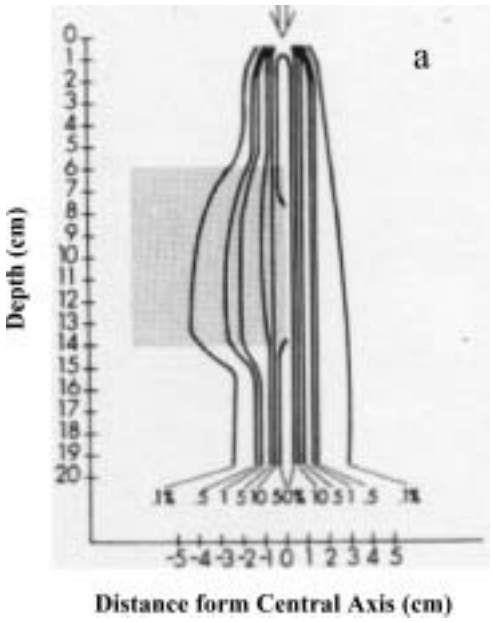

Figure 21a. Isodose curves generated by a Monte Carlo calculation for a pencil monoenergetic beam of 5 MeV photons that approximates a 15 MV x-ray spectrum. The right hand side was obtained for a homogeneous water phantom while the left-hand side is for a heterogeneous phantom with a cork slab (shaded). (Reprinted from T. R. Mackie, E. El-Khatib, J. J. Battista, J. Scrimger, J. Van Dyk, and J. R. Cunningham,[275] "Lung dose corrections for 6 MV and 15 MV x-rays," *Med. Phys.* 12:327–332 (1985) with permission from the American Association of Physicists in Medicine.)

De Marco et al.[247] have used a high-density heterogeneity phantom (from Masterson et al.[277]) consisting of a 3 cm × 3 cm × 10 cm cortical bone insert (mass density: 1.87 g/cm^3) inserted into a 25 × 25 × 25 cm^3 polystyrene support base with 28 TLD-100 rod inserts. The measurement setup for the high-density heterogeneity is based upon a field size of 10 × 10 cm^2 and a SSD of 95 cm. All data sets are normalized to a depth of 5.0 cm. Figure 22 provides a benchmark comparison between the TLD measurements, film dosimetry and MCNP4A (Monte Carlo N-Particle, version 4A)[278,279] calculations, and a conventional treatment planner for the 10-MV photon beam (the Wong-Henkelman116 correction factor is used to account for bulk heterogeneities and the equivalent tissue-air ratio (ETAR) method of Sontag and Cunningham[167] is used for CT-based correction factors). There is good agreement between the MCNP4A calculations and measurements for the three beam energies. The agreement of the conventional algorithm with film measurement and the MCNP4A calculation

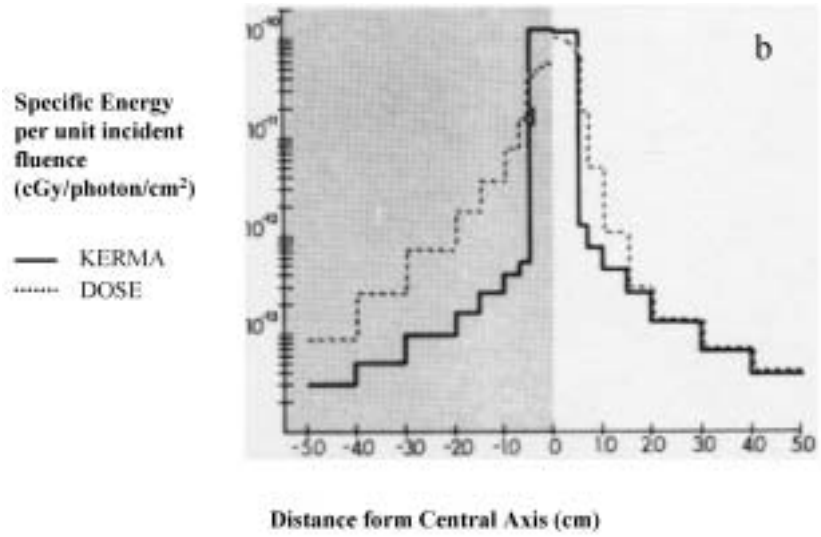

Figure 21b. Dose profile across the pencil beam at a depth (d) of 10.5 cm. The KERMA curve only considers the transport of photons while the dose curve also considers the transport of electrons away from sites of photon interaction. (Reprinted from T. R. Mackie, E. El-Khatib, J. J. Battista, J. Scrimger, J. Van Dyk, and J. R. Cunningham,[275] "Lung dose corrections for 6 MV and 15 MV x-rays," *Med. Phys.* 12:327–332 (1985) with permission from the American Association of Physicists in Medicine.)

reveals a similar trend for all three energies. Within the bone heterogeneity there is good agreement due to the normalization point, but for depths beyond the heterogeneity the conventional algorithm consistently overestimates the depth dose. At a depth of 10 cm from the surface of the phantom, the conventional system calculates a depth dose that is 5.6%, 8.9%, and 17.6% greater than MCNP4A calculated values for the 6, 10, and 25 MV photon beams, respectively. The magnitude of discrepancy may change if a different point of normalization is used for the comparison.

The bone-soft tissue interface is often modeled by an aluminum-water interface. Webb and Fox[170] calculated the dose from a ^{60}Co γ-ray beam near a water-aluminum interface using a Monte Carlo code, modified from previous work[276] to take into account the changing stopping power as the electrons slow down. Figure 23[269] shows that the dose distribution is qualitatively no what is expected. For example, there is not prediction of increased dose from backscatter. This was likely due to excluding electron scattering.

Rogers and Bielajew[280] have found quite different results with a similar geometric setup. They calculated the dose, using EGS, near a water-aluminum slab interface from a ^{60}Co γ-ray beam and compared the results with those

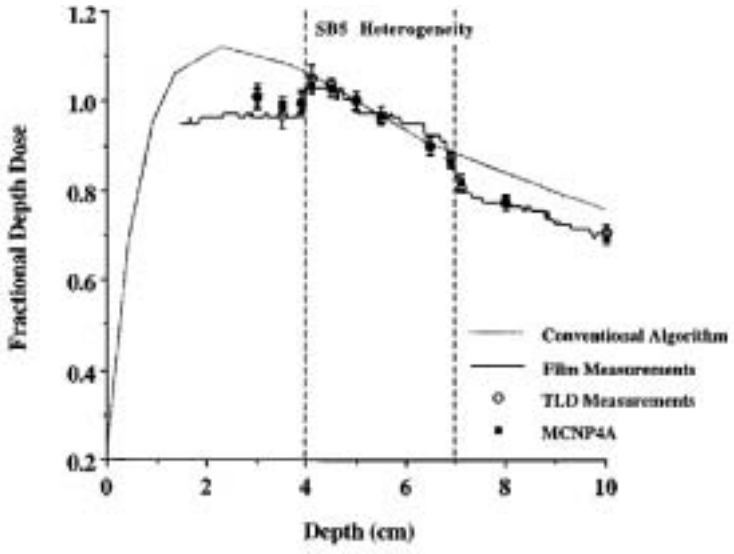

Figure 22. High-density (1.87 g/cm^3) benchmark comparison between TLD measurements, film measurements, and the MCNP4A simulation and conventional treatment planning calculations for a 10 MV photon beam. The field size is 10×10 cm^2 with an SSD of 95.0 cm to the top of the phantom. All data sets are normalized to a depth of 5.0 cm. (Reprinted from J. J. DeMarco, T. D. Solberg, and J. B. Smathers,[247] "A CT-based Monte Carlo simulation tool for dosimetry planning and analysis," *Med. Phys.* 25:1–11 (1998) with permission from the American Association of Physicists in Medicine.)

using the CYLTRAN code.[281] The dose in water very near the interface is elevated by a few percent, indicating increased backscattering from aluminum. The dose in aluminum just downstream from the interface is reduced by approximately 15%.

The simulation by Webb[269] of the dose near a water-aluminum interface was repeated by Mackie[282] for the same phantom configuration using the EGS code. The 10×10 cm^2 beam was approximated by a 10.6-cm-diameter beam, the equivalent circular field.[283] The EGS calculation exhibits a sizable dose from backscattering from the aluminum slab. More significantly, the EGS simulation does not predict a buildup region in the aluminum layer. Instead, the dose falls away rapidly at depths away from the interface. The simulations of both Webb and Mackie agree on an approximately 13% reduction in dose at a sufficient distance away from the interface to establish electron equilibrium. This reduction corresponds to the reduced mass absorption coefficient for aluminum compared with water. The results agree qualitatively with those of Rogers and Bielajew[280].

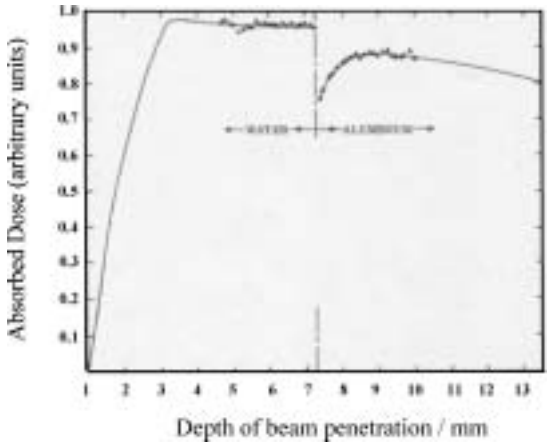

Figure 23. The distribution of absorbed dose for a 10 cm × 10 cm Co-60 beam incident on a water-aluminum interface (Reprinted from S. Webb,[269] "The absorbed dose in the vicinity of an interface between two media irradiated by a ^{60}Co source," *Br. J. Radiol.* 52:962–967 (1979) with permission from *British Journal of Radiology.*)

Recently, Wang et al.[272] used Monte Carlo dose calculation to assess the degree to which tissue inhomogeneities in the head and neck affect static field conformal, computed tomography (CT)-based 6-MV photon treatment plans. The dose distribution was recalculated with the Monte Carlo method, utilizing the same beam geometry and CT images as the clinical treatment planning system. The Monte Carlo method accurately accounted for the perturbation effects of local tissue heterogeneities. Monte–Carlo-calculated treatment plans showed a slightly lower dose received by the 95% of target volume (D95) than the plans calculated with the pencil beam algorithm. The average difference in the target volume encompassed by the prescription isodose line was less than 2.2%. The difference between the dose-volume histograms (DVHs) of the gross target volume (GTV) was generally small. For the brainstem and chiasm, the DVHs of the two plans were similar (see Figures 24 and 25).

Several vendors are currently working toward incorporating a Monte Carlo calculation option in their treatment planning systems with target release dates of mid 2004. NOMOS Corporation already offers a clinical Monte Carlo version based on the PEREGRINE project.[237,254] It is still argued, however, that Monte Carlo may be of more benefit for electron beam planning than for photons. This stance is based on having an alternative photon beam superposition algorithm that can be sufficiently accurate in most clinical situations. For the electron beams the current algorithms continue to rely on weak assumptions in regard to electron scattering and energy and range straggling, and their accuracy can be far inferior as compared to Monte Carlo. For inhomogeneities with

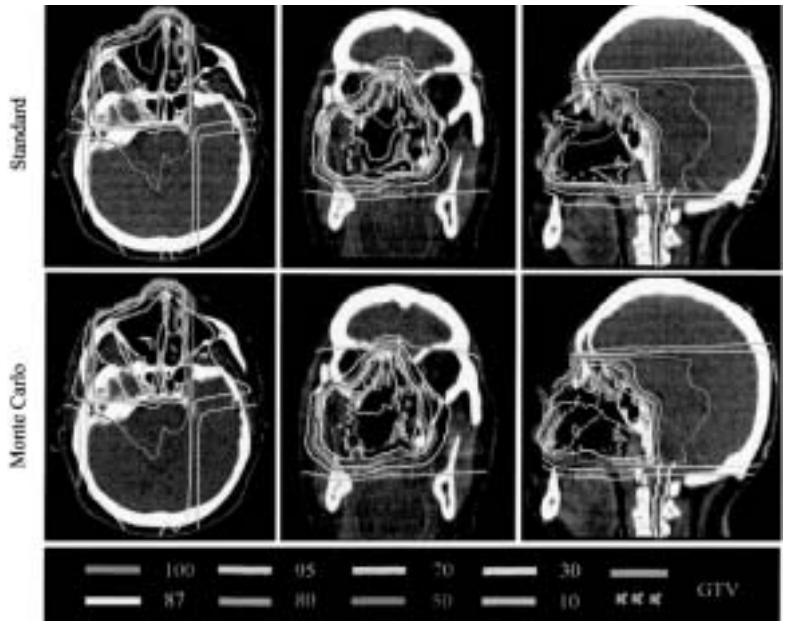

Figure 24. Comparison of the isodose distributions of the three-composite fields from the transverse, coronal, and sagittal views, for a patient with tumor in the para-nasal sinus region. The standard plan based on the equivalent path length method is shown on the upper panel. The Monte Carlo plan is shown on the lower panel. A common feature observed for individual fields is that the Monte Carlo calculated doses to tissue directly behind and within an air cavity are lower. However, after combining the fields employed in each treatment plan, the overall dose distribution shows only small differences between the two methods. (Reprinted from L. Wang, E. Yorke, and C.-S. Chui,[272] "Monte Carlo evaluation of tissue inhomogeneity effects in the treatment of the head and neck," *Int. J. Radiat. Oncol. Biol. Phys.* 50:1339–1349 (2001) with permission from Elsevier Science.)

atomic composition much different from water, as well as for interface dosimetry, Monte Carlo remains the most powerful tool and will play an emerging role in clinical treatment planning.

V. DATA COMPARISON OF DOSE IN INHOMOGENEOUS MEDIA

Various workers have reported measurements made in heterogeneous phantoms. These measurements were made specifically to obtain data to test dose algorithms for cobalt-60 and high-energy x-ray beams. Some workers have

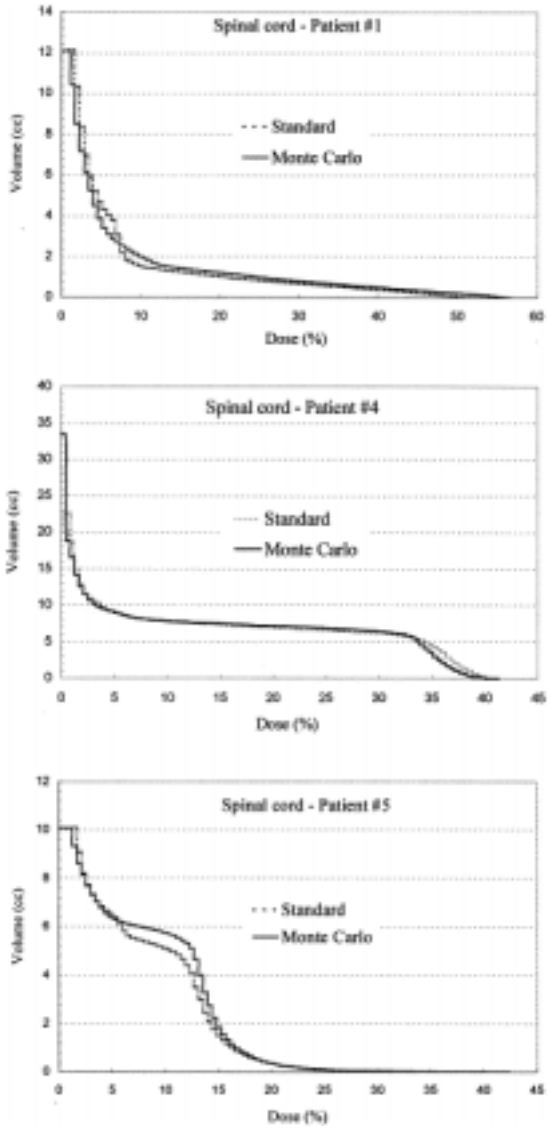

Figure 25. A comparison of the DVH of the spinal cord for three patients. Differences in the details of the DHV and the dose to 1 cc of the structure were observed, with Monte Carlo calculation generally predicting increased dose indices to the spinal cord. However, these changes are not expected to be clinically significant. (Reprinted from L. Wang, E. Yorke, and C.-S. Chui,[272] "Monte Carlo evaluation of tissue inhomogeneity effects in the treatment of the head and neck," *Int. J. Radiat. Oncol. Biol. Phys.* 50:1339–1349 (2001) with permission from Elsevier Science.)

constructed phantoms with different electron densities to simulate simultaneously air cavities, lung and bone;[277,284,285,286,287,288,289] others have focused their interest to a single density:

A. Air Cavities

The most extreme case to quantify effects from heterogeneous media is related to air cavities. The air-tissue interface that gives rise to the skin-sparing effect for high-energy photon radiation is of clinical concern and must be taken into account if the tumor extends to the surface (even though this is depending on contaminant electrons, beam modifiers, etc.). Although dose corrections at large distances beyond a cavity are accountable by attenuation differences, perturbations at air-tissue interfaces are complex to measure or calculate due to lack of electron equilibrium. Underdosing effects occur at both the distal and proximal air cavity interfaces. The magnitude of underdosing depends on cavity size, location, and energy. As the cavity thickness increases, the central axis dose at the distal interface decreases. Increasing field size remedied the underdosing, as did the introduction of lateral walls. Experimental data are therefore required to quantify the magnitude of the dose reduction in the vicinity of air-tissue interfaces.

Measurements around air cavities have been made with a variety of measurement devices for energies ranging from Co-60 to 18 MV. TLDs have been used for the majority of measurements.[291,292,292,293] Thin-windowed parallel-plate chambers have also been utilized.[294,295] Radiochromic film has been recently used for measurements in a clinical phantom.[296,297] Many of these studies provide data sets limited to measurements distal to a rectangular cavity. Others were based on a larynx geometry with measurements reported up and down stream of the cavities.[187,265,293,294,295,296,298,299,300] Many of these studies compared measured data with calculated corrections that did not account for the lack of re-established equilibrium near the cavity. Conventional algorithms commercially available will predict a dose increase well beyond a cavity (beyond d_{max}) based on straight-line calculations (RTAR, Power Law Method) but will not predict the build-down and build-up of dose near interfaces. Even algorithms that explicitly account for electron transport overestimate the dose close to a cavity.[301]

Klein et al.[294] made extensive measurements of doses on surfaces around air cavities. A thin-windowed parallel-plate chamber and a special diode were used for measurements with various air cavity geometries (layer, channel, cubic cavity, triangle) in x-ray beams of 4 and 15 MV. Their results show that following a 2.0 cm wide air channel for a 4 MV, 4×4 cm^2 field there was an 11% underdose at the distal interface, while a 2.0 cm cubic cavity yielded only a 3% loss. Measurements at the proximal interface showed losses of 5% to 8%. For a 4 MV parallel-opposed beam irradiation the losses at the interfaces were 10% for a channel cavity (in comparison with the homogeneous case) and 1% for a cube. The losses were slightly larger for the 15 MV beam (Figure 26).

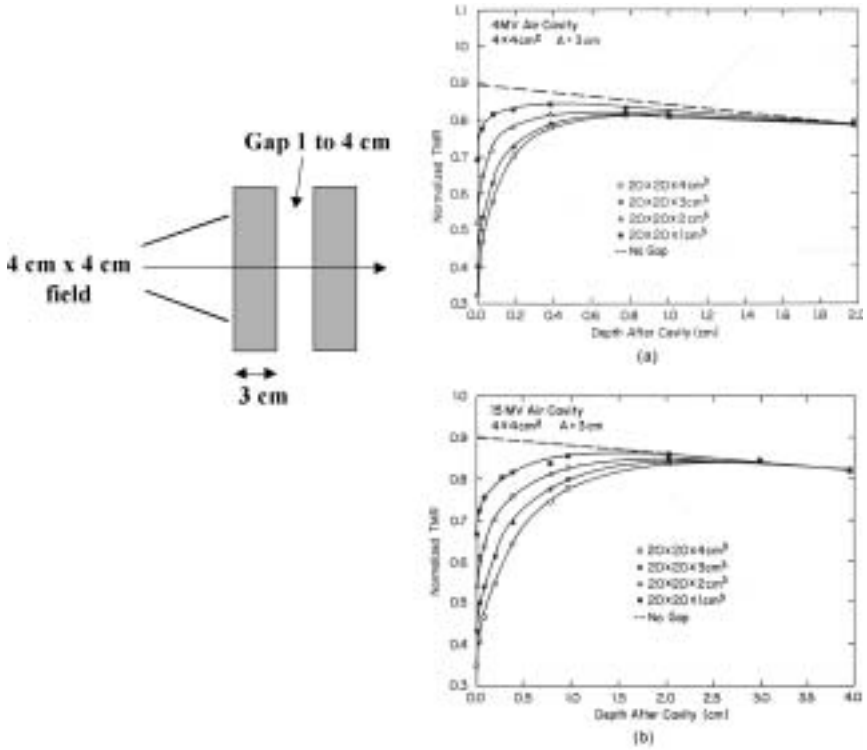

Figure 26. Effects of varying air gap thicknesses on distributions (normalized TMRs) after air for a 4 cm × 4 cm field, (a) 4 MV, (b) 15 MV. (Reprinted from E. E. Klein, L. M. Chin, R. K. Rice, B. J. Mijnheer,[294] "The influence of air cavities on interface doses for photon beams," *Int. J. Radiat. Biol. Phys.* 27:419–427 (1993) with permission from Elsevier Science.)

Underdosage at the lateral interface was 4% and 8% for the 4 MV and 15 MV beams, respectively.

Concerning the dose distribution dependence on energy some reports[294,295,302] suggest better clinical results using lower photon energies with the presence of air cavities and improved target volume coverage when 3D information was used. Izuno et al.[303] reported better local control and survival of early vocal cord cancer treated with Co-60 vs. 8 to 10 MV photons. Coia et al.[302] reported that Co-60 provided better target coverage when compared to 6 MV at the expense of a larger volume of larynx receiving a high dose. The lower energy 4 MV provided better target coverage than 10 MV with only slight increase in the volume of larynx receiving 77 Gy or more. In maxillary sinus treatment with postoperative irradiation Jiang et al.[304] suggest using a water-filled balloon to reduce the air cavity volume (to reduce the potential dose inhomogeneity). For

example, if a pre-cavity thickness for high-energy photons is smaller than the range of secondary electrons, there will be severe underdosage at the distal interface. Also the distance between the proximal and distal layers is proportional to the magnitude of the underdosage that occurs at the distal interface, while underdosage at the proximal interface is fairly consistent. Increase in field size and introduction of lateral interfaces alleviate some of the dose lost to displaced forward scatter by introducing lateral scatter.

B. Lung

Accurate dose calculations in lung are important to assess lung and tumor dose in various radiotherapy cancer patients. Those patients of particular relevance are lung cancer and esophagus cancer patients because large volumes of lung are irradiated to high doses. For treatment of lung cancer, dose heterogeneity corrections and subsequent prescription alteration remain controversial. Energy choice also remains controversial.

Path-length based algorithms: There has been a recent flurry of publications that challenge the simpler dose algorithms in predicting accurate dose within or near lung media. These algorithms are used routinely in manual and computer-aided planning of radiation therapy, but have been validated primarily for cobalt-60 radiation. One deficiency of all the common correction algorithms is that they do not work in regions of electron disequilibrium, such as near lung-tumor interfaces or close to the edges of a beam within lung. This can become significant with high-energy beams (>10 MV) and it is especially important with the increased use of 3D planning and non-coplanar beams, which often involve more treatment fields that most likely traverse greater lung paths.

Many workers clearly have demonstrated the failure of path-length based algorithms (i.e., 1D) in the presence of lung.[167,196,227,275,305,308,309,310,311]

Tests performed with 6 and 15 MV x-rays[275] reveal that incorrect doses can be computed within or near to a low-density medium, particularly when the field size is small. In these cases, electron equilibrium is not achieved in the lateral direction, thereby violating an implicit assumption of all the above calculation methods. Figure 20 from Mackie et al.[276] demonstrates the rebuild-up region downstream from cork for 15 MV x-rays and a 5×5 cm^2 field. A disequilibrium effect, observed for 6 MV x-rays, is much more pronounced with 15 MV x-rays. Within the cork, there is a reduction in dose and all the calculation methods that assume equilibrium overpredict the dose. Considering the average longitudinal range of an electron set in motion 15 MV x-rays to be 3.0 cm in water (i.e., d_{max}), then this range is elongated to approximately 9.0 cm in cork with density of 0.33. Laterally the electrons will be scattered to a distance of approximately of 1/3 to 1/2 of this range, that approximately 3 to 5 cm. Thus, irradiation of cork with a minimum field width equal to twice this lateral range (i.e., 6 to 10 cm) is needed to maximize dose along the central axis of the

beam. The 5×5 cm^2 field is inadequate for achieving such lateral equilibrium in a low-density medium.

Figure 27 from Rice et al.[312] showed the dependence on these new build-up regions of the density of the upstream material. They showed lower interface dose and extended build-up curves beyond the interface. However, in this paper, calculated and measured doses were reported away from the lung, where equilibrium was re-established.

Generally, the dose at the ICRU reference point of any lung tumor is calculated with acceptable accuracy. The accuracy of the algorithms is limited by the assumption of electron and photon equilibrium. The location of the ICRU reference point at the center of a unit density GTV provides almost complete electron and photon equilibrium, hence the relatively small error observed at this position. These circumstances explain the high accuracy with which the dose could be calculated even with simple algorithms (pencil beam algorithm with 1D corrections, the modified Batho algorithm, and the equivalent path length algorithm, see Engelsman et al.[196]) at the ICRU reference point. Differences between calculated and measured dose distributions are primarily due to changes in electron transport in the lung, which are not adequately taken into account by the simple tissue inhomogeneity correction algorithms. Particularly for high photon beam energies, clinically unacceptable errors will be intro-

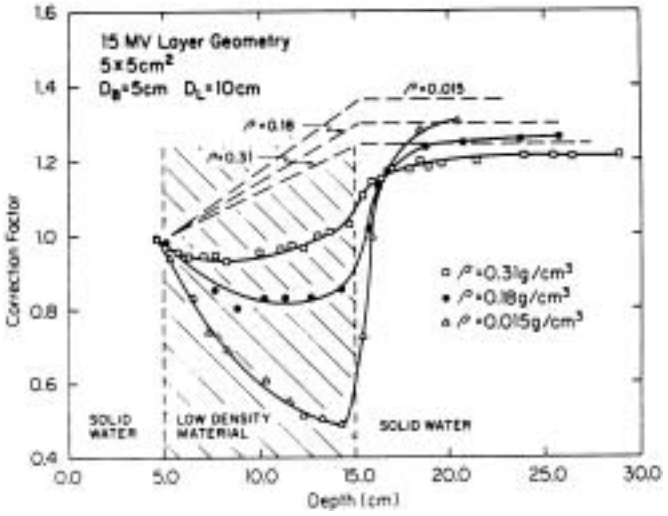

Figure 27. Correction factor for a 15 MV x-rays, 5×5 cm^2 field as a function of depth below the surface of the phantom for densities of 0.015 (humid air) and 0.18 and 0.31 (lung) gcm^{-3}. (Reprinted from R. K. Rice, B. J. Mijnheer, L. M. Chin,[306] "Benchmark measurements for lung dose corrections for x-ray beams," *Int. J. Radiat. Oncol. Biol. Phys.* 15:399–409 (1988) with permission from Elsevier Science.)

duced in the choice of field sizes employed for conformal treatments, leading to underdosage of the planning target volume (PTV). In addition, the dose to the lung will be wrongly predicted which may influence the choice of the prescribed dose level in dose-escalation studies: many papers have demonstrated that simplistic algorithms can overestimate the dose at a tumor lung boundary to such a degree that making 1D corrections may be misleading clinically and contra-indicated.[24,190,212,313]

3D dose calculation: Papers that examined the spread of secondary electrons from high-energy beams[32,33,35,94,314,315,316] showed that the concept of primary and scatter could be extended to conditions of non-equilibrium, using small field TAR values which reflect the loss of lateral electron equilibrium.

Choice of energy: Many lung patients who undergo radiation therapy are treated with higher energy photons (15 to 18 MV) to obtain deeper penetration. However, the longer range of the higher energy recoil electrons in the low-density medium may cause lateral electron disequilibrium and degrade the target coverage. Several studies (e.g., refs. 33, 35, 37, 227, 315, 317, 318) quantified the effects of lateral low-density regions and show that the use of low-energy beams is preferred in irradiating lung tumors because higher energy beams would need larger field margins in order to achieve target dose homogeneity. The previous work by Mackie et al.[275] further showed the central axis dose depression for 15 MV x-rays (Figure 20). Wong and Purdy[146] provided similar measurements for Co-60, demonstrating the dependence on the proximity of low-density regions to points of interest (see Figure 28). Loss of electron equilibrium within and adjacent to low density materials can result in a dose reduction along the central axis and near the beam edge for megavoltage photon beams. In this context, the Radiation Therapy Oncology Group[319] protocol #91-05 recommends the use of photon beams of energy 12 MV or less for non-small-cell lung cancer therapy.

Ekstrand and Barnes[33] have compared profiles of x-ray beams ranging in energy from 4 to 18 MV. The profiles were measured at 10-cm depth in unit-density and lung-density (0.26) phantoms. At the highest energy the 20% to 80% physical penumbra width was measured to be 7.5 mm in the unit-density material, whereas in the lung phantom the width was 18 mm. At 4 MV the situation was reversed; that is, the penumbra was slightly smaller in the lung phantom. As a result, unanticipated underdosing inside the field and greater dose outside the field can occur when high-energy x-rays are used. The authors suggested that the optimal beam energies for lung tissue were 6 MV or less.

The penumbra broadening of a photon beam in lung is of major concern for conformal irradiation of lung tumors. This broadening necessitates larger field sizes to achieve the same target coverage as in a homogeneous environment, and the effect increases for higher energies. For treatment of lung tumors, it is advantageous to keep the field sizes as small as possible, to limit the mean lung dose. It is, therefore, concluded[32,317] that beam energies above about 10 MV are less appropriate for treatment of these tumors.

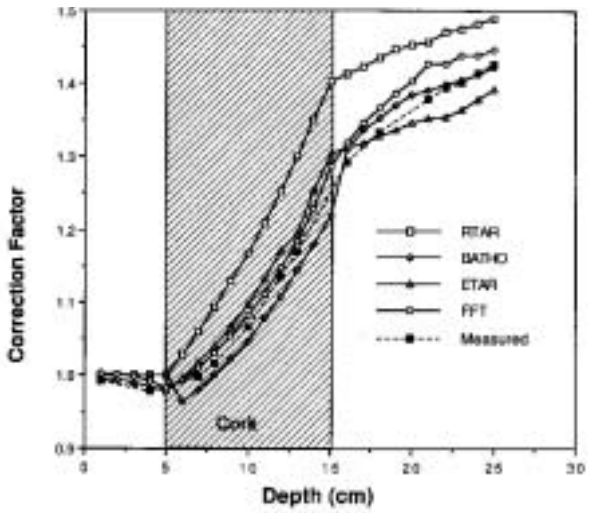

Figure 28. Measurements demonstrate the dependence on the proximity of low-density regions to points of interest for Co-60 (Reprinted from J. W. Wong and J. A. Purdy,[146] "On methods of inhomogeneity corrections for photon transport," [Review]. *Med. Phys*. 17:807–814 (1990) with permission of the American Association of Physicists in Medicine.)

Klein et al.[313] performed a study that compared dose distributions around a tumor situated within the lung parenchyma for 6 and 18 MV beams using a five-field irradiation technique in an anthropomorphic phantom. They concluded that, for tumors surrounded by lung tissue, lower energy beams should be used and, for tumors with at least one boundary with the lung parenchyma, boost fields should be treated with lower energy beams. Their conclusions are supported also by Miller et al.[317] and Kornelsen and Young.[35]

White et al.[315] examined unopposed and parallel opposed beams in lung density phantoms, and concluded that the addition of an opposed beam reduced the penumbra difference between 6 and 18 MV to such a sufficient extent that the use of higher energy beams would be preferable in some clinical situations in which patient thickness would lead to unacceptably high entry doses with lower energies. However, the reduced entrance dose with higher energies has to be balanced against the increased field margins, which result in a possible increase in mean lung dose and therefore an increased complication probability. They concluded also that for opposed fields, the difference in beam fringe values (distance between the 50% and 90% isodose lines) degradation of the 6 and 18 MV photon beams at the lung/polystyrene interface is clinically insignificant compared to daily setup errors and patient motion.

Brugmans et al.[32] have used an inhomogeneous phantom, consisting of polystyrene, cork, and polystyrene layers, with a $6 \times 6 \times 6$ cm^3 polystyrene cube

inside the cork representing the tumor, to simulate a lung cancer treatment. Film dosimetry experiments were performed for an AP-PA irradiation technique with 8 or 18 MV beams. They concluded that for lung cancer treatment, a beam energy of 8 MV is more suitable than 18 MV. Field sizes in conformal radiotherapy of tumors in lung can be decreased without compromising the biologically effective dose to the target. Reductions of the mean lung dose by at least a factor of 1.6 are feasible for the same mean target dose. A simple intensity-modulation technique, in which small edge segments deliver some extra dose at the target edge in addition to a small uniform segment, can be employed to maintain the target dose homogeneity and limit the decrease in minimum target dose upon field shrinkage. Small movements of the target, where the tumor in which the edge of the target volume does not approach the field edge to within several millimeters, hardly affects the target dose and no extra margin for target motion needs to be taken into account. For motion with larger excursions, however, application of an extra margin is essential. Their study has demonstrated that conformal therapy of lung tumors can be significantly improved; the mean lung dose can be decreased by decreasing the field size and keeping the mean target dose constant. For clinical application of these findings for the conformal treatment of lung tumors, however, it is recommended by the authors that dose distributions in the presence of heterogeneities can be calculated with a higher accuracy than presently possible with most treatment planning systems. Since Brugmans' work is quite complex and includes much valuable information, this Task Group recommends its study.

Obviously, an accurate dose computation algorithm (such as a Category 4 type as decribed earlier) will guide the treatment planner in the selection of the correct energy and field margins. Some instances may occur where selection of a higher energy beam would result in superior dose distributions, provided the correct margin is selected. When inaccurate dose calculation algorithms are used, use of lower energy beams for lung is preferred since the dose calculation inaccuracy is less for many algorithms.

Dosimetry studies based on slab geometry with single-beam geometry do not represent the clinical situation. A circumscribed tumor within lung poses a more complex problem. Before adjusting dose prescriptions based on heterogeneity corrections, realistic phantom studies have to be performed. The accuracy and effect of the corrections must then be assessed. Various authors[320,321] have constructed and irradiated phantoms based on benchmark patients. The data were used to analyze algorithms (2D or 3D) and provide information concerning energy choice for lung irradiation. The debate on the use of simple (1D) and complex (3D with electron transport) inhomogeneity corrections or using no correction at all continues, especially as dose escalation trials with 3D–Treatment Planning evolve.[30]

Breast Treatment: Due to the inclusion of lung tissue in the treatment volume, some parts of the breast will get a higher dose during tangential breast irradiation because of the lower lung density. The influence of lung on breast

treatment planning, the effect of different inhomogeneity algorithms on the dose distributions, and the need of 3D dose calculation and conformal techniques have been comprehensively addressed by some authors.[184,322,323,324,325,326,327,328] To investigate this issue, Chin et al.[184] have studied the three-dimensional dose distributions calculated for an "average" (lung density 0.31 g/cm^3) breast phantom for ^{60}Co, 4 MV, 6 MV, and 8 MV photon beams. They have concluded that when lung correction is included in the dose calculation, the doses to areas at the left and right margin of the lung volume increase. The magnitude of the increase depends on energy and the patient anatomy. For the "average" breast phantom the correction factors are between 1.03 and 1.06 depending on the energy used. Higher energy is associated with lower correction factors. Both the ratio-of-TMR and the Batho lung correction methods, used in this study, can predict these corrections within a few percent. The use of higher energy photons provides lower value of the "hot spots" compared to lower energy photons, but this needs to be balanced against a possible disadvantage in decreased dose delivered to the skin and superficial portion of the breast. Aref et al.[323] in a study of the radiation therapy plans of 85 patients with early breast cancer have found a significant reduction of volume overdosage if a complex 3D plan utilizing multiple contours, lung inhomogeneity correction, and dose-based compensators is used compared to single-contour-based methods. Fogliata et al.[324] have analyzed different treatment techniques with conventional photon beams, intensity-modulated photon beams, and proton beams for intact breast irradiation for patients in whom conventional irradiation could cause potentially dangerous lung irradiation. They concluded that geometrically difficult breast cancer patients could be irradiated with a three-field non-IMRT technique, thus reducing the dose to the lung that is proposed as standard for this category of patients. Intensity-modulated techniques were only marginally more successful than the corresponding non-IMRT treatments, while protons offer excellent results.

Data on the accuracy of dose calculation algorithms, investigated by phantom measurements, determinations of the geometry and density of the actual lung in the patient, and the results of *in vivo* dose measurements, have been published by Mijnheer et al.[328] From their work it can be concluded that a lung correction varying between 3% and 7% is needed, but its magnitude is slightly overpredicted in a number of commercial treatment planning systems. Because this increase in dose is already in a high-dose region, the authors recommend that inhomogeneity corrections should be applied during tangential breast irradiation.

Accuracy in patient positioning is a prerequisite to ensure agreement between the calculated and the delivered dose distribution to the patient but may well be one of the weakest parts of the radiotherapy process.[329,330,331,332] During the delivery of the prescribed dose in external beam radiotherapy, respiration alters the patient's body outline and consequently the basis for dose calculations. Variations in dose distribution and in dose delivery can contribute

to underdosage of the tumor or overdosage of normal tissue, which are potentially related to a reduction of local tumor control and an increase of side effects. Breathing motion can produce deviation of the delivered dose distribution compared to the calculated CT-based treatment plan and the effect in the dose-volume histograms can be significant.[333,334,335,336] Breathing also affects the density of the lung, thus affecting the calculated dose.[337,338] An estimation of the impact that setup uncertainties have on the clinical outcome of the treatment (in terms of lung tumor control and lung complications) has recently been reported based on radiobiological modeling.[196,339,340]

C. Bone and High-Density Media

There is a surprisingly small number of papers addressing influence of the presence of bone.[247,341,342,343,344,345,346] There are many studies however that address the influence of high Z media.[56,74,75,91,217,256,263,264,269,347,348,349,350,351,352,353,354] Figure 29 demonstrates the dose build-up region as a photon beam approaches a steel slab inhomogeneity in water. Downstream from the interface a build-down followed by a build-up is observed due to the lack, initially, and then the rebuild of the electron fluence (Galbraith in Gullane).[85] These papers are explicit demonstra-

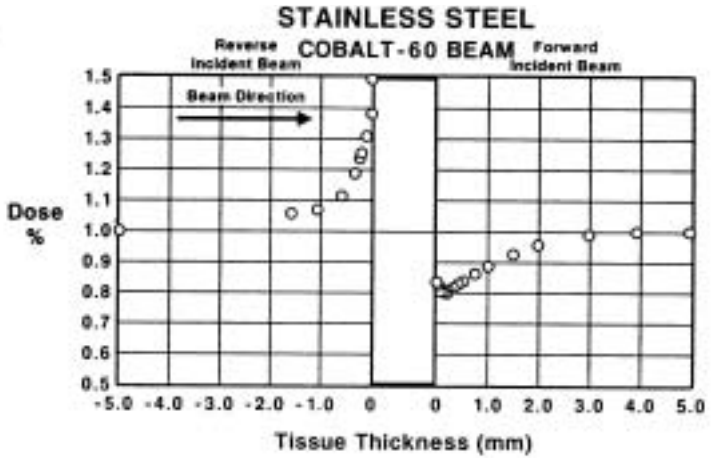

Figure 29. Upstream build-up region and downstream build-down followed by build-up regions in water near to stainless steel for parallel opposed beams. Doses at interfaces are measured using a wall-less ionization chamber, thus yielding doses at the interface surface. The interface doses increase by as much as 50% at the proximal surface of the metallic inhomogeneity (Reprinted from P. J. Gullane,[85] "Primary mandibular reconstruction: analysis of 64 cases and evaluation of interface radiation dosimetry on bridging plates," *Laryngoscope* 101:1–24 (1991) with permission of Lippincott Williams & Wilkins.)

tions of the competition of abundant downstream scatter and the "rebuild up" of dose in the low Z medium downstream. A few studies exist that examine the influence of implanted high-Z prosthetic materials.[93,355,356,357,358] Wang et al.[359] and Mian et al.360) examine the dose enhancement at bone-implant interfaces from scattered radiation during simulated head and neck radiotherapy.

Niroomand-Rad et al.[357] have investigated the magnitude of dose perturbation effects at the tissue-titanium alloy implant with (100 μ and 500 μ thick) and without hydroxylapatite (HA) coating interfaces in head and neck cancer patients treated with 6 MV and 10 MV photon beams. They found at the upper surface (toward the source) of the tissue-dental implant interface, for 15×3.2 mm^2 uncoated, as well as 100 μ coated discs, dose perturbation is about +22.5% and +20.0% using 6 MV and 10 MV photon beams, respectively. At the lower interface for 15×3.2 mm^2 and 48×3.2 mm^2 uncoated and 100 μ coated discs, dose reduction is similar and is about −13.5% and −9.5% for 6 MV and 10 MV beams, respectively. For 48×3.2 mm^2 discs, these values basically remain the same. These results were slightly lower for the 500 μ coated discs but are not clinically significant.

Some studies exist dealing with the biological or clinical consequences of interface effects. Metal dental prostheses or overlays may lead to increased mucosal reactions of adjacent tissue surfaces during intensive irradiation of the oral cavity. The dosimetry of this phenomenon was investigated by Gibbs et al.[361] by irradiating dental phantoms with 4 and 6 MV photons. It was found that gold and amalgam interfaces may produce local mucosal doses as high as 150% to 170% depending on the beam geometry, but doses of 111% to 126% for gold crowns and about 109% to 118% for amalgam fillings were found for opposed-beam configurations. Two to four mm of tissue-equivalent absorber is sufficient to re-establish a homogeneous dose distribution and should be employed throughout therapy whenever dental extraction is unwarranted. Zellmer et al.[362] examined cell cultures attached to 6 micron Mylar™ adjacent to scattering materials consisting of polystyrene, glass, aluminum, copper, tin, and lead and irradiated with 137Cs gamma rays and 200 kVp x-rays. According to the authors, the major differences in biological effect observed when the cells were irradiated adjacent to these materials could be largely explained by the differences in the physical dose. Further analyses using the linear quadratic (LQ) equation suggested additional biological effects with implications for the mechanisms involved. Cells showed a small but consistent increase in the low-dose mechanism for radiation scattered from high-Z material. An increased value of the alpha coefficient suggests an increase in relative biological effectiveness (RBE) which could be associated with a higher proportion of low-energy and track-end electrons in these fields.

AAPM TG 6[348] has performed an in-depth review of the issues associated with implanted high-Z hip prostheses and has made recommendations on how to deal with some of the practical issues in clinical practice.

D. Influence of CT Number Variations

Accurate dose calculation not only requires an accurate algorithm but also relies on accurate calibration of Hounsfield Unit (HU) for CT-based inhomogeneity corrections (especially for lung cases), prior to dose calculation. In CT scans, the parameter that mostly affects the accuracy of CT-HU is kV because it determines the beam quality and, therefore, the attenuation coefficient or HU. Other parameters such as mAs, slice thickness, pitch factor, etc., should, in principle, take no effect. For each CT scanner, the HU for each kV should be correctly calibrated.

The limitation of using CT numbers for *in vivo* tissue characterization is well documented (e.g.,[363,364,365,366,367,368,369,370]) Newman et al.[363] suggest that the CT number and thickness of bone cannot be measured accurately unless the thickness exceeds 3 mm. Below this thickness there is a progressive underestimation of the CT number and an overestimation of thickness. These CT number variations, however, did not result in significant dose-calculation errors during radiation therapy treatment planning. Geise and McCullough[364] reported that a 4% to 10% uncertainty in electron density would result in no more than a 2% change in dose; therefore, they concluded that knowing the size and shape of a significant heterogeneity is more important than the accuracy of knowing the electron density.

Chu et al.[366] demonstrated that the uncertainty of the CT numbers from a simulator-based CT scanner is larger than that from a conventional CT unit. This phenomenon is more obvious for higher electron density or high-Z materials; in their study, a 20 HU uncertainty in CT number for soft tissues results in about 2% of uncertainty in electron densities, and a 250 HU-CT number uncertainty for cortical bone results in about 5% of uncertainty in electron densities. Also, the dose uncertainty for the 6 MV beam is less than 2%, up to a 20 cm depth. The presence of 1 cm bone increases the uncertainty by less than 0.5%. The dose uncertainty for the 18 MV beam is less than 2%, up to at least 30 cm in depth. Verellen et al.[365] also compared the treatment monitor units (MU) calculations for 10 pelvic fields using images from simulator-based CT and diagnostic CT. The agreement between their equivalent path length (EPL)-based MU calculations is within 1% to 2%. The effect of CT numbers on dose calculation may depend on the particular dose algorithm used. Chu et al., have performed additional dose calculations using the collapsed cone convolution algorithm[106] implemented in a commercial planning system (Pinnacle, ADAC Labs, Milpitas, CA) to confirm the EPL results described above. MUs for the treatment fields were calculated for three clinical cases: the brain, lung, and pelvis. The calculations show that a change of 20 HU for soft tissue and 250 HU for bone result in a less than 1% change in MU for the brain case, and a less than 2% change for the lung and pelvis cases.

Establishing a relationship between CT numbers and electron densities provides a simple method in dose calculations in inhomogeneous tissues. The

possible errors in measured CT numbers need to be assessed in order to estimate the error of calculated dose when the CT information is directly used. Chu et al.[366] have measured the CT number and have also conducted a series of experiments to obtain the possible errors in measured CT numbers as a function of electron density. These errors, although larger than those from diagnostic CT scanners, produced an error in dose of less than 2% with depths up to 20 cm.

For high-energy beams such as the 18 MV, pair production accounts for more than 20% of the total energy transfer in bone. The pair production component is proportional to Z per gram and not to electron density (ED). However, if there are high-Z materials on the beam path (e.g., 60° external wedge or an internal hip replacement material) which cause significant amounts of beam hardening and pair production for high energy beams such as 18 MV, the algorithm's accuracy may need to be reevaluated. These high-Z materials will also introduce high dosimetric differences between CT scans using different kVs (or different HU–ED curves) because the photoelectric effect is strongly energy and Z dependent. The difference is caused not only by the materials themselves, but also by the possible streak artifacts generated by the materials.

Task Groups 40[371] and 53[384] also make specific recommendations on tests and measurements to be made.

E. Radiosurgical Beams

For fractionated stereotactic radiotherapy (SRT) and/or stereotactic radiosurgery (SRS) treatment planning, the volume enclosed by the external contour is typically assumed to be of uniform density. The majority of the SRT/SRS treatment planning systems ignore the presence of heterogeneities such as the cranial bone and the air cavities at the skull base mainly due to two reasons: (a) the assumption that heterogeneity correction is not necessary since the multiple beam arrangement is compensating the perturbation effect of the cranial bone and (b) computation time limitations since the irradiation technique includes multiple arcs and multiple isocenters. However, it has been shown by Rustgi et al.[372] for 6 MV x-rays that air cavities and low-density inhomogeneities encountered in the nasopharyngeal and sinus regions cause a significant perturbation in the dose distribution of small beam immediately beyond the inhomogeneity. They used a diamond detector in a 6 MV photon beam. Measurements that were made in a uniform density solid-water phantom and in the presence of four air gaps indicate significant dose perturbation immediately beyond the air-solid water interface; e.g., the reduction in dose at the surface for a 12.5 mm diameter field was 11%, 17%, 23%, and 33% for air gap thickness of 3, 4.6, 6, and 9.2 mm, respectively. For the dose perturbation caused by high-density inhomogeneities, i.e., cranial bone, Rustgi et al.[373] have shown that neglecting the presence of the cranial bone may result to an overestimation of the absolute dose at the isocenter by approximately 2% to 5% (depending on the cranial

bone thickness which varies between 3 and 8 mm with average thickness of 5 mm). The same magnitude of perturbations have been obtained by Theodorou et al.[374] comparing the results of Monte Carlo simulation and stereotactic dose calculation code (without heterogeneity correction) based on clinical cases. The effect of air inhomogeneities on dose distributions in radiosurgery is expected to increase with beam energy as demonstrated by the results of Solberg et al.[375] who studied a 10 MV photon beam. Nevertheless, for targets situated in the central part of the brain Ayyangar and Jiang,[376] based on clinical cases, showed that conventional algorithms without inhomogeneity correction are sufficiently accurate for relative dose distributions; whereas the absolute dose is overestimated by 1.5% to 2.6% compared to Monte Carlo calculations.

F. Multiple Beam Arrangements

Choice of beam quality in the presence of inhomogeneities could be less critical when multiple beams are used as several investigators[39,196,272,302,377] have shown based on clinical measurements and image based treatment plans.

Engelsman et al.[196] have shown that even when using low-energy beams for irradiating lung tumors, the underestimation of field margins may result in a very large difference between planned and actual delivered dose distribution. Single multileaf collimator-shaped photon beams of 6, 8, 15, and 18 MV nominal energy were used to irradiate a 50-mm diameter spherical solid tumor, simulated by polystyrene, which was located centrally inside lung tissue, simulated by cork. The planned dose distribution was made conformal to the PTV, which was a 15 mm 3D expansion of the tumor. Values of both the absolute dose at the ICRU reference point and relative dose distributions inside the PTV and in the lung were calculated using three inhomogeneity correction algorithms. The algorithms investigated in their study were the pencil beam algorithm with 1D corrections, the modified Batho algorithm, and the equivalent path length algorithm. Deviations of up to 3.5% between calculated and measured values of the dose at the ICRU reference point were found. Discrepancies between measured and calculated beam fringe values (distance between the 50% and 90% isodose lines) of up to 14 mm have been observed. The differences in beam fringe and penumbra width (20±80%) increase with increasing beam energy. Their results have demonstrated that an underdosage of the PTV up to 20% may occur if calculated dose values are used for treatment planning. The three algorithms predict a considerably higher dose in the lung, both along the central beam axis and in the lateral direction, compared with the actual delivered dose values. They have also concluded that the difference between planned and actual position of the 95% isodose level will be smaller in a treatment plan if multiple (non-opposing) beams are used, because the contribution of a specific beam penumbra to the dose at a certain point is decreased.

Wang et al.[272] retrospectively studied 3D conformally shaped 6 MV photon treatment plans that had been used for the treatment of five patients with tumors

in the nasopharyngeal or paranasal sinus regions. The plans were designed with a clinical treatment planning system that uses a measurement-based pencil beam dose-calculation algorithm with an equivalent path-length inhomogeneity correction.[378,379] For each plan, the dose distribution was recalculated with the Monte Carlo method, which accounts for the perturbation effects of local tissue heterogeneities.[255,268,380] However, after combining the fields employed in each treatment plan, the overall dose distribution shows only small differences between the two methods. Their results indicate that conformal 6 MV photon treatment plans for head-and-neck tumors, designed with a pathlength corrected, measurement-based pencil beam algorithm, give adequate target coverage and sparing of normal organs at risk, even in the presence of large surgical air cavities.

G. Measured Benchmark Data

The data from the work by Rice et al.[306] and by Zhu[218] are assimilated in Tables 10 through 12 to give a set of measurements covering the energy range from cobalt-60 to 18 MV x-rays for lung and bone.

The phantom geometries in the examples given here are simple. They consist of slabs of heterogeneous regions whose boundaries are normal or parallel to the axis of the radiation beam, and which comply nicely with the assumptions underlying the simpler dose algorithms. Although data are available for other geometries, data for only two geometries are tabulated here.

One geometry consists of a slab extending across the entire field and the other geometry consists of two lateral blocks separated by a region of unit density material around the central axis to simulate the mediastinum.[181] The slabs were imbedded in water-equivalent plastic or suspended in water at a depth of DB from the surface. The slab thickness was denoted by ST. For the split slab geometry, the separation between the regions was denoted by S.

All the data given in Tables 10 through 12 are Inhomogeneity Correction Factors (ICF) measured on the central axis of the beam for square fields. Since measurements are not easily obtained within a living human, the measurements have been more practically made in a variety of phantom materials. For the homogeneous medium, water is the usual material of choice. However, water-equivalent plastic has also been used. Rice used balsa wood with a density of 0.18 g/cc to represent emphazeimic lung and Styrofoam™ with a density of 0.015 g/cc to represent humid air. Rice et al.[306] fabricated plastic lung phantoms using Constantinou's formulation.[381,382] Many others[384] have used cork to represent normal lung densities (0.25 to 0.4 g/cm^3). Both lung and bone phantom material provided commercially by Gammex RMI (Middleton, WI) were used by Zhu et al. Zhu et al.[212] measured the density of the lung plastic to be 0.272 g/cc and the density of the bone plastic to be 1.83 g/cc. The composition by weight of the lung material was C (0.6887), O (0.1762), H (0.0862),

Ca (0.0252), N (0.0226), Cl (0.0011) and that of the bone material was O (0.3757), C (0.3226), Ca (0.2703), H (0.031), N (0.0099), and Cl (0.0005).

According to the suggestions of AAPM TG 53[384] the tests must be based on the nature of the correction method used. For example, if the algorithm uses a simple equivalent pathlength approach, the verification of the algorithm can be performed with a very simple 1D phantom test, but it will fail for more complex phantoms. More complicated algorithms will require more complicated "stress" tests.

The measurements made by Rice et al.[306] employed special parallel plate chambers constructed from water-equivalent plastic and lung-equivalent plastic. The plate separation of the parallel plate chambers was 2 mm. In addition, Rice used a cylindrical 0.1 cc ionization chamber with an inner diameter of 3.5 mm. These data are generally limited to measurements along the central axis of the beam only, with several different geometries and two different beam qualities (4 and 15 MV). Further benchmark data especially 2D and 3D data for various geometries are needed.[385]

Zhu and Boyer[218] made measurements in water with a 0.6 cc ionization chamber with an inner diameter of 6.25 mm. Measurements in plastic were made with a 0.1 cc chamber and with TLD. In addition, Zhu made measurements in the unit density side of interfaces in solid water (Gammex RMI) with a 0.33 cc parallel plate chamber.

The ionization measurements made by Zhu were corrected for the presence of the ionization chamber using factors calculated as follows:[167]

$$ICF_{bone} = ICF_{meas,\,bone} \frac{\left(\frac{L}{\rho}\right)_{gas}^{bone}}{\left(\frac{L}{\rho}\right)_{gas}^{water}} \frac{P_{reple,bone} P_{wall,bone}}{P_{repl,water} P_{wall,water}} \tag{37}$$

$$ICF_{lung} = ICF_{meas,lung} \frac{\left(\frac{L}{\rho}\right)_{gas}^{lung}}{\left(\frac{L}{\rho}\right)_{gas}^{water}} \frac{P_{repl,lung} P_{wall,lung}}{P_{repl,water} P_{wall,water}} \tag{38}$$

The physical factors in equations (37) and (38) are defined and explained in TG 21.[385]

For the lung measurements, the corrections to the ionization measurements were not significantly different from unity (see also measurements from Mauceri and Kase[386]). For bone the factors were more significant, i.e., 0.928 for 6 MV and 0.925 for 18 MV. Thus "raw" ionization readings should not be used directly for bone dosimetry with ion chambers.

All measurements reported in Tables 10 through 12 were made with a fixed source-to-surface distance (SSD). For cobalt-60 and 4 MV x-rays the SSD was

80 cm. For x-ray energies from 6 MV to 18 MV, the SSD was 100 cm. These type of data are preferred for checking computer calculations since it allows the comparison of several depths from one field size calculation, and since it checks the computer modeling of intensity variation with distance from the source.

The machines used in studies in the tables are listed in Table 9.

A sample of correction factors for uniform slabs of lung and bone are given in Tables 10, 11, and 12. Highlights of the tables are plotted in Figures 30 through 33. The lower panels in Figures 31 and 33 show lung slabs at 6 MV and 15 MV x-rays, respectively. At both energies there is a rise in primary (TERMA) transmission through the lung slab. At 6 MV ICFs decrease with increasing field size. At 15 MV, there is little difference between 10 cm $\times$ 10 cm and 20 cm $\times$ 20 cm field sizes. However, the ICF for a 5 cm $\times$ 5 cm field is less than unity in the lung due to lateral equilibrium effects (see previous Figure 20). It is apparent from examining Table 10 that the correction factor in lung decreases with increasing energy. This characteristic is demonstrated more clearly in Figure 34 in which data from Takeshi for a 10 cm $\times$ 10 cm field is plotted for lung heterogeneity for a range of energies between cobalt-60 and 15 MV. Beyond the lung slab the ICF is greater than unity due to the higher primary transmission through the slab.

Typical ICFs for bone are shown in the upper panels of Figures 31 and 33 at 6 MV and 18 MV x-rays, respectively. For 6 MV x-rays, there is a build-up, build-down, and rebuild-up effect. When the energy is increased to 18 MV, there is a build-down effect beyond the interface. Beyond the bone slab ICFs are less than unity.

Data in split slab phantoms are tabulated in Tables 11 and 12. Highlights of the tables are plotted in Figure 32. The lower panel of Figure 32 shows ICFs measured around a lung heterogeneity. The effect on the ICF is a decrease in dose due to a loss of photon scatter in the surrounding lung material. The effect decreases with increasing energy because the scattering is more forward-peaked with increasing energy. The upper panel depicts ICFs measured in the presence of bone slabs. Here, the ICFs rise because of greater scattering in the high-density bone. The effect decreases and becomes foreshortened because of

Table 9. The machines used in studies
(refer to the data given in Tables 10–12).

Stated Energy	Model	Manufacturer
Cobalt 60	Theratron 780C	Atomic Energy of Canada, Ltd. (now MDS Nordion)
4 MV	Clinac 4	Varian Radiation Division
6 MV	Mevatron KD	Siemens Medical Laboratories
15 MV	Mevatron 77	Siemens Medical Laboratories
18 MV	Mevatron KD	Siemens Medical Laboratories

Table 10. "Inhomogeneity Correction Factors" for heterogeneities composed of lung-equivalent plastic.

Lung Slab

	Cobalt-60		**4 MV**			**6 MV**		**15 MV**			**18 MV**	
	10 × 10	20 × 20	5 × 5	10 × 10	20 × 20	10 × 10	20 × 20	5 × 5	10 × 10	20 × 20	10 × 10	20 × 20
DB	3 cm		2 cm			3 cm		5 cm			3 cm	
ST	5 cm		10 cm			5 cm		10 cm			5 cm	
2.0			* * Interface * *									
2.1			0.999	0.982	0.982							
2.3			0.995	0.985	0.980							
2.5				0.984	0.988							
2.7			0.996	0.982	0.976							
3.0	* * Interface * *					* * Interface * *					* * Interface * *	
3.3			1.011	0.982	0.982							
3.5				0.986	0.987							
4.0	0.969	0.983				0.990	0.980				0.948	0.996
4.1			1.031	1.009	0.992							
4.6						1.007	1.006	0.989	0.990	0.993		
5.0	0.975	1.001						* * Interface * *			0.994	1.007
5.1								0.968	0.982	0.976		
5.7								0.953	0.985	0.982		
6.0	1.020	1.030				1.035	1.029				1.006	1.019
6.1			1.093	1.050	1.023							
6.3								0.942	0.996	0.997		
7.0	1.041	1.034	1.099	1.069	1.048	1.060	1.047				1.028	1.028
7.1								0.942	1.006	1.007		
7.7								0.944	1.009	1.012		
8.0	* * Interface * *					* * Interface * *					* * Interface * *	
8.1			1.147		1.069							

(continues)

Table 10. Continued.

	Cobalt-60		4 MV			6 MV		15 MV			18 MV	
	10 × 10	20 × 20	5 × 5	10 × 10	20 × 20	10 × 10	20 × 20	5 × 5	10 × 10	20 × 20	10 × 10	20 × 20
8.2						1.083	1.072					
8.3	1.124	1.115	1.160	1.125	1.098			0.930	1.017	1.022	1.060	1.054
8.4						1.085	1.076					
9.0						1.097	1.082					
10.0	1.139	1.124				1.104	1.087	0.952	1.043	1.047	1.065	1.057
10.1			1.202	1.144	1.141							
10.5			1.224	1.168	1.134							
11.0	1.149	1.131	1.124	1.182	1.147	1.110	1.091				1.068	1.059
11.1								0.959	1.050	1.055		
11.3			1.255	1.188	1.154							
11.5			1.257	1.197	1.161							
11.7				1.192	1.154			0.969	1.065	1.072		
12.0	1.159	1.138	* * * Interface * * *			1.114	1.096				1.071	1.063
12.3								0.964	1.074	1.080		
12.4			1.315	1.243	1.198							
12.9			1.332	1.257	1.210							
13.0	1.168	1.144				1.119	1.100				1.073	1.064
13.1								0.996	1.089	1.091		
13.4			1.344	1.266	1.221							
13.7								1.009	1.102	1.104		
13.9			1.356	1.280	1.233							
14.0	1.175	1.147				1.123	1.102				1.075	1.064
14.7								1.029	1.121	1.119		
15.0	1.180	1.152				1.126	1.104	* * * Interface * * *			1.077	1.066

(continues)

Table 10. Continued.

	Cobalt-60		4 MV			6 MV		15 MV			18 MV	
	10×10	20×20	5×5	10×10	20×20	10×10	20×20	5×5	10×10	20×20	10×10	20×20
15.1			1.381	1.331	1.246				1.140	1.140		
15.4								1.108	1.143	1.133		
15.9								1.145	1.146	1.133		
16.4								1.154	1.146	1.132		
17.4			1.397	1.323	1.264				1.155	1.136		
19.6								1.192	1.167	1.151		
20.4			1.408	1.344	1.282							
21.4								1.197	1.166	1.147		
23.9			1.412	1.370	1.311			1.213	1.174	1.151		
25.4			1.418	1.372	1.305							
26.4								1.210	1.176	1.154		
28.9								1.214	1.182	1.158		

DB: thickness of build up layer of solid water, ST: thickness of lung-equivalent slab.

Table 11. "Inhomogeneity Correction Factors" for heterogeneities composed of lung-equivalent plastic.

Lung Split Slabs

	Cobalt-60		**4 MV**			**6 MV**		**15 MV**			**18 MV**	
	10 × 10	20 × 20	5 × 5	10 × 10	20 × 20	10 × 10	20 × 20	5 × 5	10 × 10	20 × 20	10 × 10	20 × 20
DB	3 cm		5 cm			3 cm		5 cm			3 cm	
ST	5 cm		16 cm			5 cm		16 cm			5 cm	
S	2.5 cm		2 cm			2.5 cm		2 cm			2.5 cm	
0.5	1.001	0.998										
1.0	0.999	0.995										
1.6						0.999	– – – –					
1.8						– – – –	0.990					
2.0	0.996	0.990				0.997	0.990					
3.0	0.994	0.986				0.990	0.998					
3.3											0.997	0.996
4.0	0.987	0.981				0.993	0.988				0.994	0.993
5.0	0.981	0.973				0.989	0.984				0.990	0.991
6.0	0.976	0.967	0.993	0.986	0.980	0.985	0.980	0.987	0.984	0.986	0.986	0.988
7.0	0.971	0.961				0.981	0.978				0.984	0.985
8.0	0.967	0.958				0.978	0.977				0.984	0.984
9.0	0.966	0.959				0.977	0.975				0.985	0.984
10.0	0.969	0.960	0.973	0.948	0.944	0.980	0.979	0.966	0.972	0.974	0.987	0.986
11.0	0.972	0.964				0.981	0.982				0.988	0.984
12.0	0.979	0.970				0.983	0.985				0.988	0.987
13.0	0.983	0.975				0.987	0.987				0.989	0.986
14.0	0.989	0.981	0.960	0.931	0.933	0.992	0.990	0.950	0.956	0.959	0.990	0.988
15.0	0.995	0.987				0.993	0.996				0.991	0.988
18.0			0.957	0.922	0.928			0.953	0.952	0.959		
21.0												

(continues)

Table 11. Continued.

	Cobalt-60		4 MV			6 MV		15 MV			18 MV	
	10 × 10	20 × 20	5 × 5	10 × 10	20 × 20	10 × 10	20 × 20	5 × 5	10 × 10	20 × 20	10 × 10	20 × 20
22.0			0.968	0.933	0.948							
22.9								0.991	0.967	0.975		
26.0			1.010	0.986	1.002							
27.1								1.007	0.982	0.990		
30.0			1.037	1.049	1.059							
30.1								1.014	0.999	1.003		
34.9			1.057	1.110	1.126							
35.1								1.021	1.018	1.022		
35.6			1.052	1.101	1.115							

DB: thickness of build up layer of solid water, ST: thickness of lung-equivalent slab, S: separation between the lung-equivalent slabs (split slab geometry)

Table 12. "Inhomogeneity Correction Factors" for heterogeneities composed of bone-equivalent plastic.

Bone

	Solid Slab						**Split* Slab**					
	Cobalt-60		**6 MV**		**18 MV**		**Cobalt-60**		**6 MV**		**18 MV**	
	10 × 10	20 × 20	10 × 10	20 × 20	10 × 10	20 × 20	10 × 10	20 × 20	10 × 10	20 × 20	10 × 10	20 × 20
DB	3 cm		3 cm		3 cm		3 cm		3 cm		3 cm	
ST	3 cm		3 cm		3 cm		3 cm		3 cm		3 cm	
S	– – –		– – –		– – –		2.5 cm		2.5 cm		2.5 cm	
0.5							1.004	1.007				
1.0							1.004	1.011				
1.6									1.004	– – –		
1.8									– – –	0.998		
2.0							1.006	1.013	1.006	0.999		
3.0	* * Interface * *		* * Interface * *		* * Interface * *		1.008	1.017	1.005	1.002		
3.3											1.012	1.011
4.0	0.987	0.967	0.940	0.938	0.976	0.971	1.011	1.020	1.014	1.007	1.017	1.016
5.0	0.983	0.984	0.931	0.936	0.972	0.966	1.015	1.022	1.020	1.011	1.022	1.024
6.0	* * Interface * *		* * Interface * *		* * Interface * *		1.018	1.026	1.018	1.015	1.023	1.024
6.2			0.925	0.929	0.987	0.988						
6.4			0.934	0.938	0.982	0.986						
6.7			0.938	0.944	0.978	0.982						
7.0	0.932	0.937	0.946	0.948	0.968	0.971	1.019	1.027	1.019	1.015	1.019	1.020
8.0	0.925	0.935	0.944	0.949	0.957	0.963	1.019	1.029	1.017	1.017	1.015	1.015
9.0	0.921	0.931	0.941	0.947	0.951	0.957	1.017	1.028	1.017	1.017	1.012	1.014
10.0	0.918	0.928	0.939	0.945	0.948	0.953	1.016	1.026	1.018	1.019	1.012	1.013
11.0	0.913	0.925	0.937	0.944	0.945	0.952	1.012	1.022	1.015	1.018	1.011	1.010
12.0	0.909	0.922	0.935	0.943	0.944	0.951	1.010	1.019	1.014	1.017	1.009	1.011

(continues)

Table 12. Continued.

	Solid Slab						**Split* Slab**					
	Cobalt-60		**6 MV**		**18 MV**		**Cobalt-60**		**6 MV**		**18 MV**	
	10 × 10	20 × 20	10 × 10	20 × 20	10 × 10	20 × 20	10 × 10	20 × 20	10 × 10	20 × 20	10 × 10	20 × 20
13.0	0.907	0.920	0.933	0.941	0.942	0.949	1.006	1.016	1.012	1.016	1.009	1.010
14.0	0.903	0.917	0.931	0.941	0.941	0.948	1.003	1.016	1.014	1.016	1.008	1.011
15.0	0.901	0.915	0.930	0.938	0.940	0.946	1.001	1.012	1.012	1.016	1.007	1.009

DB: thickness of build up layer of solid water, ST: thickness of bone-equivalent slab, S: separation between the bone-equivalent slabs (split slab geometry)

*Note: 2.5-cm gap at split.

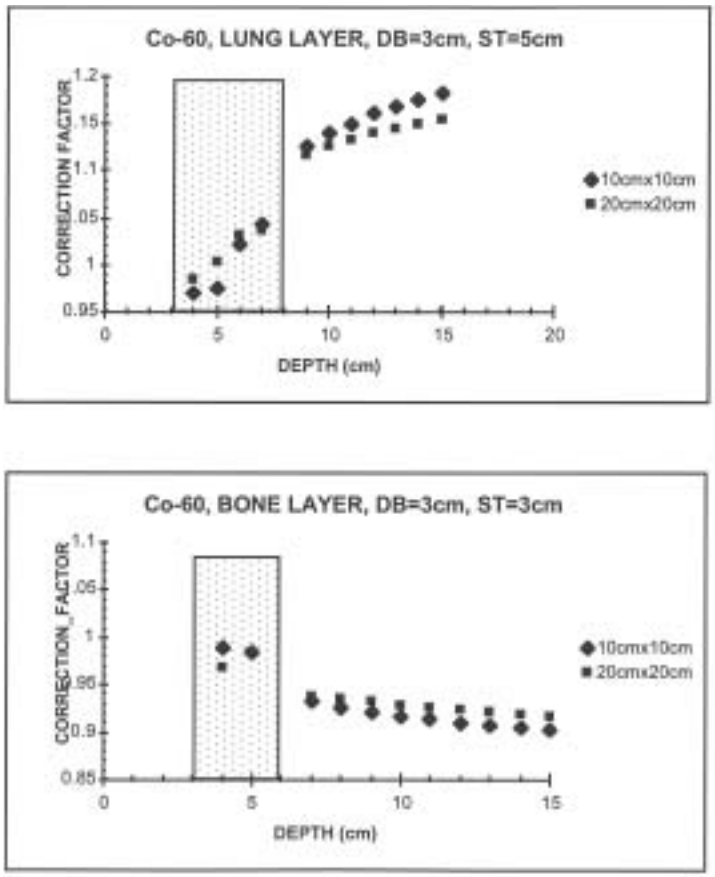

Figure 30. Inhomogeneity correction factor for cobalt-60 for two different field sizes as a function of depth below the surface of the phantom. (a) lung slab, (b) bone slab.

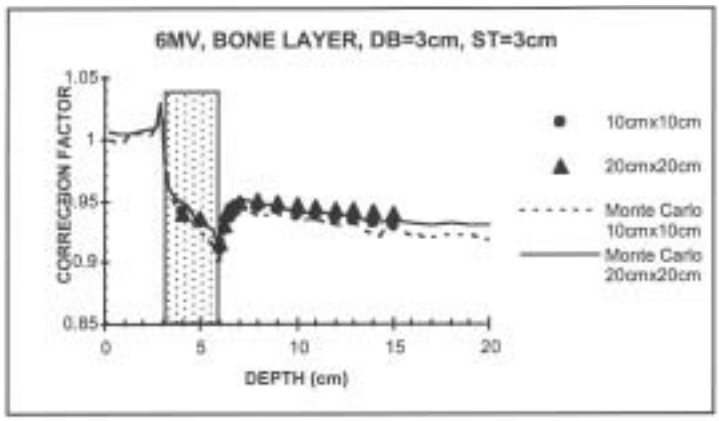

(a)

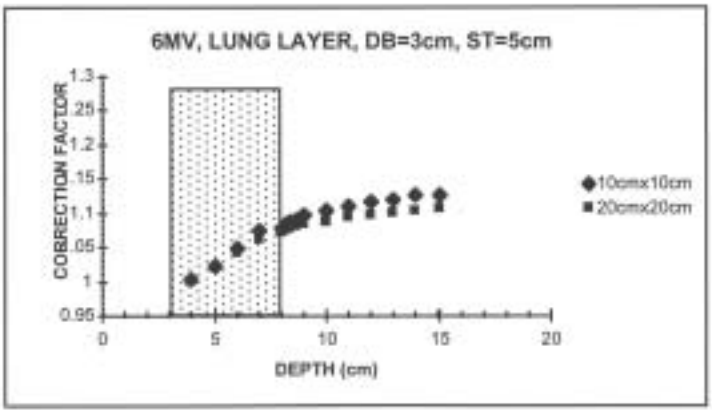

(b)

Figure 31. Inhomogeneity correction factor as a function of depth in a layered bone (a) and lung (b) phantoms for a 6 MV photon beam with field sizes of 10×10 and 20×20 cm^2.

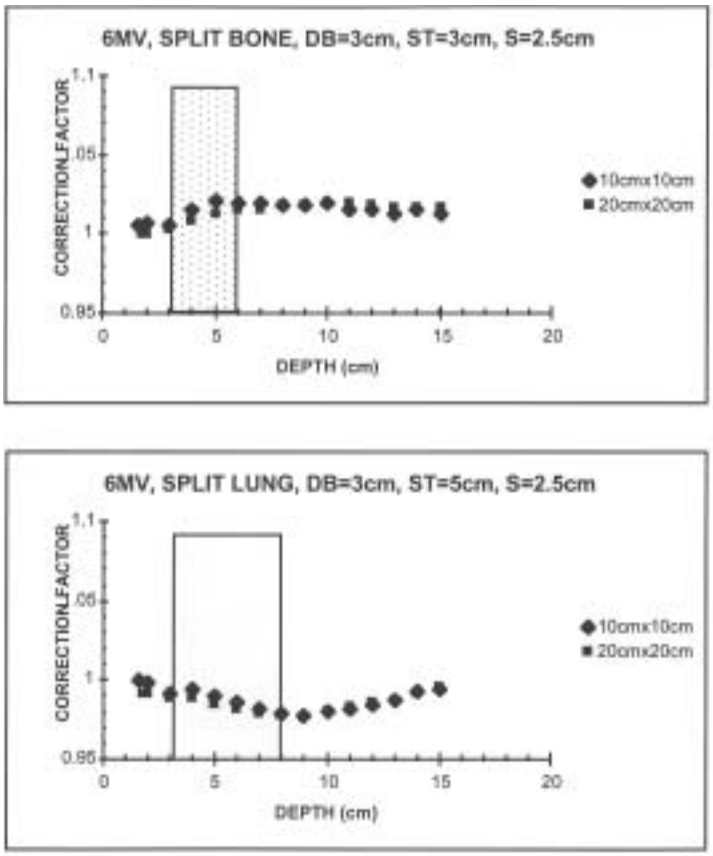

Figure 32. Dose correction factor as a function of depth in mediastinum bone (a) and lung (b) phantoms for 6 MV x-rays with field sizes of 10×10 and 20×20 cm^2.

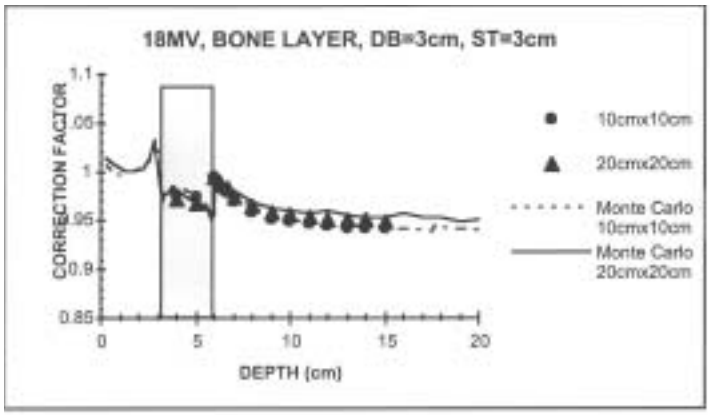

(a)

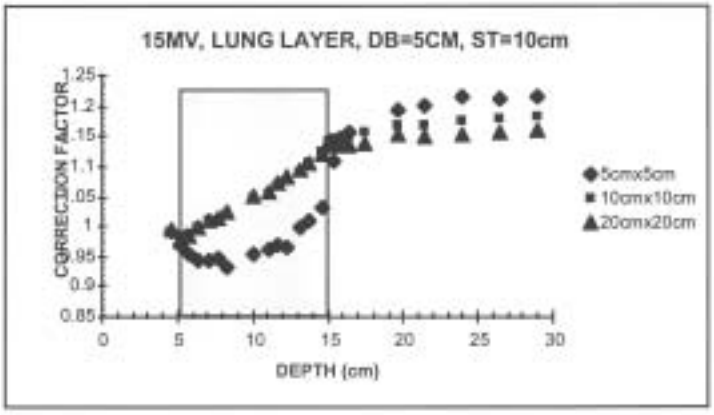

(b)

Figure 33. Inhomogeneity correction factor as a function of depth in (a) layered bone phantom for an 18 MV photon beam with field sizes of 10×10 and 20×20 cm^2 and (b) lung phantom for a 15 MV photon beam with field sizes of 5×5, 10×10, and 20×20 cm^2.

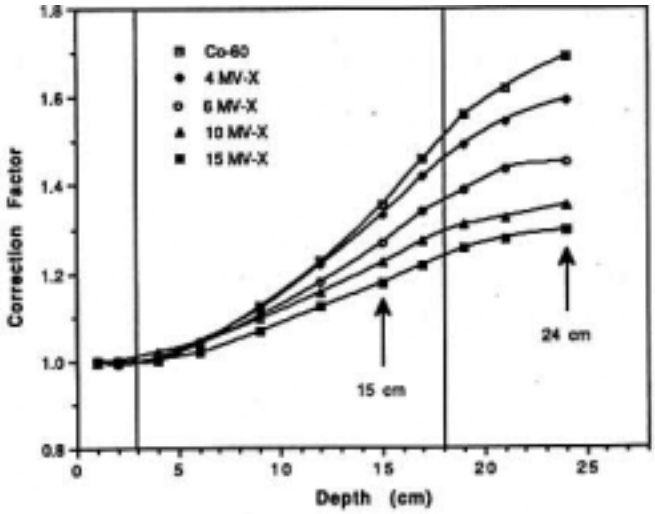

Figure 34. A 10×10 cm^2 field is plotted for lung heterogeneity for a range of energies between cobalt-60 and 15 MV. Beyond the lung slab the ICF is greater than unity due to the higher primary transmission through the slab. (Reprinted from P. J. Gullane,[85] "Primary mandibular reconstruction: analysis of 64 cases and evaluation of interface radiation dosimetry on bridging plates," *Laryngoscope* 101:1–24 (1991) with permission of Lippincott Williams & Wilkins.)

the narrow scattering angle of the higher energy x-rays. The details of the ICFs are complex and vary significantly with energy. This sample of data illustrates the major characteristics.

H. Data Trends

Although there is an abundance of measured data that often leads to different conclusions, there are still some consistent messages. Some are obvious and others require closer analysis.

- Doses increase downstream beyond ($> d_{max}$) low-density media (air, lung).
- There are build-up and build-down regions within tissue near the interface of the low-density media. The severity increases with increasing energy, decreases with increasing field size.
- The penumbra increases in the region of low-density medium and increases with energy.
- Doses decrease downstream beyond ($> d_{max}$) high-density media (bone, metal prosthetics).

The physicist is strongly advised to understand these trends, especially as they apply to specific clinical situations and how their treatment planning system does or does not account for them.

VI. THE EFFECT OF INHOMOGENEITY IN IMRT

The impact of the inclusion of inhomogeneity corrections for intensity-modulated radiation therapy (IMRT) can be more complex than for conventional 3D planning, partly due to the combinatorial effect of many small fields, the presence of inhomogeneity, and the presence of steep fluence gradients. Papanikolaou et al.[204,387,388,389] have studied the effect of inhomogeneity corrections for non-small-cell lung cancer and found that errors up to 6% can be expected (see Figure 35a,b,c and related Table 13).

Most commercial inverse treatment planning systems for IMRT rely on fast but approximate dose calculation algorithms such as the finite sized-pencil beam method.

Use of inaccurate dose calculation in iterative inverse treatment planning for IMRT introduces two errors in the plan. One is the systematic error, which is similar to the systematic error in the conventional treatment planning. The second is the convergence error that appears because the optimization converges to the solution optimal for the inaccurate dose calculation beamlets, which is different from the solution for the accurate dose calculation. The convergence error is similar to the noise convergence error, which appears when Monte Carlo dose calculation is used in inverse treatment planning.[390,391]

A study of three cases (head and neck, lung, and prostate) with the use of several different objective functions by Jeraj et al.[391] was performed to characterize both errors. While the systematic error was found to be small for superposition (1%), it was much larger for pencil beam dose calculation (up to 8%), even though dose calculations in water were accurate to within 1%.

The convergence error is dependent on the systematic error of the dose calculation method; however, it is also very strongly dependent on the specified objectives. It was found to be smaller for superposition than the pencil beam method for the objectives studied. Because of the current uncertainty in the definition of the optimality and definition of the objective function, the clinical significance of the convergence error is unclear. The clinical significance of the convergence error could be reduced if the final dose calculation is performed with an accurate dose calculation. In the case that the final plan, based upon an accurate dose calculation, is judged to be still acceptable, the existence of a better plan (i.e., removal of the convergence error) is of little consequence. If, however, compromises still exist in the final plan, the existence of the convergence error could be clinically important.

As both the systematic and convergence errors were found to be significant for the pencil beam calculations, the reported results suggest that vendors and users who currently use pencil-beam-based dose calculations for IMRT should

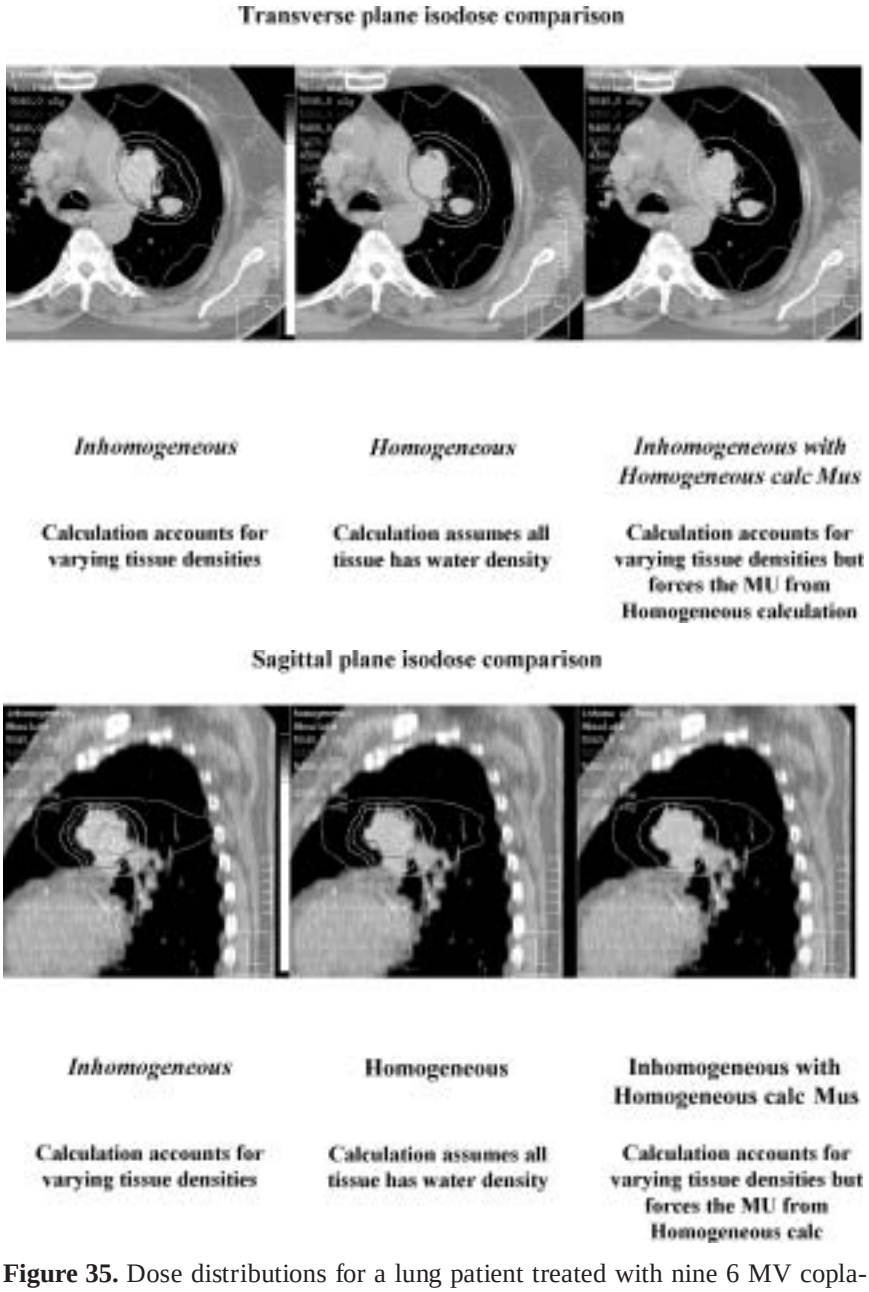

Figure 35. Dose distributions for a lung patient treated with nine 6 MV coplanar IM beams in (a) transverse, (b) sagittal, and (c) coronal views. Calculations were performed using a superposition/convolution algorithm and compared to a homogeneous calculation. For comparison, the distribution using the superposition algorithm but with the homogeneously computed MU is also shown.

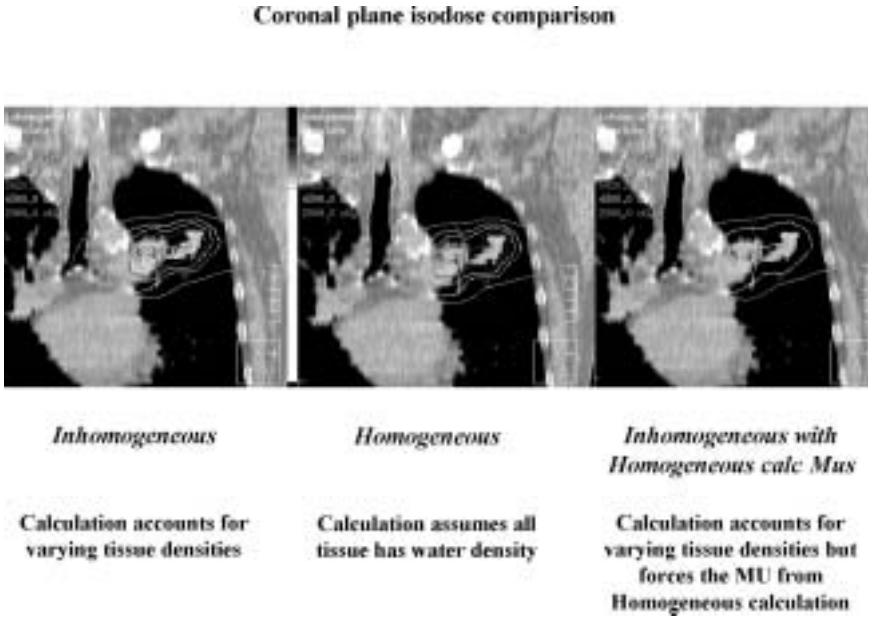

Figure 35. Continued.

Table 13. Comparison of dose to target and organs at risk for a lung patient demonstrating the effect of inhomogeneity correction. Dose normalization is beams isocenter. Volumes correspond to the entire organ (lung and

	Homogeneous Calculation		**Inhomogeneous Calculation**		**Inhomogeneous w/ Homogeneous MUs**		**Ratio of Inhomogeneous MUs and Homogeneous**	
	Max. Dose cGy	**Mean Dose** cGy	**Max. Dose** cGy	**Mean Dose** cGy	**Max. Dose** cGy	**Mean Dose** cGy	**Max. Dose Ratio** in %	**Mean Dose Ratio** in %
GTV	5400	5348	5429	5384	5092	5045	–5.7	–5.7
Adenopathy	5420	5341	5451	5399	5109	5049	–5.7	–5.5
Lt. Lung	5393	1057	5451	1077	5110	1012	–5.2	–4.2
Soft Tissue	5420	293	5457	299	5115	277	–5.6	–5.4

upgrade to either superposition or Monte Carlo-based dose calculation, at least for the final dose calculation to eliminate the systematic error. The same reason (lack of accuracy) that has been driving treatment planning system vendors and users to improve their dose calculation algorithms for conventional forward treatment planning, should also be considered in IMRT.

Comparison between importance of dose calculation accuracy and statistical uncertainty for inverse treatment planning[390,391] shows (see Figures 36 and 37 and

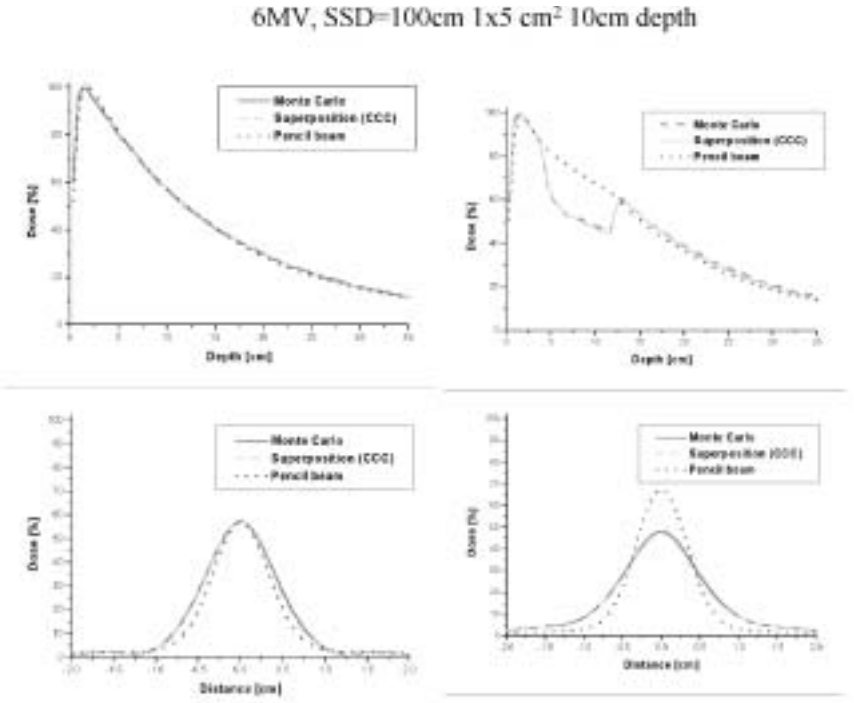

Figure 36. 6 MV 100 cm SSD depth dose curves (top) and profiles at 10 cm depth (bottom) in water for narrow 1×5 cm^2 fields as calculated by Monte Carlo, superposition (collapsed cone convolution), and pencil beam dose calculation. While depth dose curves agree well, the pencil beam dose profile shows an underdose in the penumbra region. Comparisons for a water/lung/water phantom are also shown. Note the good agreement between the Monte Carlo and superposition depth dose and dose profile curves, and the overestimation of the pencil beam depth dose curve within the lung and the underestimation of the lateral dose spread within the lung region (Reprinted from R. Jeraj, P. J. Keall, and J. V. Siebers,[391] "The effect of dose calculation accuracy on inverse treatment planning," *Phys. Med. Biol.* 47:391–407 (2002) with permission from the Institute of Physics Publishing.)

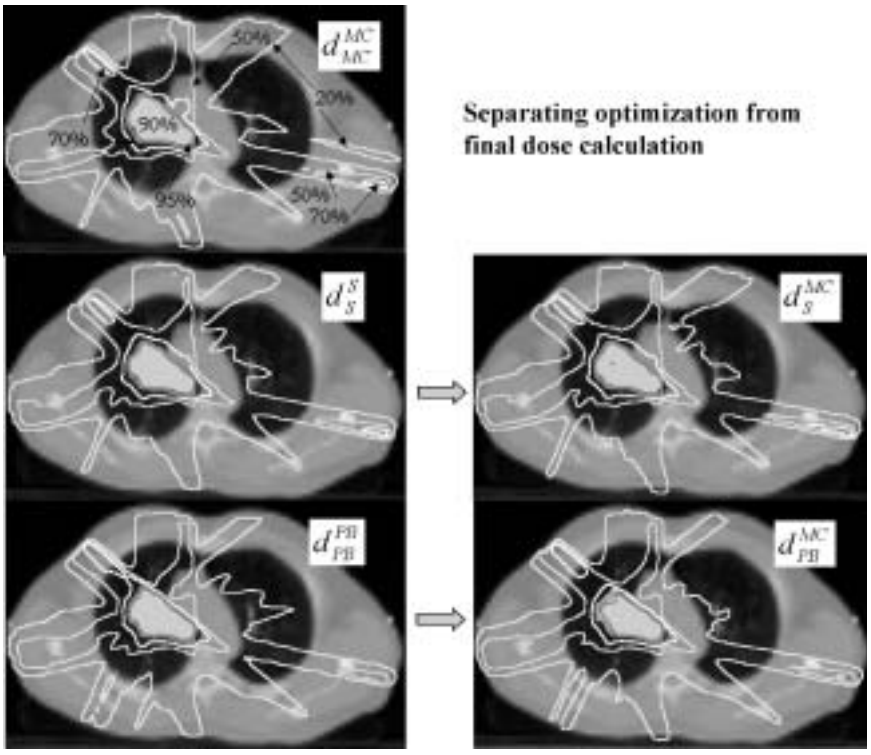

Figure 37. Optimal (left) and recalculated (right) dose distributions for the lung tumor case: Monte Carlo (d_{MC}^{MC} upper left), superposition (d_S^S middle left), recalculated superposition (d_S^{MC} middle right), pencil beam (d_{PB}^{PB} lower left) and recalculated pencil beam (d_{PB}^{MC} lower right). The following isodose curves are shown: 20% (blue), 50% (green), 70% (yellow), 90% (orange) and 95% (red). The objective function used for the optimization in these cases was exponential (tumor) with sparing of the left lung. (Reprinted from R. Jeraj, P. J. Keall, and J. V. Siebers,[391] "The effect of dose calculation accuracy on inverse treatment planning," *Phys. Med. Biol.* 47:391–407 (2002) with permission from the Institute of Physics Publishing.)

Table 14) that the systematic and convergence errors for superposition type of dose calculation are approximately equal to the 2% statistical error of a Monte Carlo dose calculation. Therefore, to gain anything with the use of Monte Carlo dose calculation in inverse treatment planning, precision of the dose calculation should be below 2% for the final dose distribution, which is in agreement with the data reported by Keall et al.[392] for Monte Carlo precision in conventional treatment planning. However, since there is also some systematic error in the definition of the linear accelerator geometry and/or source model used for charac-

Table 14. Systematic and convergence errors for superposition and pencil beam dose calculations. The mean difference and standard deviations are given for the systematic error and the range of standard deviations for the convergence error. The ranges in the convergence error indicate the differences observed between different objective functions. (a) Errors for the lung tumor and left lung, (b) errors for the prostate tumor and rectum and (c) errors for the head & neck tumor and spinal cord.

(a)

	Superposition		**Pencil beam**	
Error (%D_{max})	**Tumor**	**Lung**	**Tumor**	**Lung**
Systematic	–0.1 ± 2	–1 ± 1	+8 ± 3	+6 ± 5
Convergence	2–5	1–4	3–6	6–7

(b)

	Superposition		**Pencil beam**	
Error (%D_{max})	**Tumor**	**Lung**	**Tumor**	**Lung**
Systematic	–0.3 ± 2	–1 ± 1	+5 ± 1	+6 ± 1
Convergence	2–5	2–7	3–6	2–5

(c)

	Superposition		**Pencil beam**	
Error (%D_{max})	**Tumor**	**Lung**	**Tumor**	**Lung**
Systematic	–0.1 ± 2	–3 ± 1	–3 ± 2	+2 ± 1
Convergence	3–6	1–3	3–4	1–3

terizing the phase space of particles used in Monte Carlo simulations, which are typically of the order of 1% to 2%, superposition dose calculation in inverse treatment planning might be sufficient for the current accuracy of dosimetry protocols and geometry modeling in Monte Carlo simulations. On the other hand, the difference in speed between superposition and fast Monte Carlo dose computations is getting less, therefore, one might consider employing Monte Carlo dose calculation to avoid potential problems with the accuracy (especially in difficult cases like head and neck, metal implants, etc.), which might be even more severe when the actual beam delivery characteristics are taken into account.

VII. SUMMARY AND RECOMMENDATIONS

The uncertainty on the dose at a point in the patient is due to a combination of largely independent sources of error including patient movement, fluctuations in machine output, uncertainty in the basic calibration of the reference

point in terms of dose, and, very significantly, uncertainties in the very complex calculation which corrects the measured distribution in a water phantom for the irregular patient skin surface and the inhomogeneities in the body; most notably bone, air passages, cavities, and lung. The problem of the radiation transport can be summarized as follows: photons scatter through the Compton process, not just singly, but multiply, and the dose is actually delivered not by primary or scattered photons, but by primary electrons which transport the energy away from the point where they were generated; a 6 MeV electron will travel approximately 2.5 cm in water. Both of these phenomena are very difficult to deal with analytically and a solution to only one of these transport problems is of limited value for higher energy x-ray beams incident on low-density media.

The accuracy of a calculation is a complex function of the dose algorithm, the number of beams, the site that is irradiated, the geometry that was used, and the resolution of the dose calculation grid.

Although the currently implemented algorithms for inhomogeneity corrections often overestimate or underestimate the actual dose to the patient, they still present the treatment planner with a better solution compared to not performing any inhomogeneity correction at all.[23,24,25,26,28,31] In other words, the inherent estimations are often closer to the actual values than those calculations with no inhomogeneity corrections. The 3D scatter integration algorithms, such as convolution and superposition do account in first approximation for the photon scatter component, and some also can predict the change in dose where electron disequilibrium exists. This requires that the primary scatter kernel, representing electron transport, be used explicitly and independently of the photon scatter kernels during the superposition procedures. As discussed in section IV, Monte Carlo algorithms are now becoming more attractive in a clinical setting, since it only takes a few minutes (PEREGRINE, Macro-MC) to a fraction of an hour to calculate the dose with complex geometries where both the photon and the electron component of the dose are more correctly transported through the inhomogeneities.

Table 15 describes many of the current (August 2003) commercial treatment planning systems and their photon algorithms. Please note that the table represents a sampling of treatment planning systems familiar to the Task Group members and is not intended to be exhaustive. There is no implied value judgment on a particular system or algorithm if it has not been included in the table.

In terms of the dose calculation parameters, the resolution of the dose grid becomes an important factor in evaluating the effect of the inhomogeneities. When large voxel sizes are used in the computation, there is an interpolation that reduces the accuracy of the calculation, especially in areas where dose gradients are steep such as the penumbra, build-up region, and interfaces. This is a special concern for IMRT, where very small pencil beams (″ 5 mm) are used for calculations and treatment. In this situation, the penumbra is much more significant and grid size limitations can lead to erroneous distributions for these very small pencil beams.

Table 15. Dose calculation algorithms of commercial treatment planning systems.

Company	Product	Version	Algorithm
3D LINE MEDICAL SYSTEMS	DYNART/ERGO	1.4.1.	• 3D Pencil Beam Based Algorithm • Equivalent Path Length
BRAINLAB	BRAINSCAN (Stereo)		Pencil Beam algorithm
Computerised Medical Systems—CMS	FOCUS	2.4.0	• Clarkson (effective pathlength) • FFT convolution kernels (not scaled but beam hardening taken into account)
Computerised Medical Systems—CMS	FOCUS	2.5.0 and later	Multigrid Superposition (convolution kernels scaled with density)
Computerised Medical Systems—CMS	XIO	3.2.1	FFT Convolution / Superposition, Collapsed Cone Convolution
ELEKTA	PrecisePLAN	1.1	TAR and 3D SAR integration
FIXMA	DOSIGRAY		
STRYKER—LEIBINGER	RADIO PACKAGE		Virtuoso: Pencil beam based convolution algorithm with inhomogeneity correction
LLNL	PEREGRINE first release		3D Monte Carlo
MEDICALIBRATION	PC3D EXPERT SYSTEM		Pencil Beam
MDS NORDION	THERAPLAN Plus	3.5	Equivalent TAR plus electron transport
MDS NORDION	HELAX-TMS	6.0	• pencil kernel with depth scaling • collapsed cone point kernel with 3D scaling
MDS NORDION	ONCENTRA - OTP	1.0	• pencil kernel with depth scaling • collapsed cone point kernel with 3D scaling

(continues)

Table 15. Continued.

Company	Product	Version	Algorithm
MEDTRONIC SOFAMOR DAINEK	ARTS 3D	2.1	ETAR (equivalent TAR)
MKS Inc	MKS 3D		• Differential SAR method • Batho method
MULTIDATA	DSS+		PRISM (effective) path length algorithm
NOMOS	CORVUS PEREGRINE	1.0	1D ray trace
NUCLETRON	Plato RTS 3D	2.5.2	ETAR method (Yu and Wong)
PHILIPS/ MARCONI	ACQPLAN 3D		
PHILIPS	PINACLE^3	6.2d	Adaptive collapsed cone convolution / superposition
PRISM MICRO-SYSTEMS	PRISM-TPS		
PROWESS	PROWESS - 3D		• Effective Path Length • Batho Power Law Method
RHAD	RHAD - 3D		
ROCS	ROCS	5.0	• Equivalent path length • TMR ratio
TECHNO-LOGIE DIFFUSION / INSTITUTE CURIE / EUREKA	ISIS 3D	2.33	Clarkson—Cunningham, 3D Beam Substraction Method
VARIAN	ECLIPSE		• Modified Batho power law method • ETAR

It has also been observed in clinical measurements that inhomogeneity corrections are less important for multiple beam arrangements. In addition, beam energy has bearing as to complexity of the heterogeneity correction and as to decision on treatment margins and even prescriptions. On the surface of this issue, it is obvious that the lower the energy the larger the correction on central axis to points far from interfaces where electron equilibrium exists. However,

the corrections are more complex and even contradictory depending on algorithm, as the energy increases. Therefore, the clinician should be made aware of the constraints with high-energy beams and heterogeneity corrections when, not only prescribing, but also when choosing energies. Some examples of where energy and related heterogeneity correction considerations should mandate using low-energy photon beams, include: larynx (due to additive underdosage effects of missing tissue and air cavity; chest wall (due to the absence of breast tissue and underlying lung); and coin lesions in the lung (due to the non-equilibrium condition).

The Task Group has the following recommendations:

- The Task Group recommends that heterogeneity corrections be applied to treatment plans and dose prescriptions, with the provision that the algorithms used for the calculations are reviewed and tested[384] by the medical physicist. Discussions pertaining to the application of inhomogeneous calculations for specific clinical sites should be initiated with the clinicians, so they can appreciate and anticipate the changes in the treatment plans. While reviewing the algorithms, the medical physicist should seek answers to some basic concepts, such as, "Is scatter corrected for in 1D, 2D, or 3D?" or, "Does the algorithm handle electron transport?" It is clear that simple 1D algorithms are suitable in most clinical situations where interest points are far from the heterogeneous media, but will most likely fail proximal to an interface. In the following clinical examples, we shall describe the performance requirements for a dose algorithm.
- Head and Neck: For points of interest well beyond the mandible and air cavities, even simplistic 1D equivalent path corrections are reasonable for point dose estimates. However, for soft tissue regions that are within the proximity of these heterogeneous structures, the superposition/convolution or Monte Carlo algorithms may be considered. Another limitation comes into play with the presence of high-Z implanted mandible wires. The user should ensure that the algorithm properly accounts for the attributes of the high atomic number or otherwise correct for the high-Z implant. Refer to the TG 63 report[48] for specific recommendations on how to implement such procedures.
- Larynx: For points of interest well beyond the air-tissue interface (beyond d_{max}), even simplistic 1D equivalent path corrections are reasonable for point dose estimates. However for ascertaining dosage at tumor-air interfaces and for accounting for disturbed scatter conditions, the superposition/convolution or Monte Carlo algorithms may be considered. The most severe case is the location of the anterior commissure, which is located anterior to the cavity and does not have enough tissue build-up upstream.
- Lung: For points of interest well beyond the lung even simplistic 1D equivalent path corrections are reasonable for point dose estimates. However for ascertaining dosage at tumor-lung interfaces and for accounting for disturbed scatter and equilibrium, the superposition/convolution or

Monte Carlo algorithms may be considered. The strongest test is to calculate accurately the peripheral dose of a tumor that is imbedded within lung in the presence of small, high-energy fields. Loss of electron equilibrium within and adjacent to lung can result in a dose reduction along the central axis and near the beam edge for megavoltage photon beams. In this context, it is recommended to use photon beams of energy 12 MV or less for non-small-cell lung cancer therapy.

- Breast: As the entire breast parenchyma is the planning target volume in this case, the heterogeneity question is complex. As CT-based planning is becoming an acceptable method of simulating and planning breast cancer patients, more data are available to the planner, physicist, and physician to ascertain the effects of the presence of lung below the chest wall (see Butker et al.[393]). Though the calculated dose to most of the breast tissue is not affected by the presence of the lung below the chest wall (typically prescription points are anterior enough from the chest wall), the loss of lateral photon scatter can be significant. Also, optimization of compensators (wedges, etc.) is affected by the presence of lung tissue as the increased dose to the corners of the breast, lateral to the lung, but can be somewhat predicted by simplistic 1D equivalent path corrections. However, the dose distribution to the chest wall itself is greatly affected by the adjacent lung. Dosimetric improvement can be achieved if applying a complex 3D plan utilizing multiple contours instead of simple contours based on manual methods. Consequently, calculations to the chest wall must be accurately calculated and therefore, the superposition/convolution or Monte Carlo algorithms may be considered. The same recommendation applies to post-mastectomy patients.
- Upper GI: The abdomen is a site relatively insensitive to the inclusion of inhomogeneity corrections. Although it is tempting to suggest that one need not be concerned with corrections for this site, one should remember that the effects are highly dependent on the specific geometry. Transient gas and barium are potential problems if observed on CT since they are not stable and, therefore, corrections will not be representative of the actual dose delivered to the patient. When barium contrast is used, the signal-enhanced volume can be contoured and its density can be overridden (to unity) to remove any erroneous increased dose absorption due to the high density of the contrast agent.
- Pelvis and Prostate: For points of interest well beyond the femoral heads, even simplistic 1D equivalent path corrections are reasonable for point dose estimates. The main limitation comes into play with the presence of high-Z implanted hip prostheses. The user needs to evaluate whether the algorithm properly accounts for the attributes of the high-atomic number. For the most part, interface and lateral scattering issues are not a factor for the pelvis region. See AAPM TG 6348 for a full description of issues associated with high-Z hip prostheses.

In summary:

(1) The physicist needs to understand the algorithm(s) that are within the treatment planning system and monitor unit calculation programs.
(2) The physicist is strongly advised to test the planning system to ascertain if the system can predict the common trends listed at the end of section V. The physicist may use some of the benchmark data presented in Tables 10 through 12 or within the references directly. The data presented in Tables 10 through 12 are also to be used by vendors of treatment planning systems to test their algorithms. The Task Group recommends that potential clients should ask a vendor for the results of these calculations.
(3) The physicist is advised to measure benchmark data for his/her own beam and compare with the calculated (planning system or hand calculations) data. If possible, the physicist may also use Monte Carlo calculations to support measured data.
(4) The physicist should understand the importance of the dose calculation resolution grid. Its value is typically user selectable. As the resolution decreases (e.g., 0.6 cm grid) the calculation gets faster but the effect of the inhomogeneity is less resolved due to volumetric averaging. If the dose needs to be accurately evaluated, especially in areas of steep dose gradients and tissue interfaces, a high-resolution grid (e.g., 0.2 cm grid) should be employed.
(5) The physicist should maintain an open dialogue with the clinician and be clear on limitations of the planning system. If the clinician is comfortable with using corrections to dose prescriptions and dose distributions for inhomogeneities, then the following learning curve is recommended. For each clinical site (e.g., left breast, right lung, larynx, etc.), there should be 5 to 10 treatment plans generated, with and without inhomogeneity corrections. The dose prescription should be the same for both cases. The plans should be compared, with differences highlighted in absolute dose and dose coverage. This should also be repeated if a new algorithm is implemented or a new release of software is received.
(6) The physicist should keep abreast of new algorithm developments and, if evaluating the purchase of a new treatment planning system, be thoroughly informed as to the accuracy and adequacy of its ability to deal with tissue inhomogeneities. The vendors should provide clear documentation of the inhomogeneity correction methods implemented in their systems. The vendors also should be strongly encouraged to provide algorithm in-services at their user's meetings.
(7) Since physicists usually teach residents, tissue inhomogeneity effects on the doses delivered at the main clinical sites should be carefully discussed in residents' physics didactic lectures. Comparative plans, as

described in paragraph 5 above, are an important teaching tool and physicists should advise residents to run them for themselves.

(8) The physicist should finally confirm that the method to calculate treatment time or monitor units, whether it is derived by the treatment planning software, or with an alternative method, is accurate to deliver the planned absolute dose to the point of interest.

VIII. REFERENCES

1. B. Emami, J. Lyman, A. Brown, L. Coia, M. Goitein, F. W. Munzinrider, B. Shank, L. J. Solin, and M. Wesson, "Tolerance of normal tissue to therapeutic irradiation," *Int. J. Radiat. Oncol. Biol. Phys.* 21:109–122 (1991).
2. C. Burman, G. J. Kutcher, B. Emami, and M. Goitien, "Fitting of normal tissue tolerance data to an analytic function," *Int. J. Radiat. Oncol. Biol. Phys.* 21:123–135 (1991).
3. H. D. Thames and J. H. Hendry, *Fractionation in Radiotherapy*. (London: Taylor & Francis) (1987).
4. K. Mah, J. Van Dyk, T. J. Keane, and P. Y. Poon, "Acute radiation induced pulmonary damage: a clinical study on the response to fractionated radiation therapy," *Int. J. Radiat. Oncol. Biol. Phys.* 13:179–188 (1987).
5. B. J. Mijnheer, J. J. Battermann, and A. Wambersie, "What degree of accuracy is required and can be achieved in photon and neutron therapy?" *Radiother. Oncol.* 8:237–252 (1987).
6. M. K. Martel, R. K. Ten Haken, M. B. Hazuka, M. L. Kessler, M. Strawderman, A. T. Turrisi, S. T. Lawrence, B. A. Fraass, and A. S. Lichter, "Estimation of tumor control probability model parameters from 3-D dose distributions of non-small cell lung cancer patients," *Lung Cancer* 24(1):31–37 (1999).
7. P. Mavroidis, B. K Lind, J. Van Dijk, K. Koedooder, W. De Neve, C. De Wagter, B. Planskoy, J.-C. Rosenwald, B. Proimos, C. Kappas, C. Danciu, M. Benassi, G Chierego and A. Brahme, "Comparison of conformal radiation therapy techniques within the dynamic radiotherapy project 'DYNARAD'," *Phys. Med. Biol.* 45:2459–2481 (2000).
8. A. Brahme, "Dosimetric precision requirements in radiation therapy," *Acta Radiol. Oncol.* 23:379–391 (1984).
9. P. Kallman, Optimization of Radiation Therapy Planning Using Physical and Biological Objective Functions. Ph.D. Thesis, Department of Radiation Physics, Stockholm University (1992).
10. P. Kallman, A. Ågren, and A. Brahme, "Tumour and normal tissue responses to fractionated non-uniform dose delivery," *Int. J. Radiat. Biol.* 62:249–62 (1992b).
11. P. Kallman, B. K. Lind, and A. Brahme, "An algorithm for maximizing the probability of complication-free tumour control in radiation therapy," *Phys. Med. Biol.* 37:871–90 (1992a).
12. A. Brahme, "Treatment optimization using physical and radiobiological objective functions," in *Radiation Therapy Physics*, A. Smith (ed.) (Berlin: Springer) (1995).

13. D. F. Herring, and D. M. J. Compton, "The degree of precision required in the radiation dose delivered in cancer radiotherapy," *Comput. Radiother. Br. J. Radiol Special Report* 5:51–58 (1971).
14. A-K. Ågren-Cronqvist, Quantification of the response of heterogeneous tumours and organized normal tissues to fractionated radiotherapy, Ph.D. Thesis, University of Stockholm (1995).
15. J. C. Kim, D. Elkin, and F. R. Hendrickson, "Carcinoma of the vocal cord: results of treatment and time-dose relationships," *Cancer* 42:1114 (1978).
16. A. Dau and J. Denekamp, "Superfractionation as a potential hypoxic cell radiosensitizer: prediction of an optimum dose per fraction," *Int. J. Radiat. Oncol. Biol. Phys.* 43:1083–94 (1999).
17. J. Overgaard and H. Bartelink, "About tolerance and quality. An important notice to all radiation oncologists," *Radiother. Oncol.* 35:1–3 (1995).
18. S. Dische, M. I. Saunders, C. Williams, A. Hopkins, and E. Aird, "Precision in reporting the dose given in a course of radiotherapy," *Radiother. Oncol.* 29:287–93 (1993).
19. A. L. Boyer and T. Schultheiss, "Effects of dosimetric and clinical uncertainty on complication-free local tumor control," *Radiother. Oncol.* 11:65–71 (1988).
20. A. Dutreix, "When and how can we improve precision in radiotherapy?" *Radiother. Oncol.* 2:275–292 (1984).
21. J. G. Stewart and A. W. Jackson, "The steepness of the dose response curve both for tumor curve and normal tissue injury," *Laryngoscope* 85:1107–1111 (1975).
22. S. M. Bentzen, "Radiobiological considerations in the design of clinical trials," *Radiother. Oncol.* 32:1–11 (1994).
23. K. Mah and J. Van Dyk, "On the impact of tissue inhomogeneity corrections in clinical thoracic radiation therapy," *Int. J. Radiat. Oncol. Biol. Phys.* 21:1257–1267 (1991).
24. C. G. Orton, S. Chungbin, E. E. Klein, M. T. Gillin, T. E. Schultheiss, and W. T. Sause, "Study of lung density corrections in a clinical trial (RTOG 88-08)," *Int. J. Radiat. Oncol. Biol. Phys.* 41(4):787–794 (1998).
25. A. Van't Riet, H. C. Stam, A. C. A. Mak, and F. H. S. van Slooten, "Implications of lung corrections for dose specification in radiotherapy," *Int. J. Radiat. Oncol. Biol. Phys.* 11:621–625 (1985).
26. W. G. McKenna, K. Yeakel, A. Klink, B. A. Fraass, J. van de Geijn, E. Glatstien, and A. Lichter, "Is correction for lung density in radiotherapy treatment planning necessary?" *Int. J. Radiat. Oncol. Biol. Phys.* 13:273–278 (1987).
27. H. J. van Kleffens and B. J. Mijnheer, "Determination of the Accuracy of the Tissue Inhomogeneity Correction in Some Computer Planning Systems for Megavoltage Photon Beams," in *Proceedings of the 8th International Conference on the Use of Computers in Radiation Therapy*. Toronto, Canada, (Silver Spring, MD: Computer Society Press IEEE), pp. 45–49 (1984).
28. C. G. Orton, P. M. Mondalek, J. T. Spicka, D. S. Herron, L. I. Andres, "Lung corrections in photon beam treatment planning: are we ready?" *Int. J. Radiat. Oncol. Biol. Phys.* 10(12):2191–9 (1984).
29. Radiation Therapy Oncology Group, "A Phase III Study of Radiation Therapy Alone or in Combination with Chemotherapy for Patients with Non-Small Cell Lung Cancer," RTOG 88-08 (Revision 1991).

30. M. L. Graham, B. Emami, and J. A. Purdy, "A phase I/II dose escalation study using three dimensional conformal radiation therapy in patients with inoperable, non-small cell lung cancer," Radiation Therapy Oncology Group RTOG 93–11 (1999).
31. N. Papanikolaou, E. E. Klein, and W. R. Hendee, "Heterogeneity corrections should be used in treatment planning for lung cancer?" *Med. Phys.* 27 (8), 1702–1704 (2000), Editorial
32. M. J. P. Brugmans, A. van der Horst, J. V. Lebesque, and B. J. Mijnheer, "Beam intensity modulation to reduce the field size for conformal irradiation of lung tumors: a dosimetric study," *Int. J. Radiat. Oncol. Biol. Phys.* 43:893–904 (1999).
33. K. E. Ekstrand and W. H. Barnes, "Pitfalls in the use of high energy x-rays to treat tumors in the lung," *Int. J. Radiat. Oncol. Biol. Phys.* 18:249–252 (1990).
34. P. W. Hoban, P. J. Keal, and W. H. Round, "The effect of density on the 10MV photon beam penumbra," *Australas. Phys. Eng. Sci. Med.* 15(3):113–23 (1992).
35. R. O. Kornelsen and M. E. Young, "Changes in the dose-profile of a 10 MV x-ray beam within and beyond low density material," *Med. Phys.* 9:114–116 (1982).
36. T. Knoos, A. Ahnesjo, P. Nilsson, and L. Weber, "Limitations of a pencil beam approach to photon dose calculations in lung tissue," *Phys. Med. Biol.* 40:1411–20 (1995).
37. M. A. Hunt, G. E. Desobry, B. Fowble, and L. R. Coia, "Effect of low-density lateral interfaces on soft-tissue doses," *Int. J. Radiat. Oncol. Biol. Phys.* 37:475–482 (1997).
38. R. Mohan, Q. Wu, X. Wang, and J. Stein, "Intensity modulation optimization, lateral transport of radiation, and margins," *Med. Phys.* 23:2011–2021 (1996).
39. M. L. Graham, J. W. Matthews, W. B. Harms, B. Emami, H. S. Glazer, and J. A. Purdy, "Three-dimensional radiation treatment planning study for patients with carcinoma of the lung," *Int. J. Radiat. Oncol. Biol. Phys.* 29:1105–1117 (1994).
40. ICRU Report No. 24, "Determination of Absorbed Dose in a Patient Irradiated by Beams of X or Gamma Rays in Radiotherapy Procedures," (Washington, DC: International Commission on Radiation Units and Measurements) (1976).
41. H. Svensson, "Quality assurance in radiation therapy: physical aspects," *Int. J. Radiat. Oncol. Biol. Phys.* 10:59–65 (1984).
42. K. A. Johansson, Studies of Different Methods of absorbed Dose Determination and a Dosimetric Intercomparison at the Nordic Radiotherapy Centers, Thesis, University of Gothenberg, Sweden (1982).
43. A. Brahme et al, "Accuracy requirement and quality assurance of external beam therapy with photons and electrons," *Acta Radiol. Oncol. Suppl.1* (1988).
44. IAEA, Absorbed Dose Determination in Photon and electron Beams. An International Code of Practice, IAEA Technical Report Series No. 277 (Vienna: International Atomic Energy Agency) (1987).
45. J. Venselaar, H. Welleweerd, and B. Mijnheer, "Tolerances for the accuracy of photon beam dose calculations of treatment planning systems," *Radiother. Oncol.* 60:191–201 (2001).
46. J. Van Dyk, R. B. Barnett, J. E. Cygler, P. C. Shragge, "Commissioning and quality assurance of treatment planning computers," *Int. J. Radiat. Oncol. Biol. Phys.* 26:261–73 (1993).

47. P. Andreo, "Uncertainties in dosimetric data and beam calibration," *Int. J. Radiat. Oncol. Biol. Phys.* 19:1233–47 (1990).
48. R. Alecu, C. Reft, I. J. Das, B. J. Gerbi, P. Keall, E. Lief, B. J. Mijnheer, N. Papanikolaou, C. Sibata, and J. Van Dyk, "Dosimetric considerations for patients with hip prostheses undergoing pelvic irradiation," Report of the AAPM Radiation Therapy Committee Task Group 63, *Med. Phys.* 30(6):1162–1182 (2003).
49. H. E. Johns and J. R. Cunningham, *The Physics of Radiology*, (Springfield, IL: C.C. Thomas) (1983).
50. R. Mohan, C.-S. Chui, and L. Lidofsky, "Energy and angular distributions of photons from medical linear accelerators," *Med. Phys.* 12:592–596 (1985).
51. R. Mohan, "Monte Carlo Simulation of Radiation Treatment Machine Heads," in *Monte Carlo Transport of Electrons and Photons*," T. M. Jenkins, W. R. Nelson, A. Rindi (eds.), (New York: Plenum Press), pp. 453–468 (1988).
52. D. W. O. Rogers, B. A. Faddegon, G. X. Ding, C.-M. Ma, J. We, and T. R. Mackie, "BEAM - A Monte Carlo code to simulate radiotherapy treatment units," *Med. Phys.* 22:503–524 (1995).
53. F. A. Attix, *Introduction to Radiological Physics and Radiation Dosimetry*, (New York: Wiley) (1986).
54. D. W. O. Rogers, "Fluence to dose equivalent conversion factors calculated with EGS3 for electrons from 100 keV to 20 GeV and photons from 11 keV to 20 GeV," *Health Phys.* 46:891–914 (1984).
55. A. Ahnesjo, P. Andreo, and A. Brahme, "Calculation and application of point spread functions for treatment planning with high energy photon beams", *Acta Oncologica* 26:49–56 (1987).
56. N. Papanikolaou and T. R. Mackie, "Extension of the convolution/superposition based algorithms to include atomic number effects," *Med. Phys.* 22:977 (1995).
57. J. McLellan, L. Papiez, G. A. Sandison, W. Huda, and P. Therrien, "A numerical method for electron transport calculations", *Phys. Med. Biol.* 37:1109–25 (1992).
58. G. Starkschall, A. A. Shiu, S. W. Bujnowski, L. L. Wang, D. A. Low, and K. R. Hogstrom, "Effect of dimensionality of heterogeneity corrections on the implementation of a three-dimensional electron pencil-beam algorithm," *Phys. Med. Biol.* 36(2):207–227 (1991).
59. I. Kawrakow, M. Fippel, and K. Friedrich, "3D electron dose calculation using a voxel based monte carlo algorithm," *Med. Phys.* 23:445–457 (1996).
60. I. Kawrakow, "Accurate condensed history Monte Carlo simulation of electron transport. I. EGSnrc, the new EGS4 version," *Med. Phys.* 27:485–98 (2000).
61. M. K. Woo, D. Scora, and E. Webb, "The regional Monte Carlo method: a dose calculation method based on accuracy requirement," *Med. Phys.* 25:1866–1871 (1998).
62. I. Kawrakow, "Accurate condensed history Monte Carlo simulation of electron transport. II. Application to ion chamber response simulations," *Med. Phys.* 27:499–513 (2000).
63. I. Kawrakow, "VMC++, Electron and Photon Monte Carlo Calculations Optimized for Radiation Treatment Planning," in *Advanced Monte Carlo for Radiation Physics, Particle Transport Simulation and Applications*: *Proc. Monte Carlo 2000 Meeting* Lisbon, A. Kling, F. Barao, M. Nakagawa, L. Tavora, and P. Vaz (eds.), (Berlin: Springer), pp. 229–236 (2001).

64. H. Neuenschwander, T. R. Mackie, and P. Reckwerdt, "MMC-a high-performance Monte Carlo code for electron beam treatment planning," *Phys. Med. Biol.* 40(4):543–74 (1995).
65. M. Fippel, I. Kawrakow, K. Friedrich, "Electron beam dose calculations with the VMC algorithm and the verification data of the NCI working group," *Phys. Med. Biol.* 42:501–20 (1997).
66. C. Manfredotti, U. Nastasi, R. Marchisio, C. Ongaro, G. Gervino, R. Ragona, S. Anglesio and G. Sannazzari, "Monte Carlo simulation of dose distribution in electron beam radiotherapy treatment planning," *Nucl. Instrum. Methods* A291:646–54 (1990).
57. P. Keall and P. Hoban, "A review of electron beam dose calculation algorithms," *Australas. Phys. Eng. Sci. Med.* 19:111–30 (1996).
68. G. A. Carlsson, "Absorbed dose equations. on the derivation of a general absorbed dose equation and equations valid for different kinds, of radiation equilibrium," *Radiat. Res.* 85:219–237 (1981).
69. A. Dutreix and A. Bridier, "Dosimetry for External Beams of Photon and Electron Radiation" (Chapter 3) in *The Dosimetry of Ionizing Radiation,*" Kenneth R. Kase, Bengt Björngard, and Frank Attix (eds.), (San Diego: Academic Press Inc., Harcourt Brace Jovanovitch) V.1, pp. 163–228 (1985).
70. W. M. C. Roesch, "Dose for non electronic equilibrium conditions," *Radiat. Res.* 9:399–410 (1958).
71. R. Loevinger, "A formalism for calculation of absorbed dose to a medium from photon and electron beams," *Med. Phys.* 8:1–12 (1981).
72. T. R. Mackie, A. F. Bielajew, D. W. Rogers, and J. J. Battista, "Generation of photon energy deposition kernels using the EGS Monte Carlo code," *Phys. Med. Biol.* 33:1–20 (1988).
73. H. E. Johns, E. K. Darby, R. N. Haslam, L. Katz, and E. L. Harrington, "Depth dose data and isodose distributions for radiation from a 22 MeV betatron," *Am. J. Roentgenol.* 62:257–68 (1949).
74. J. Dutreix, A. Dutreix, and M. Tubiana, "Electronic equilibrium and transition stages." *Phys. Med. Biol.* 10:177–190 (1965).
75. J. Dutreix and M. Bernard, "Dosimetry at interfaces for high energy X and gamma rays," *Br. J. Radiol.* 39:205–210 (1966).
76. A. A. Mustafa and D. F. Jackson, "The relationship between x-ray CT numbers and charged particle stopping powers and its significance in radiotherapy treatment planning," *Phys. Med. Biol.* 28:169–76 (1983).
77. E. C. McCullough and A. M. Krueger, "Performance evaluation of computerized treatment planning systems for radiotherapy: external photon beams," *Int. J. Radiat. Oncol. Biol. Phys.* 6:1599–1605 (1980).
78. R. P. Parker, P. A. Hobday, and K. J. Cassell, "The direct use of CT numbers in radiotherapy dosage calculations for inhomogeneous media," *Phys. Med. Biol.* 24:802–809 (1979).
79. J. J. Battista, M. J. Bronskill, "Compton scatter imaging of transverse sections: an overall appraisal and evaluation for radiotherapy planning," *Phys. Med. Biol.* 26:81–99 (1981).
80. U. Fano, "Note on the Bragg-Gray cavity principle for measuring energy dissipation," *Radiat. Res.* 1:237–40 (1954).

81. A. Ahnesjo, M.-M. Aspradakis, "Dose calculations for external photon beams in radiotherapy" (Topical Review), *Phys. Med. Biol*. 44(11):99–155 (1999).
82. D. Harder, "Fano's theorem and the multiple scattering correction," *Fourth Symposium On Microdosimetry* (Verbania –Pallanza, Italy) J. Booz, H. G. Ebert, R. Eickel, and A. Waker (eds.) (Luxembourg: Commission of the European Communities), pp. 677–93 (1974).
83. M. Nilsson and T Knoos, "Application of the Fano theorem in inhomogeneous media using a convolution algorithm," *Phys. Med. Biol*. 37:69–83 (1992).
84. J. E. O'Connor, "The variation of scattered x-rays with density in an irradiated body," *Phys. Med. Biol*. 1:352–69 (1957).
85. P. J. Gullane, "Primary mandibular reconstruction: analysis of 64 cases and evaluation of interface radiation dosimetry on bridging plates," *Laryngoscope* 101:1–24 (1991).
86. B. E. Bjarngard, "On Fano's and O'Connor's theorems," *Radiat. Res*. 109:184–9 (1987).
87. M. B. Sharpe, A Unified Approach of Calculating the Dose Rate and Dose Distribution for Therapeutic X-Ray Beams," Ph.D. Thesis. University of Western Ontario, London, ON Canada.
88. ICRU Report No. 50, "Prescribing, Recording and Reporting Photon Beam Therapy," (Washington, DC: International Commission on Radiation Units and measurements) (1994).
89. C. X. Yu, J. W. Wong, and J. A. Purdy, "Photon dose perturbations due to small inhomogeneities," *Med. Phys*. 14:78–83 (1987).
90. B. L. Werner, I. J. Das, F. M. Khan, and A. S. Meigooni, "Dose perturbations at interfaces in photon beams," *Med. Phys*. 14:585–595 (1987).
91. B. L. Werner, I. J. Das, and W. N. Salk, "Dose perturbations at interfaces in photon beams: secondary electron transport," *Med. Phys*. 17:212–226 (1990).
92. K. M. Stenson, J. M. Balter, J. H. Campbell, and C. R. Carroll, "Effects of implantable biomaterials on radiation dosimetry," *Head and Neck* 19:384–390 (1997).
93. M. Tatcher, A. Kuten, J. Helman, and D. Laufer, "Perturbation of cobalt 60 radiation doses by metal objects implanted during oral and maxillofacial surgery," *J. Oral. Maxillofac. Surg*. 42(2):108–10 (1984).
94. M. K. Woo, J. R. Cunningham, and J. J. Jeziorenski, "Extending the concept of primary and scatter separation to the condition of electronic disequilibrium," *Med. Phys*. 17:588–595 (1990).
95. D. A. Jaffray, J. J. Battista, A. Fenster, and P. Munro, "X-ray sources of medical linear accelerators: focal and extra-focal radiation," *Med. Phys*. 20:1417–27 (1993).
96. M. B. Sharpe, D. A. Jaffray, J. J. Battista, P. Munro, "Extrafocal radiation: a unified approach to the prediction of beam penumbra and output factors for megavoltage x-ray beams," *Med. Phys*. 22:2065–2074 (1995).
97. A. Ahnesjo, "Analytic modeling of photon scatter from flattening filters in photon therapy beams," *Med. Phys*. 21:1227–35 (1994).
98. A. Dutreix, B. E. Bjarngard, A. Bridier, B. Mijnheer, J. E. Shaw, and H. Svensson, "Monitor Unit Calculation For High Energy Photon Beams," in *Physics for Clinical Radiotherapy Booklet No. 3*, European Society for Therapeutic Radiology and Oncology (ESTRO), ed. Garant Publishers N.V. (1997).

99. B. E. Bjarngard and P. L. Petti, "Description of the scatter component in photon-beam data," *Phys. Med. Biol.* 33:21–32 (1988).
100. M. K. Woo and J. R. Cunningham, "The validity of the density scaling method in primary electron transport for photon and electron beams," *Med. Phys.* 17:187–194 (1990).
101. R. Mohan and C.-S. Chui, "Validity of the concept of separating primary and scatter dose," *Med. Phys.* 12:726–30 (1985).
102. B. E. Bjarngard and J. R. Cunningham, "Comments on 'Validity of the concept of separating primary and scatter dose' (letter)," *Med. Phys.* 13:760–1 (1986).
103. J. C. Cunningham, "Scatter-air ratios," *Phys. Med. Biol.* 17:42-51 (1972).
104. A. Ahnesjo, "Cone Discretization for the Collapsed Cone Algorithm," in *International Conference on the Use of Computers in Radiation Therapy, XII ICCR*, Salt Lake City, Utah, D. D. Leavitt and G. Starkschall (eds.) (Madison, WI, Medical Physics Publishing) pp. 114–16 (1997).
105. A. Ahnesjo, "Collimator scatter in photon therapy beams," *Med. Phys.* 22:267–78 (1995).
106. A. Ahnesjo, "Collapsed cone convolution of radiant energy for photon dose calculation in heterogeneous media," *Med. Phys.* 16:577–92 (1989).
107. T. R. Mackie, J. W. Scrimger, and J. J. Battista, "A convolution method of calculating dose for 15-MV x rays," *Med. Phys.* 12:188–196 (1985).
108. R. Mohan, C.-S. Chui, and L. Lidofsky, "Differential pencil beam dose computation model for photons," *Med. Phys.* 13:64–73 (1986).
109. M. R. Sontag, Photon Beam Dose Calculations in Regions of Tissue Heterogeneity Using Computed Tomography, Ph.D. Thesis, University of Toronto, Toronto, ON Canada (1979).
110. J. J. Battista, M. B. Sharpe, "True three-dimensional dose computations for megavoltage x-ray therapy: a role for the superposition principle," *Australas. Phys. Eng. Sci. Med.* 15:159–78 (1992).
111. G. C. Field and J. J. Battista, "Photon Dose Calculations Using Convolution in Real and Fourier Space: Assumptions and Time Estimates," *Proceedings of the 9th International Conference on Computers in Radiation Therapy*, (New York, Elsevier) pp. 103–106 (1987).
112. J. R. Cunningham and L. Beaudoin, "Calculations for tissue inhomogeneities with experimental verification," *Proceedings of the XIII International Congress of Radiology*, Madrid, pp. 653–7 (1973).
113. J. E. O'Connor and D. E. Malone, "A cobalt-60 primary dose spread array derived from measurements," *Phys. Med. Biol.* 34:1029–42 (1989).
114. A. L. Boyer and E. C. Mok, "A photon dose distribution model employing convolution calculations," *Med. Phys.* 12:169–177 (1985).
115. J. W. Wong, R. M. Henkelman, A. Fenster, and H. E. Johns, "Second scatter contribution to dose in a cobalt-60 beam," *Med. Phys.* 8:755–782 (1981).
116. J. W. Wong and R. M. Henkelman, "A new approach to CT pixel-based photon dose calculations in heterogeneous media," *Med. Phys.* 10:199–208 (1983).
117. J. Van Dyk, R. B. Barnett, and J. Battista, "Computerized Radiation Treatment Planning Systems" in *The Modern Technology of Radiation Oncology: A Compendium for Medical Physicists and Radiation Oncologists*, J. Van Dyk (editor), (Madison, WI: Medical Physics Publishing) pp. 231–286 (1999).

118. J. R. Cunningham and J. J. Battista, "Calculation of dose distributions for x ray radiotherapy," *Physics in Canada* 41:190–195 (1995).
119. N. Papanikolaou and T. R. Mackie, "A new convolution approach for the generation of polyenergetic photon beam dose distributions," *Med. Phys*. 19 (1992).
120. J. J. Battista, M. B. Sharpe, E. Webb and J. Van Dyk, "A New Classification Scheme for Photon Beam Dose Algorithms," in *International Conference on the Use of Computers in Radiation Therapy, XII ICCR*, Salt Lake City, Utah, D. D. Leavitt and G. Starkschall (eds.) (Madison, WI, Medical Physics Publishing) pp. 39–42 (1997).
121. M.-M. Aspradakis, and A. T. Redpath, "A technique for the fast calculation of three-dimensional photon dose distributions using the superposition model," *Phys. Med. Biol*. 42:1475–89 (1997).
122. M. R. Sontag and S. K. Ray, "Determination of differential scatter-air ratios (dSAR) for three-dimensional scatter integration," *Med. Phys*. 22:775–80 (1995).
123. J. W. Wong and R. M. Henkelman, J. W. Andrew, J. Van Dyk, H. E. Johns, "Effect of small inhomogeneities on dose in a cobalt-60 beam," *Med. Phys.*, 8:783-791 (1981).
124. A. L. Boyer, "Shortening the calculation time of photon dose distributions in an inhomogeneous medium," *Med. Phys.* 11:552–554 (1984).
125. A. L. Boyer and E. C. Mok, "Calculation of photon dose distributions in an inhomogeneous medium using convolutions," *Med. Phys*. 13:503–509 (1986).
126. A. Ahnesjo and P. Andreo, "Determination of effective bremsstrahlung spectra and electron contamination for photon dose calculations," *Phys. Med. Biol*. 34:1451–64 (1989).
127. A. Ahnesjo, M. Saxner, and A. Trepp, "A pencil beam model for photon dose calculation," *Med. Phys.* 19:263–273 (1992).
128. M. Saxner and A. Ahnesjo, "Implementation of the collapsed cone method for clinical beam qualities," *Med. Phys.* 25, part 1, A185, (1998).
129. A. Ahnesjo and A. Trepp, "Acquisition of the effective lateral energy fluence distribution for photon beam dose calculations by convolution models," *Phys. Med. Biol.* 36:973–85 (1991).
130. R. Mohan and C.-S. Chui, "Use of fast Fourier transforms in calculating dose distributions for irregularly shaped fields for three dimensional treatment planning," *Med. Phys*. 14:70–77 (1987).
131. N. Papanikolaou and T. R. Mackie, "Generation of photon convolution kernels using a Monte Carlo code for use in radiotherapy treatment planning and cavity theory," *Med. Phys*. 20 (1993).
132. J. D. Bourland and E. L.Chaney, "A finite-size pencil beam model for photon dose calculations in three dimensions," *Med. Phys*. 19:1401–1412 (1992).
133. M. B. Sharpe and J. J. Battista, "Dose calculations using convolution and superposition principles: the orientation of dose spread kernels in divergent x-ray beams," *Med. Phys.* 20:1685–1694 (1993).
134. A. L. Boyer, Y. P. Zhu, L. Wang, and P. Francois, "Fast Fourier transform convolution calculations of x-ray isodose distributions in homogeneous media," *Med. Phys.* 16:248–253 (1989).
135. B. Lind, Radiation Therapy Planning and Optimization Studies as Inverse Problems, Ph.D. Thesis, Department of Radiation Physics, Stockholm Univeristy (1991).

136. T. R. Mackie, P. Reckwerdt, T. McNutt, M. Gehring, and C. Sanders, "Photon Beam Dose Computations," in T.R. Mackie, J.R. Palta (editors). *Teletherapy: Present and Future*. (Madison, WI:Advanced Medical Publishing) pp. 103–135 (1996).
137. Photon Treatment Planning Collaborative Working Group, M. Goitein, J. Laughlin, J. Purdy, M. R. Sontag, "Evaluation of high energy photon external beam treatment planning: project summary," *Int. J. Radiat. Oncol. Biol. Phys.* 21:3–8 (1991).
138. Photon Treatment Planning Collaborative Working Group, M. Goitein, J. Laughlin, J. Purdy, and M. R. Sontag, "Three-dimensional dose calculations for radiation treatment planning," *Int. J. Radiat. Oncol. Biol. Phys*. 21:25–36 (1991).
139. Photon Treatment Planning Collaborative Working Group, M. Goitein, J. Laughlin, J. Purdy, and M. R. Sontag, "Role of inhomogeneity corrections in three-dimensional photon treatment planning," *Int. J. Radiat. Oncol. Biol. Phys.* 21:59–69 (1991).
140. Photon Treatment Planning Collaborative Working Group, M. Goitein, J. Laughlin, J. Purdy, and M. R. Sontag, "The clinical three-dimensional treatment planning studies: A prologue," *Int. J. Radiat. Oncol. Biol. Phys*. 21:165–167 (1991).
141. G. J. Kutcher, Z. Fuks, H. Brenner, A. P. Brown, C. Burman, E. Cheng, L. Coia, K. Krippner, J. M. Manolis, R. Mohan, J. R. Simpson, M. Urie, B. Vikram, and R. Wallace, "Three-dimensional photon treatment planning for carcinoma of the nasopharynx," *Int. J. Radiat. Oncol. Biol. Phys.* 21:169–182 (1991).
142. J. R. Cunningham, "Tissue inhomogeneity corrections in photon beam treatment planning," in *Progress in Medical Radiation Physics*, Vol 1., C. G. Orton (ed.) pp. 103–131 (1982).
143. J. A. Purdy and S. C. Prasad, "Current Methods and Algorithms in Radiation Absorbed Dose Calculation and the Role of Computed Tomography: A Review" in *Computed Tomography in Radiation Therapy*," C. C. Ling, C. C. Rogers, and R. J. Morton (eds.) (New York: Raven Press) pp. 187–97 (1983).
144. R. Mohan, C.-S. Chui, D. Miller, and J. S. Laughlin, "Use of Computerized Tomography in Dose Calculations for Radiation Treatment Planning, CT," *J. Comput. Tomogr.* 5(3):273–282 (1981).
145. J. A. Purdy, J. W. Wong, W. B. Harms, B. Emami, and J. W. Matthews, "State of the art of high energy photon treatment planning," *Front. Radiat. Ther. Oncol.* 21:4–24 (1987).
146. J. W. Wong and J. A. Purdy, "On methods of inhomogeneity corrections for photon transport," [Review]. *Med. Phys.* 17:807–814 (1990).
147. J. W. Wong and J. A. Purdy, "Review of Methods of Inhomogeneity Corrections." in *Advances in Radiation Oncology Physics: Dosimetry, Treatment Planning and Brachytherapy* (New York: American Institute of Physics) pp. 887–99 (1992).
148. P. Bloch and M. D. Altschuler, "Three-Dimensional Photon Beam Calculations," in *Radiation Therapy Physics*, A. Smith (ed.) (Berlin: Springer) (1995).
149. J. Van Dyk, "Lung dose calculations using computerized tomography: Is there a need for pixel based procedures?" *Int. J. Radiat. Oncol. Biol. Phys*. 9:1035–1041 (1983).

150. J. R. Cunningham, "Current and future Development of Tissue Inhomogeneity Corrections for Photon Beam Clinical Dosimetry with the Use of CT," in *Computed Tomography in Radiation Therapy,"* C. C. Ling, C. C. Rogers, and R. J. Morton (eds.) (New York: Raven Press) pp. 209–18 (1983).
151. R. L. Siddon, "Fast calculation of the exact radiological path for a three-dimensional CT array," *Med. Phys.* 12:252–255 (1985).
152. M. R. Sontag and J. R. Cunningham, "Clinical application of a CT based treatment planning system," *Comput. Tomogr*. 2:117–30 (1978a).
153. M. R. Sontag, J. J. Battista, M. J. Bronskill, and J. R. Cunningham, "Implications of computed tomography for inhomogeneity corrections in photon beam dose calculations," *Radiology* 124:143–149 (1977).
154. P. W. Henson and R. A. Fox, "The electron density of bone for inhomogeneity correction in radiotherapy planning using CT numbers," *Phys. Med. Biol*. 29:351–359 (1984).
155. J.J. Battista, J. Van Dyk, and W.D. Rider, "Computed tomography for radiotherapy planning," *Int. J. Radiat. Oncol. Biol. Phys.* 6:99–107 (1980).
156. P. K. Kijewski and B. E. Bjarngard, "The use of computer tomography data for radiotherapy dose calculations," *Int. J. Radiat. Oncol. Biol. Phys*. 4:429–435 (1978).
157. H. Dahlin, I.-L. Lamm, T. Landberg, S. Levernes, and N. Ulsø, "User requirements on CT-based computed dose planning systems in radiation therapy," *Acta Radiol. Oncol*. 22:398–414 (1983).
158. G. D. Fullerton, W. Sewchand, J. T. Payne, S. H. Levitt, "CT determination of parameters for inhomogeneity corrections in radiation therapy of the esophagus," *Radiology* 126:167–171 (1978).
159. E. Glatstein, A. S. Lichter, B. A. Fraass, B. A. Kelly, and J. van de Geijn, "The imaging revolution and radiation oncology: use of CT, ultrasound, and NMR for localization treatment planning and treatment delivery," *Int. J. Radiat. Oncol. Biol. Phys*. 11:299–314 (1985).
160. R. L. Siddon, "Calculation of the radiological depth," *Med. Phys*. 12:84–87 (1985).
161. J. Van Dyk, T. J. Keane, and W. D. Rider, "Lung density as measured by computerized tomography: implications for radiotherapy," *Int. J. Radiat. Oncol. Biol. Phys*. 8:1363–72 (1982).
162. M. D. Altschuler, M. R. Sontag, and P. Bloch, "Three-dimensional dose calculations for photon beam therapy," *Med. Phys*. 10:529 (1983).
163. M. Tatcher and S. Palti, "Evaluation of density correction algorithms for photon-beam dose calculations," *Radiology* 141:201–205 (1981).
164. R. P. Parker, L. Contier de Freitas, K. J. Cassell, S. Webb, and P. A. Hobday, "A method of implementing inhomogeneity corrections in radiotherapy treatment planning: Comparison with experiment and Monte Carlo calculations," *J. Eur. Radiother.* 1(2):93–100 (1980).
165. M. Goitein and M. Abrams, "Multi-dimensional treatment planning: II. Beam's eye-view, back projection, and projection through CT sections," *Int. J. Radiat. Oncol. Biol. Phys*. 9:789–797 (1983).
166. E. C. McCullough and T. W. Holmes, "Acceptance testing computerized radiation therapy treatment planning systems: Direct utilization of CT scan data," *Med. Phys.* 12:237–242 (1985).

167. M. R. Sontag and J. R. Cunningham, “Corrections to absorbed dose calculations for tissue inhomogeneities”, *Med. Phys.* 4:431–436 (1977).
168. H. F. Batho, “Lung corrections in cobalt 60 beam therapy,” *J. Can. Assoc. Radiol.* 15:79–83 (1964).
169. M. E. Young and J. D. Gaylord, “Experimental tests of corrections for tissue inhomogeneities in radiotherapy,” *Br. J. Radiol.* 43(509):349–55 (1970).
170. S. Webb and R. A. Fox, “Verification by Monte Carlo methods of a power law tissue-air ratio algorithm for inhomogeneity corrections in photon beam dose calculations,” *Phys. Med. Biol.* 25:225–40 (1980).
171. R. L. Siddon, “Generalised Batho correction factor (radiotherapy dosimetry),” *Phys. Med. Biol.* 29:1575–1579 (1984).
172. K. J. Cassell, P. A. Hobday, and R. P. Parker, “The implementation of a generalized Batho inhomogeneity correction for radiotherapy planning with direct use of CT numbers,” *Phys. Med. Biol.* 26:825–33 (1981).
173. E. El-Khatib and J. J. Battista, “Improved lung dose calculation using tissue-maximum ratios in the Batho correction,” *Med. Phys.* 11:279–86 (1984).
174. K. Kappas and J.-C. Rosenwald, “Calcul des doses en radiotherapie en presence d’heterogeneites de petites dimensions,” *J. Eur. Radiother.* 6(1):35–45 (1985).
175. S. J. Thomas, “A modified power-law formula for inhomogeneity corrections in beams of high-energy x-rays,” *Med. Phys.* 18:719–23 (1991).
176. S. Chungbin, M. Gillin, and E. E. Klein, “Heterogeneity correction evaluation for RTOG Protocol 88-08,” *Med. Phys.* 21:923 (1994).
177. M. R. Arnfield, C. Hartmann Siantar, J. Siebers, P. Garmon, L. Cox, and R. Mohan, “The impact of electron transport on the accuracy of computed dose,” *Med. Phys.* 27:1266–1274 (2000).
178. J. Van Dyk, J. J. Battista, and W. D. Rider, “Half body radiotherapy: The use of computed tomography to determine the dose to the lung,” *Int. J. Radiat. Oncol. Biol. Phys.* 6:463–470 (1980).
179. J. Van Dyk, T. J. Keane, S. Kan, W. D. Rider, C. J. Fryer, “Radiation pneumonitis following large single dose irradiation: a re-evaluation based on absolute dose to lung,” *Int. J. Radiat. Oncol. Biol. Phys.* 7(4):461–7 (1981).
180. K. Yuen and R. O. Kornelsen, “Practical application of the differential Batho method for inhomogeneity correction on kerma in a photon beam,” *Med. Phys.* 15:74–77 (1988).
181. J. W. Wong and R. M. Henkelman, “Reconsideration of the power-law (Batho) equation for inhomogeneity corrections,” *Med. Phys.* 9:521–30 (1982).
182. C. Kappas and J.-C. Rosenwald, “Quality control of inhomogeneity correction algorithms used in treatment planning systems,” *Int. J. Radiat. Oncol. Biol. Phys.* 32:847–858 (1995).
183. K. Kappas and J.-C. Rosenwald, “A 3-D beam subtraction method for inhomogeneity correction in high energy X-ray radiotherapy,” *Radiother. Oncol.* 5:223–233 (1986).
184. L. M. Chin, C. W. Cheng, R. L. Siddon, R. K. Rice, B. J. Mijnheer, and J. R. Harris, “Three-dimensional photon dose distribution with and without lung corrections for tangential breast intact treatments,” *Int. J. Radiat. Oncol. Biol. Phys.* 17:1327–1335 (1991).

185. F. C. P. du Plessis, C. A. Willemse, M. G. Lötter, and L. Goedhals, "Comparison of the Batho, ETAR and Monte Carlo dose calculation methods in CT based patient models," *Med. Phys.* 28:582–589 (2001).
186. A. Iwasaki, "A method of taking into account the inhomogeneity backscatter contribution to the Batho correction factor," Scientific Note. *Phys. Med. Biol.* 31(8):923–926 (1986).
187. B. H. Shahine, M. S. A. L. Al-Ghazi, E. El-Khatib, "Experimental evaluation of interface doses in the presence of air cavities compared with treatment planning algorithms," *Med. Phys.* 26:350–355 (1999).
188. D. S. Shimm, K. P. Doppke, J. C. K. Leong, E. Gregory, and D. E. Dosoretz, "Variation in the lung inhomogeneity correction factor with beam energy," *Acta Radiol. Oncol.* 24(5):407–410 (1985).
189. W. Tang, F. M. Khan, and B. J. Gerbi, "Validity of lung correction algorithms," *Med. Phys.* 13:683–686 (1986).
190. E. Yorke, L. Harisiadis, B. Wessels, H. Aghdam, and R. Altemus, "Dosimetric considerations in radiation therapy of coin lesions of the lung," *Int. J. Radiat. Oncol. Biol. Phys.* 34(2):481–7 (1996).
191. B. A. Lulu and B. E. Bjarngard, "A derivation of Batho's correction factor for heterogeneities," *Med. Phys.* 9:907–909 (1982).
192. M. R. Sontag and J. R. Cunningham, "The equivalent tissue-air ratio method for making absorbed dose calculations in a heterogeneous medium," *Radiology* 129:787–794 (1978).
193. C. X. Yu and J. W. Wong, "Implementation of the ETAR method for 3D inhomogeneity corrections using FFT," *Med. Phys.* 20:627–632 (1993).
194. M. K. Martel, B. A. Fraass and D. L. McShan, "Study of limits of applicability of ETAR – Like inhomogeneity correction methods," *Med. Phys.* 19:785 (1992).
195. A. T. Redpath and D. I. Thwaites, "A 3-dimensional scatter correction algorithm for photon beams," *Phys. Med. Biol.* 36:779–98 (1991).
196. M. Engelsman, E. M.F. Damen, P. W. Koken, A. A. van `t Veld , K. M. van Ingen, and B. J. Mijnheer, "Impact of simple tissue inhomogeneity correction algorithms on conformal radiotherapy of lung tumours," *Radiother. Oncol.* 60:299–309 (2001).
197. T. P. Wong, W. K. Kan, and M. Law, "The effects of air cavities on X-ray dose distribution at 6 and 25 MV," *Australas. Phys. Eng. Sci. Med.* 19:237–47 (1996).
198. L. Beaudoin, "Analytical Approach to the Solution of the Dosimetry in Heterogeneous Media," M.Sc. Thesis, University of Toronto (1968).
199. K. Kappas and J.-C. Rosenwald, "Theoretical and experimental analysis of scatter from inhomogeneous slabs in a ^{60}Co beam: the differential tissue-air ratio method (DTAR)," *Phys. Med. Biol.* 31:1211–1228 (1986).
200. J. W. Wong, E. D. Slessinger, F. U. Rosenberger, K. Krippner, and J. A. Purdy, "The Delta-Volume Method for 3-Dimensional Photon Dose Calculations," in *Proceedings of the 8th International Conference on the Use of Computers in Radiation Therapy*. Toronto, Canada (Silver Spring, MD: Computer Society Press. IEEE) pp. 26–30 (1984).
201. K. Krippner, J. W. Wong, W. B. Harms, J. A. Purdy, "The Use of an Array Processor for the Delta-Volume Dose Computation Algorithm," in *Proceedings of the 9th International Conference on the Use of Computers in Radiation*

Therapy, Scheveningen, The Netherlands (North Holland, The Netherlands) pp. 533–536 (1987).
202. K. Kappas, "Les Heterogeneites dans les Faisceaux de Photons de Haute Energie Employes en Radiotherapie. Recherches Experimentales et Theoriques," Doctorat d' Etat, Univ. Paul Sabatier de Toulouse (Sciences), (1986).
203. M. J. Day, "The equivalent field method for axial dose determinations in rectangular fields," *Br. J. Radiol*. (*suppl 11*) 95–100 (1978).
204. N. Papanikolaou, T. R. Mackie, M. Gehring, and J. Fairbanks, "Clinical implementation of a convolution based algorithm for 3D treatment planning,",*Int. J. Radiat. Oncol. Biol. Phys*. 32, *Suppl. 1*, 302 (1995).
205. M. J. Butson, R. Elferink, T. Cheung, P.K. Yu, M. Stokes, K.Y. Quach, and P. Metcalfe, "Verification of lung dose in an anthropomorphic phantom calculated by the collapsed cone convolution method," *Phys. Med. Biol.* 45:43–9 (2000).
206. N. Papanikolaou, J. Erb, M. Gehring, C. Sanders, "Commissioning and Acceptance Testing of a Convolution based 3D RTP System," in *Medical & Biological Engineering & Computing*, V. 35, Suppl. Part 2, p. 994, Nice 1997, World Congress on Medical Physics 994, Nice (1997).
207. N. Papanikolaou and B. Heintz, "Speed and accuracy considerations for convolution algorithms in 3D treatment planning," *Med. Phys.* 23, (1996).
208. N. Papanikolaou, T. R. Mackie, and M. Gehring, "A Convolution Based Algorithm for Dose Computation in Radiation Therapy," in *Proceedings of the Roentgen Centennial International Congress*, Wurzburg-Germany (1995).
209. N. Papanikolaou, T. R. Mackie, C. Meger-Wells, M. Gehring, and P. Reckwerdt, "Investigation of the convolution method for polyenergetic spectra," *Med. Phys*. 20:1327–1336 (1993).
210. N. Papanikolaou and T. R. Mackie, "Separation of photon beam output factor into its phantom and machine generated components using a convolution code," *Med. Phys.* 21:877–878 (1994).
211. N. Papanikolaou and T. R. Mackie, "The extended phantom concept: modeling the treatment machine modifiers and portal imaging dosimetry system using a convolution code," *Med. Phys.* 21:877 (1994).
212. X. R. Zhu, D. A. Low, W. B. Harms, and J. A. Purdy, "A convolution-adapted ratio-TAR algorithm for 3D photon beam treatment planning," *Med. Phys*. 22:1315–1327 (1995).
213. T. Bortfeld, W. Schlegel, and B. Rhein, "Decomposition of pencil beam kernels for fast dose calculations in three-dimensional treatment planning," *Med. Phys.* 20:311–18 (1993).
214. O. Z. Ostapiak, Y. Zhu, and J. Van Dyk, "Refinements of the finite-size pencil beam model of three-dimensional photon dose calculation," *Med. Phys*. 24:743–750, (1997).
215. E. Wong, Y. Zhu, and J. Van Dyk, "Theoretical developments on Fast Fourier transform convolution dose calculations in inhomogeneous media," *Med. Phys.* 23:1511–1521 (1996).
216. E. Wong, J. Van Dyk and Y. Zhu, "Lateral electron transport in FFT photon dose calculations," *Med. Phys.* 24:1992–2000 (1997).
217. C. X. Yu, T. R. Mackie, and J. W. Wong, "Photon dose calculation incorporating explicit electron transport," *Med. Phys*. 22:1157–1165 (1995).

218. Y. Zhu and A. L. Boyer, "X-ray dose computations in heterogeneous media using 3-dimensional FFT convolution," *Phys. Med. Biol.* 35(3):351–368 (1990) (editorial).
219. Y. Zhu and J. Van Dyk, "Accuracy requirements of the primary x-ray spectrum in dose calculations using FFT convolution techniques," *Med. Phys*. 22:421–6 (1995).
220. M. Miften, M. Wiesmeyer, S. Monthofer, and K. Krippner, "Implementation of FFT convolution and multigrid superposition models in the FOCUS RTP system," *Phys. Med. Biol.* 45:817-33 (2000).
221. A. Iwasaki, "A method of calculating high-energy photon primary absorbed dose in water using forward and backward spread dose-distribution functions," *Med. Phys.* 12:731–7 (1985).
222. A. Iwasaki, "Calculation of three-dimensional photon primary absorbed dose using forward and backward spread dose-distribution functions," *Med. Phys*. 17:195–202 (1990).
223. A. Iwasaki and T. Ishito, "The differential scatter-air ratio and differential backscatter factor method combined with the density scaling theorem," *Med. Phys.* 11:755–63 (1984).
224. M. D. Altschuler, M. R. Sontag, and P. Block, "Rapid three dimensional treatment planning: I. Ray-tracing approach to primary component dose calculations," *Phys. Med. Biol.* 32:543–556 (1987).
225. N. Papanikolaou and T. R. Mackie, "A Convolution/Superposition Algorithm for Photon Beam Dose Computation," in *World Congress on Medical Physics*, Nice-V.35, Suppl. Part 2, p. 915 (1997).
226. T. R. Mackie, P. Reckwerdt, T. Holmes, N. Papanikolaou, and D. Simpkin, "The concept of secondary radiation equilibrium," *Med. Phys.* 19:785 (1992).
227. M. E. Young and R. O. Kornelsen, "Dose corrections for low-density tissue inhomogeneities and air channels for 10-MV X rays," *Med. Phys*. 10:450–455 (1983).
228. P. W. Hoban, "Accounting for the variation in kerma/terma ratio in photon beam convolution," *Med. Phys*. 22:2035–2044 (1995).
229. A. Ahnesjo and T. R. Mackie, "Analytical description of Monte Carlo generated photon dose convolution kernels," in *Int. Conference on the Use of Computers in Radiation Therapy, IX ICCR* (Scheveningen, The Netherlands), I. A. D. Bruinvis, P. H. van der Giessen, H. J. van Kleffens and F. W. Wittkamper (eds.) (Amsterdam: Elsevier) pp. 197–200 (1987).
230. A. Ahnesjo, "Dose Calculation Methods in Photon Beam Therapy Using Energy Deposition Kernels," Ph.D. Thesis, Department of Radiation Physics, Stockholm University (1991).
231. P. J. Reckwerdt and T. R. Mackie, "Superposition/convolution speed improvements using Run-Length Raytracing," *Med. Phys*. 19:784 (1992).
232. P. Andreo, "Monte Carlo techniques in medical radiation physics," [published erratum appears in *Phys. Med. Biol.* 1992 37(10):2031–2]. [Review] *Phys. Med. Biol.* 36:861–920 (1991).
233. D. W. O. Rogers and A. F. Bielajew, "Monte Carlo Techniques of Electron and Photon Transport for Radiation" in *The Dosimetry of Ionizing Radiation* vol 3, K. R. Kase, B. Bjarngard, and F. H. Attix (eds.) (New York: Academic) pp. 427–539 (1990).

234. T. R. Mackie, "Applications of the Monte Carlo Method in Radiotherapy," in *The Dosimetry of Ionizing Radiation*, vol 3, K. R. Kase, B. Bjarngard, and F. H. Attix (eds.) (New York: Academic) pp. 541–620 (1990).
235. D.W.O. Rogers, "Monte Carlo techniques in radiotherapy," *Phys. in Canada, Med. Phys*. Special Issue (2002).
236. P. Bloch, M. D. Altschuler, B. E. Bjärngar, A. Kassaee, and J. McDonough, "Determining clinical photon beam spectra from measured depth dose with the Cimmino algorithm," *Phys. Med. Biol.* 45(1):171–183 (2000).
237. C. L. Hartmann-Siantar, W. P. Chandler, M. B. Chadwick, et al, "Dose Distributions calculated with the PEREGRINE all-particle Monte Carlo Code," *Med. Phys*. 22:994–994 (1999).
238. A. Ahnesjo, L. Weber, and P. Nilsson, "Modeling transmission and scatter for photon beam attenuators," *Med. Phys.* 22:1711–1720 (1995).
239. O. A. Sauer and M. Neumann, "Reconstruction of high-energy bremsstrahlung spectra by numerical analysis of depth-dose data," *Radiother. Oncol.* 18:39–47 (1990).
240. B. R. Archer, P. R. Almond, and L. K. Wagner, "Application of a Laplace transform pair model for high-energy x-ray spectral reconstruction," *Med. Phys*. 12:630–3 (1985).
241. C. R. Baker and K. K. Peck, "Reconstruction of 6 MV photon spectra from measured transmission including maximum energy estimation," *Phys. Med. Biol*. 42:2041–2051 (1997).
242. P. H. Huang, K. R. Kase, and B. E. Bjarngard, "Reconstruction of 4-MV bremsstrahlung spectra from measured transimission data," *Med. Phys*. 10:778–785 (1983).
243. A. Piermattei, G. Arcovito, L. Azario, C. Bacci, L. Bianciardi, E. De Sapio, and C. Giacco, "A study of quality of bremsstrahlung spectra reconstructed from transmission measurements," *Med. Phys*. 17:227–233 (1991).
244. C. R. Baker, B. Amaee and N. M. Spyrou, "Reconstruction of megavoltage photon spectra by attenuation analysis," *Phys. Med. Biol*. 40:529–42 (1995).
245. P. Francois, F. Coste, J. Bonnet, and O. Caselles, "Validation of reconstructed bremsstrahlung spectra between 6 MV and 25 MV from measured transmission data," *Med. Phys*. 24:769–73 (1997).
246. A. Nisbet, H. Weatherburn, J. D. Fenwick, and G. McVey, "Spectral reconstruction of clinical megavoltage photon beams and the implications of spectral determination on the dosimetry of such beams," *Phys. Med. Biol*. 43:1507–21 (1998).
247. J. J. DeMarco, T. D. Solberg, and J. B. Smathers, "A CT-based Monte Carlo simulation tool for dosimetry planning and analysis," *Med. Phys*. 25:1–11 (1998).
248. D. M. Lovelock, C.-S. Chui and R. Mohan, "A Monte Carlo model of photon beams used in radiation therapy," *Med. Phys.* 22:1387–94 (1995).
249. H. H. Liu, T. R. Mackie, and E. C. McCullough, "A dual source photon beam model used in convolution/superposition dose calculation for clinical megavoltage x-ray beams," *Med. Phys*. 24:1960–74 (1997).
250. J. Sempau, S. J. Wilderman, and A. F. Bielajew, "DPM, a fast, accurate Monte Carlo code optimized for photon and electron radiotherapy treatment planning dose calculations," *Phys. Med. Biol*. 45:2263–2291 (2000).
251. C.-M. Ma, J. S. Li, T. Pawlicki, S. B. Jiang, J. Deng, "MCDOSE - A Monte Carlo dose calculation tool for radiation therapy treatment planning," in *Use of*

Computers in Radiotherapy, XIIIth Int. Conf., Heidelberg, W. Schlegel and T. Bortfeld (eds.) (Heidelberg: Springer-Verlag) pp. 123–125 (2000).
252. C.-M. Ma, J. S. Li, T. Pawlicki, S. B. Jiang, J. Deng, M. C. Lee, T. Koumrian, M. Luxton, and S. Brain, "A Monte Carlo dose calculation tool for radiotherapy treatment planning," *Phys. Med. Biol.* 47(10):1671–1689 (2002).
253. I. Kawrakow and M. Fippel, "Investigation of variance reduction techniques for Monte Carlo photon dose calculation using XVMC," *Phys. Med. Biol.* 45:2163–83 (2000).
254. C. L. Hartmann-Siantar, P. M. Bergstrom, W. P. Chandler, L. Chase, L. J. Cox, T. P. Daly, D. Garrett, S. M. Hornstein, R. K. House, E. I. Moses, R. W. Patterson, J. A. Rathkopf, and A. E. Schach von Wittenau, "Lawrence Livermore National Laboratory's PEREGRINE Projec" in *International Conference on the Use of Computers in Radiation Therapy, XII ICCR,* Salt Lake City, Utah, D. D. Leavitt and G. Starkschall (eds.) (Madison, WI: Medical Physics Publishing) pp. 19–22 (1997).
255. L. Wang, C.-S. Chui, and M. Lovelock, "A patient-specific Monte Carlo dose-calculation method for photons beams," *Med. Phys.* 25:867–78 (1998).
256. M. Bernard, "Etude de L'Ionisation au Voisinage des Interfaces Planes Situeés entre Deux Milieux de Nombres Atomiques Differents Soumis aux Rayons Gamma du Cobalt 60 et aux Rayons X d'un Betatron de 20 MV", Doctorat d'Etat, Univ. de Paris (1964) (in French).
257. A. F. Bielajew, D. W. O. Rogers, and A. E. Nahum, "The Monte Carlo simulation of ion chamber response to ^{60}Co-resolution of anomalies associated with interfaces," *Phys. Med. Biol.* 30(5):419–427 (1985).
258. A.F. Bielajew and D.W.O. Rogers, "PRESTA: The parameter reduced electron-step transport algorithm for electron Monte Carlo transport," *Nucl. Instrum. Methods Phys. Res. B, Beam Interact. Mater. At.* (Netherlands) B18, pp. 165–81 (1987).
259. X. A. Li, C. Yu, and T. Holmes, "A systematic evaluation of air cavity dose perturbation in megavoltage x-ray beams," *Med. Phys.* 27:1011–1017 (2000).
260. T. Haider and E. El-Khatib, "Differential scatter integration in regions of electronic non-equilibrium," *Phys. Med. Biol.* 40:31–43 (1995).
261. D. Hannallah, T. C. Zhu, and B. E. Bjarngard, "Electron disequilibrium in high-energy x-ray beams," *Med. Phys.* 23:1867–71 (1996).
262. T. C. Zhu and B. E. Bjarngard, "The fraction of photons undergoing head scatter in x-ray beams," *Phys. Med. Biol.* 40(6):1127–34 (1995).
263. O. A. Sauer, "Calculation of dose distributions in the vicinity of high-Z interfaces for photon beams," *Med. Phys.* 22:1685–90 (1995).
264. I. J. Das, K. R. Kase, A. S. Meigooni, F. M. Khan, and B. L. Werner, "Validity of transition-zone dosimetry at high atomic number interfaces in megavoltage photon beams," *Med. Phys.* 17:10–16 (1990).
265. W. K. Kan, P. M. Wu, H. T. Leung, T. C. Lo, C. W. Chung, D. L. Kwong, and S. T. Sham, "The effect of the nasopharyngeal air cavity on x-ray interface doses," *Phys. Med. Biol.* 43(3):529–37 (1998).
266. P. L. Petti, R. K. Rice, B. J. Mijnheer, L. M. Chin, and B.E. Bjarngard, "A heterogeneity model for photon beams incorporating electron transport," *Med. Phys.* 14:349–54 (1987).

267. P. L. Petti, R. L. Siddon, and B. E. Bjarngard, “A multiplicative correction factor for tissue heterogeneities,” *Phys. Med. Biol.* 31(10):1119–1128 (1986).
268. L. Wang, M. Lovelock, and C.-S. Chui, “Experimental verification of a CT-based Monte Carlo dose-calculation method in heterogeneous phantoms,” *Med. Phys*. 26:2626–2634 (1999).
269. S. Webb, “The absorbed dose in the vicinity of an interface between two media irradiated by a ^{60}Co source,” *Br. J. Radiol*. 52:962–967 (1979).
270. C.-M. Ma, E. Mok, A. Kapur, T. Pawlicki, D. Findley, S. Brain, K. Forster and A. L. Boyer, “Clinical implementation of a Monte Carlo treatment planning system,” *Med. Phys*. 26:2133–2143 (1999).
271. C.-M. Ma, T. Pawlicki, S. B. Jiang, J. S. Li, J. Deng, E. Mok, A. Kapur, L. Xing, L. Ma and A. L. Boyer, “Monte Carlo verification of IMRT dose distributions from a commercial treatment planning optimization system,” *Phys. Med. Biol*. 45:2483–2495 (2000).
272. L. Wang, E. Yorke, and C.-S. Chui, “Monte Carlo evaluation of tissue inhomogeneity effects in the treatment of the head and neck,” *Int. J. Radiat. Oncol. Biol. Phys.* 50:1339–1349 (2001).
273. M. Miften, M. Wiesmeyer, A. Kapur, and C.-M. Ma, “Comparison of RTP dose distributions in heterogeneous phantoms with the BEAM Monte Carlo simulation system,” *J. Appl. Clin. Med. Phys.* 2:21–31 (2001).
274. R. D. Lewis, S. J. Ryde, A. W. Seaby, D. A. Hancock, and C. J. Evans, “Use of Monte Carlo computation in benchmarking radiotherapy treatment planning system algorithms,” *Phys. Med. Biol.* 45:1755–64 (2000).
275. T. R. Mackie, E. El-Khatib, J. J. Battista, J. Scrimger, J. Van Dyk, and J. R. Cunningham, “Lung dose corrections for 6 MV and 15 MV x-rays,” *Med. Phys*. 12:327–332 (1985).
276. S. Webb and R. P. Parker, “A Monte Carlo study of the interaction of external beam X-radiation with inhomogeneous media,” *Phys. Med. Biol.* 23(6):1043–59 (1978).
277. M. E. Masterson, G. Barest, C.-S. Chui, K. P. Doppke, R. Epperson, W. Harms, K. Krippner, R. Mohan, E. Slessinger, M. R. Sontag, M. Urie, R. Wallace, W. Wong, “Interinstitutional experience in verification of external photon dose calculations,” *Int. J. Radiat. Oncol. Biol. Phys.* 21:37–58 (1991).
278. J. F. Briesmeister, ‘‘MCNP—A General Monte Carlo N-particle Transport Code, Version 4A,’’ Los Alamos National Laboratory report, LA-12625 (1993).
279. J. S. Hendricks and J. F. Briesmeister, ‘‘Recent MCNP Developments,’’ Los Alamos National Laboratory report, LA-UR-91-3456, 1992. 1128 (1996).
280. D. W. O. Rogers and A. F. Bielajew, “Calculated buildup curves for photons with energies up to ^{60}Co,” *Med. Phys.* 12:738–44 (1985).
281. D. W. Rogers and A. F. Bielajew, “Differences in electron depth-dose curves calculated with EGS and ETRAN and improved energy-range relationships,” *Med. Phys.* 13:687–94 (1986).
282. T. R. Mackie, “A Study of Charged Particles and Scattered Photons in Mega-Voltage X-Ray Beams,” Ph.D. Thesis, University of Alberta (1984).
283. BJR, “Central axis depth dose data for use in radiotherapy,” *Br. J. Radiol.* (*suppl 17*) (1983).

284. K. Ayyangar, J. R. Palta, J. W. Sweet, and N. Suntharalingam, “Experimental verification of a three-dimensional dose calculation algorithm using a specially designed heterogeneous phantom,” *Med. Phys.* 20(1):325–329 (1993).
285. D. Greene and J. G. Stewart, “Isodose curves in non-uniform phantoms,” *Br. J. Radiol.* 38:378–385 (1965).
286. D. R. White, “Tissue substitutes in experimental radiation physics,” *Med. Phys.* 5:467–479 (1978).
287. D. R. White, R. J. Martin, and R. Darlison, “Epoxy resin based tissue substitutes,” *Br. J. Radiol.* 50:814–821 (1977).
288. J. R. Butts and A. E. Foster, “Comparison of commercially available three-dimensional treatment planning algorithms for monitor unit calculations in the presence of heterogeneities,” *J. Appl. Clin. Med. Phys.* 2:32–41 (2001).
289. P. Dunscombe, P. McGhee, E. Lederer, “Anthropomorphic phantom measurements for the validation of a treatment planning system,” *Phys. Med. Biol.* 41:399–411 (1996).
290. B. Nilsson and P. O. Schnell, “Build-up effects at air cavities measured with thin thermoluminescent dosimeters,” *Acta Radiol. Ther. Phys. Biol.* 15(5):427–32 (1976).
291. M. D. Koskinen and E. Spring, “Build-up and build-down measurements with thin Lif-teflon dosimeters with special reference to radiotherapy of carcinoma of the larynx,” *Strahlenth.* 145:565 (1973).
292. C. Samuelsson, “Influence of air cavities on central depth dose curves for 33 MV roentgen rays,” *Acta Radiologica* 16(6):465–488 (1977).
293. P. M. Ostwald, T. Kron, and C. S. Hamilton, “Assessment of mucosal underdosing in larynx irradiation,” *Int. J. Radiat. Oncol. Biol. Phys.* 36(1):181–187 (1996).
294. E. E. Klein, L. M. Chin, R. K. Rice, B. J. Mijnheer, “The influence of air cavities on interface doses for photon beams,” *Int. J. Radiat. Biol. Phys.* 27:419–427 (1993).
295. J. L. Beach, M. S. Mendiondo, and O. A. Mendiondo, “A comparison of air-cavity inhomogeneity effects for cobalt-60, 6-, and 10- x-ray beams,” *Med. Phys.* 14:140–144 (1987).
296. A. Niroomand-Rad, K. W. Harter, S. Thobejane, and K. Bertrand, “Air cavity effects on the radiation dose to the larynx using Co-60, 6 MV, and 10 MV photon beams,” *Int. J. Radiat. Oncol. Biol. Phys.* 29(5):1139–1146 (1994).
297. P. Francescon, C. Cavedon, S. Reccanello, S. Cora, “Photon dose calculation of a three-dimensional treatment planning system compared to the Monte Carlo code BEAM,” *Med. Phys.* 27:1579–87 (2000).
298. E. R. Epp, A. L. Boyer, and K. P. Doppke, “Underdosing of lesions resulting from lack of electronic equilibrium in upper respiratory air cavities irradiated by 10 MV x-ray beams,” *Int. J. Radiat. Oncol. Biol. Phys.* 2:613–619 (1977).
299. E. R. Epp, M. N. Lougheed, and J. W. McKay, “Ionization buildup in upper air passages during teletherapy with cobalt-60 radiation,” *Br. J. Radiol.* 31:361–367 (1958).
300. T. P. Wong, P. E. Metcalfe, T. Kron, and T. G. Emeleus, “Radiotherapy x-ray dose distribution beyond air cavities,” *Australas. Phys. Eng. Sci. Med.* 15(3):138–46 (1992).

301. C. Hurkmans, T. Knoos, P. Nilsson, G. Svahn-Tapper, and H. Danielsson, "Limitations of a pencil beam approach to photon dose calculations in the head and neck region," *Radiother. Oncol.* 37:74–80 (1995).
302. L. Coia, J. Galvin, M. R. Sontag, P. Blitzer, H. Brenner, E. Cheng, K. Doppke, W. Harms, M. Hunt, R. Mohan, and J. J. Munzenrider Simpson, "Three-dimensional photon treatment planning in carcinoma of the larynx," *Int. J. Radiat. Oncol. Biol. Phys.* 21:183–192 (1991).
303. I. Izuno, S. Sone, M. Oguchi, K. Kiyons, and K. Takei, "Treatment of early vocal cord carcinoma with ^{60}Co gamma rays, 8/10 MV X-rays, or 4 MV X-rays: Are the results different?" *Acta Oncol.* 29:637–639 (1990).
304. G. L. Jiang, K. K. Ang, L. J. Peters, C. D. Wendt, M. J. Oswald, and H. Goephert, "Maxillary sinus carcinomas: Natural history and results of postoperative radiotherapy," *Radiother. Oncol.* 21:193–200 (1991).
305. J. van de Geijn, "The extended net fractional depth dose: Correction for inhomogeneities, including effects of electron transport in photon beam dose calculation," *Med. Phys.* 14:84–92 (1987).
306. R. K. Rice, B. J. Mijnheer, L. M. Chin, "Benchmark measurements for lung dose corrections for x-ray beams," *Int. J. Radiat. Oncol. Biol. Phys.* 15:399–409 (1988).
307. E. El-Khatib and J. J. Battista, "Accuracy of lung dose calculations for large-field irradiation with 6-MV x rays," *Med. Phys.* 13:111–116 (1986).
308. J. E. O'Connor and D. E. Malone, "An equivalent shape approximation for photon doses in lung," *Phys. Med. Biol.* 35(2):223–234 (1990).
309. P. E. Metcalfe, T. P. Wong, and P. W. Hoban, "Radiotherapy x-ray beam inhomogeneity corrections: the problem of lateral electronic disequilibrium in lung," *Australas. Phys. Eng. Sci. Med.* 16:155–167 (1993).
310. P. W. Hoban, D. C. Murray, P. E. Metcalfe, and W. H. Round, "Superposition dose calculation in lung for 10 MV photons," *Australas. Phys. Eng. Sci. Med.* 13:81–92 (1990).
311. R. Mayer, A. Williams, T. Frankel, Y. Cong, S. Simons, N. Yang, R. Timmerman, "Two-dimensional film dosimetry application in heterogeneous materials exposed to megavoltage photon beams," *Med. Phys.* 24:455–460 (1997).
312. R. K. Rice, J. L. Hansen, L. M. Chin, B. J. Mijnheer, and B.E. Bjarngard, "The influence of ionization chamber and phantom design on the measurement of lung dose in photon beams," *Med. Phys.* 15:884–890 (1988).
313. E. E. Klein, A. Morrison, J. A. Purdy, M. V. Graham, and J. Matthews, "A volumetric study of measurements and calculations of lung density corrections for 6 MV and 18 MV photons," *Int. J. Radiat. Oncol. Biol. Phys.* 37:1163–1170 (1997).
314. M. Blomquist and M. Karlsson, "Measured lung dose correction factors for 50 MV photons," *Phys. Med. Biol.* 43:3225–3234 (1998).
315. P. J. White, R. D. Zwicker, and D. T. Haung, "Comparison of dose homogeneity effects due to electron equilibrium loss in lung for 6 MV and 18 MV photons," *Int. J. Radiat. Oncol. Biol. Phys.* 34:1141–1146 (1996).
316. M. Essers, J. H. Lanson, G. Leunens, T. Schnabel, and B. J. Mijnheer, "The accuracy of CT-based inhomogeneity corrections and *in vivo* dosimetry for the treatment of lung cancer," *Radiother. Oncol.* 37(3):199–208 (1995).

317. R. C. Miller, J. A. Bonner, and R. W. Kline, “Impact of beam energy and field margin on penumbra at lung tumor-lung parenchyma interfaces,” *Int. J. Radiat. Oncol. Biol. Phys.* 41:707–713 (1998).
318. L. Wang, E. Yorke, G. Desobry, and C.-S. Chui, “Dosimetric advantage of using 6 MV over 15 MV photons in conformal therapy of lung cancer: Monte Carlo studies in patient geometries,” *J. Appl. Clin. Med. Phys.* 3:51–59 (2002).
319. Radiation Therapy Oncology Group, “Prospective randomized trial of postoperative adjuvant therapy in patients with completely resected stage II and stage IIIa nonsmall cell lung caner,” RTOG 91-05 Revised Edition, August 24 (1992).
320. S. B. Easterling, N. Papanikolaou, and A. Meigooni, “Quantitative analysis of dose in an anthropomorphic lung phantom using thermoluminescent dosimetry, convolution algorithm, and radiochromic film,” *Med. Phys.* 23:1114–1115 (1996).
321. E. E. Klein, J. Gibbons, Z. Li, S. Chungbin, and C. Orton, “Benchmark measurements for lung corrections for energies ranging from Co-60 to 24 MV,” *Med. Phys.* 21:945 (1994).
322. S. L. S. Kwa, J. C. M. Theuws, A. Wagenaar, E. F. M. Damen, L. J. Boersma, P. Baas, S. H. Muller, and J. V. Lebesque, “Evaluation of two dose-volume histogram reduction models for the prediction of radiation pneumonitis,” *Radiother. Oncol.* 48:61–69 (1998).
323. A. Aref, D. Thornton, E. Youssef, T. He, S. Tekyi-Mensah, L. Denton, and G. Ezzell, “Dosimetric improvements following 3D planning of tangential breast irradiation,” *Int. J. Radiat. Oncol. Biol. Phys.* 48:1569–1574 (2000).
324. A. Fogliata, A. Bolsi, and L. Cozzi, “Critical appraisal of treatment techniques based on conventional photon beams, intensity modulated photon beams and proton beams for therapy of intact breast,”,*Radiother. Oncol.* 62(2):137–145 (2002).
325. C. W. Hurkmans, B. C. J. Cho, E. Damen, L. Zijp, and B. J. Mijnheer, “Reduction of cardiac and lung complication probabilities after breast irradiation using conformal radiotherapy with or without intensity modulation,” *Radiother. Oncol.* 62(2):163–171 (2002).
326. L. A. Farraday, G. T. Doswell, “Treatment planning for the breast patient: with or without lung correction?” *Med. Dosim.* 17:1–9 (1992).
327. M. M. Ellen, K. R. Hogstrom, L. A. Miller, R. C. Erice, T. A. Buchholz, “A comparison of 18-MV and 6-MV treatment plans using 3D dose calculation with and without heterogeneity correction,” *Med. Dosim.* 24:287–94 (1999).
328 .B. J. Mijnheer, S. Heukelom, J. H. Lanson, L. J. van Battum, N. A. van Bree, and G. van Tienhoven, “Should inhomogeneity corrections be applied during treatment planning of tangential breast irradiation?” *Radiother. Oncol.* 22:239–44 (1991).
329. C. L. Creutzberg, V. G. M. Althof, H. Huizenga, A. G. Visser, and P. C. Levandag, “Quality assurance using portal imaging – the accuracy of the patient positioning in irradiation of breast cancer,” *Int. J. Radiat. Oncol. Biol. Phys.* 25:529–539 (1993).
330. B. K. Lind, P. Kallman, B. Sundelin, and A. Brahme, “Optimal radiation beam profiles considering uncertainties in beam patient alignment,” *Acta Oncol.* 32:331–42 (1993).

331 .C. Mitine, A. Dutreix, E. Vanderschueren, "Tangential breast irradiation – influence of technique of set-up on transfer errors and reproducibility," *Radiother. Oncol.* 22:308–310 (1991).
332. A. Bel, M. Vanherk, H. Bartelink, and J. V. Lebesque, "A verification procedure to improve patient set-up accuracy using portal images," *Radiother. Oncol.* 29:253–260 (1993).
333. H. D. Kubo, B. C. Hill, "Respiration gated radiotherapy treatment: a technical study," *Phys. Med. Biol.* 41:83–91 (1996).
334. A. E. Lujan, E. W. Larsen, J. M. Balter, and R. K. Ten Haken, "A method for incorporating organ motion due to breathing into 3D dose calculations," *Med. Phys.* 26:715–720 (1999).
335. J. M. Balter, R. K. Ten Haken, T. S. Lawrence, K. L. Lam, and J. M. Robertson, "Uncertainties in CT-based radiation therapy treatment planning associated with patient breathing," *Int. J. Radiat. Oncol. Biol. Phys.* 36:167–174 (1996).
336. K. E. Rosenzweig, J. Hanley, D. Mah, G. Mageras, M. Hunt, S.Toner, C. Burman, C. C. Ling, B. Mychalczak, Z. Fuks, and S. A. Leibel, "The deep inspiration breath-hold technique in the treatment of inoperable non-small-cell lung cancer," *Int. J. Radiat. Oncol. Biol. Phys.* 48:81–87 (2000).
337. J. Hanley, M. M. Debois, D. Mah, G. S. Mageras, A. Raben, K. Rosenzweig, B. Mychalczak, L. H. Schwartz, P. J. Gloeggler, W. Lutz, C. C. Ling, S. A Leibel, Z. Fuks, and G. J. Kutcher, "Deep inspiration breath-hold technique for lung tumors: The potential value of target immobilization and reduced lung density in dose escalation," *Int. J. Radiat. Oncol. Biol. Phys.* 45:603–611 (1999).
338. G. Mageras, "Respiratory Motion-Induced Treatment Uncertainties," in *Medical Physics*, C. Kappas, A. del Guerra, Z. Kolitsi, Y. Damilakis, K. Theodorou (eds.) (Bologna: Monduzzi Editore) pp. 33–8 (1999).
339. M. Engelsman, P. Remeijer, M. van Herk, J. V. Lebesque, B. J. Mijnheer, E. M. F. Damen, "Field size reduction enables ISO-NTCP escalation of tumor control probability for irradiation of lung tumors," *Int. J. Radiat. Oncol. Biol. Phys.* 51:1290–1298 (2001).
340. P. Mavroidis, S. Axelsson, S. Hyodynmaa, J. Rajala, M. A. Pitkanen, B. K. Lind, and A. Brahme, "Effects of positioning uncertainty and breathing on dose delivery and radiation pneumonitis prediction in breast cancer," *Acta Oncol.* 41(5):471–85 (2002), Erratum in *Acta Oncol.* 42(3):255 (2003).
341. W. Spiers, "The influence of energy absorption and electron range on dosage in irradiated bone," *Br. J. Radiol.* 22:521–533 (1949).
342. W. Spiers, "Dosage in irradiated soft tissue and bone," *Br. J. Radiol.* 25:365–370 (1951).
343. W. K. Sinclair, "The relative biological effectiveness of 22-MV x-rays, cobalt-60 gamma rays, and 200-kVp x-rays. Absorbed dose to the bone marrow in the rat and the mouse," *Radiat. Res.* 16:369–383 (1962).
344. N. Aspin and H. E. Johns, "The absorbed dose in cylindrical cavities within irradiated bone," *Br. J. Radiol.* 36(425):350–362 (1963).
345. I. J. Das. "Study of Dose Perturbation at Bone-Tissue Interfaces in Megavoltage Photon Beam Therapy," Ph.D. Thesis, University of Minnesota, 1988.
346. C. S. Reft and F. T. Kuchnir, "Dose Correction Factors at Bone-Tissue Surface for High Energy Photon Beams," Presented at annual AAPM meeting (1986).

347. B. J. Mijnheer, R. K. Rice, and L. M. Chin, “Lead polystyrene transition zone dosimetry in high energy photon beams,” *Radiol. Oncol.* 11:379–386 (1988).
348. I. J. Das and F. M. Khan, “Backscatter dose perturbation at high atomic number interfaces in megavoltage photon beams,” *Med. Phys.* 16:367–375 (1989).
349. I. J. Das, F. M. Khan, and B. J. Gerbi, “Interface dose perturbation as a measure of megavoltage photon beam energy,” *Med. Phys*. 15:78–81 (1988).
350. B. L. Werner, “Dose perturbations at interfaces in photon beams: Annihilation radiation,” *Med. Phys*. 18:713–718 (1991).
351. S. W. Jacob, P. Gullane, D. Galbraith, and B. Cummings, “Implications of radiation dose distribution at mandibular prosthesis/tissue interface,” Internal Report. OCI/PMH (1985).
352. M. Farahani, F. C. Eichmiller, W. L. McLaughlin, “Measurement of absorbed doses near metal and dental material interfaces irradiated by x- and gamma-ray therapy beams,” *Phys. Med. Biol*. 35:369–85 (1990).
353. R. Nadrowitz, T. Feyerabend, “Backscatter dose from metallic materials due to obliquely incident high-energy photon beams,” *Med. Phys*. 28(6):959–65 (2001).
354. X. A. Li, J. C. Chu, W. Chen, T. Zusag, “Dose enhancement by a thin foil of high-Z material: a Monte Carlo study,” *Med. Phys.* 26:1245–51 (1999).
355. M. B. Hazuka, D. N. Stroud, J. Adams, G. S. Ibbott, and J. J. Kinzie, “Prostatic thermoluminescent dosimeter analysis in a patient treated with 18 MV X rays through a prosthetic hip,” *Int. J. Radiat. Oncol. Biol. Phys*. 25(2):339–343 (1993).
356. E. E. Klein and R. R. Kuske, “Changes in photon dose distributions due to breast prostheses,” *Int. J. Radiat. Oncol. Biol. Phys.* 25:541–549 (1993).
357. A. Niroomand-Rad, R. Razavi, S. Thobejane, and K.W. Harter, “Radiation dose perturbation at tissue-titanium dental interfaces in head and neck cancer patients,” *Int. J. Radiat. Oncol. Biol. Phys.* 34:475–80 (1996).
358. G. X. Ding and C. W. Yu, “A study on beams passing through hip prosthesis for pelvic radiation treatment,” *Int. J. Radiat. Oncol. Biol. Phys*. 51:1167–75 (2001).
359. R. Wang, K. Pillai, and P. K. Jones, “Dosimetric measurement of scattered radiation from dental implants in simulated head and neck radiotherapy,” *Int. J. Oral Maxillofac. Implants* 13:197–203 (1998).
360. T. A. Mian, M. C. Jr. Van Putten, D. C. Kramer, R. F. Jacob, and A. L. Boyer, “Backscatter radiation at bone-titanium interface from high-energy X and gamma rays,” *Int. J. Radiat. Oncol. Biol. Phys.* 13:1943–7 (1987).
361. F. A. Gibbs, B. Palos, and D. R. Goffinet, “The metal/tissue interface effect in irradiation of the oral cavity,” *Radiology* 119:705–7 (1976).
362. D. L. Zellmer, J. D. Chapman, C. C. Stobbe, F. Xu, and I. J. Das, “Radiation fields backscattered from material interfaces. I. Biological effectiveness,” *Radiat. Res*. 150:406–15 (1998).
363. D. L. Newman, G. Dougherty, A. Al Obaid, and H. Al Hajrasy, “Limitations of CT in assessing cortical thickness and density,” *Phys. Med. Biol*. 43:619–626 (1998).
364. R. A. Geise and E.C. McCullough, “The use of CT scanners in megavoltage photon beam therapy planning,” *Radiology* 124:133–141 (1977).
365. D. Verellen, V. Vinh-Hung, P. Bijdekerke, F. Nijs, N. Linthout, A. Bel, and G. Storme, “Characteristics and clinical application of a treatment simulator with CT option,” *Radiother. Oncol.* 50:355–366 (1999).

366. J. C. H. Chu, B. Ni, R. Kriz, and V. A. Saxena, "Applications of simulator computed tomography number for photon dose calculations during radiotherapy treatment planning," *Radiother. Oncol*. 55:65–73 (2000).
367. M. A. Mosleh-Shirazi, P. M. Evans, W. Swindell, S. Webb, M. Partridgem, "A cone-beam megavoltage CT scanner for treatment verification in conformal radiotherapy," *Radiother. Oncol*. 48:319–328 (1998).
368. U. Schneideryx, E. Pedroniz, and A. Lomaxz, "The calibration of CT Hounsfield units for radiotherapy treatment planning," *Phys. Med. Biol*. 41:111–124 (1996).
369. W. Kilby, J. Sage, and V. Rabett, "Tolerance levels for quality assurance of electron density values generated from CT in radiotherapy treatment planning," *Phys. Med. Biol*. 47:1485–1492 (2002).
370. H. Guan, F.-F. Yin, and J. H. Kim, "Accuracy of inhomogeneity correction in photon radiotherapy from CT scans with different settings," *Phys. Med. Biol*. 47:N223-N231 (2002).
371. Task Group 40.
372. K. Rustgi, M. A. Samuels, and S. N. Rustgi, "Influence of air inhomogeneities in radiosurgical beams," *Med. Dosim*. 22(2):95–100 (1997).
373. S. N. Rustgi, A. K. Rustgi, S. B Jiang, and K. M. Ayyangar, "Dose perturbation caused by high-density inhomogeneities in small beams in stereotactic radiosurgery," *Phys. Med. Biol*. 43:3509–3518 (1998).
374. K. Theodorou, S. Stathakis, B. Lind, A. Liander, C. Kappas, "Study of the Perturbation of Dose distribution for Linac and Gamma Knife Stereotactic Radiotherapy due to Head Heterogeneities," Proceed. 19th Annual ESTRO Meeting, Istanbul, Turkey, Sept. 2000.
375. T. D. Solberg, F. E. Holly, A. A. F. De Salles, R. E. Wallace, and J. B. Smathers, "Implications of tissue heterogeneity for radiosurgery in head and neck tumors," *Int. J. Radiat. Oncol. Biol. Phys*. 32:235–239 (1995).
376. K. M. Ayyangar and S. B. Jiang, "Do we need Monte Carlo treatment planning for linac based radiosurgery? A case study," *Med. Dosim*. 23:161–167 (1998).
377. M. Blomquist, J. Li, C.-M. Ma, B. Zackrisson, and M. Karlsson, "Comparison between a conventional treatment energy and 50 MV photons for the treatment of lung tumours," *Phys. Med. Biol*. 47:889–897 (2002).
378. R. Mohan and P. P. Antich, "A method of correction for curvature and inhomogeneities in computer aided calculation of external beam radiation dose distributions," *Comput. Progr. Biomed*. 9:247–257 (1979).
379. R. Mohan, G. Barest, L. J. Brewster, et al. "A comprehensive three-dimensional radiation treatment planning system," *Int. J. Radiat. Oncol. Biol. Phys*. 15:481–495 (1988).
380. W. R. Nelson, H. Hirayama, and D. W. O. Rogers. The EGS4 code system. Stanford, CA: Stanford Linear Accelerator Center; 1985.
381. C. Constantinou, "Phantom materials for radiation dosimetry. I. Liquids and gels," *Br. J. Radiol*. 55(651):217–24 (1982).
382. C. Constantinou, F. H. Attix, and B. R. Paliwal, "A solid water phantom material for radiotherapy x-ray and gamma-ray beam calibrations," *Med. Phys*. 9:436–41 (1982).
383. E. El-Khatib, M. Evans, M. Pla, and J. R. Cunningham, "Evaluation of lung dose correction methods for photon irradiations of thorax phantoms," *Int. J. Radiat. Oncol. Biol. Phys*. 17:871–878 (1989).

384. B. Fraass, K. P. Doppke, M. Hunt, G. Kutcher, G. Starkschall, R. Stern, and J. Van Dyk, "American Association of Physicists in Medicine Radiation Therapy Committee Task Group 53: Quality assurance for clinical radiotherapy treatment planning," *Med. Phys.* 25:1773–829 (1998).
385. American Association of Physicists in Medicine, Radiation therapy Committee Task Group 21, "A protocol for the determination of absorbed dose from high-energy photon and electron beams," *Med. Phys.* 10:741–771 (1983).
386. T. Mauceri and K. Kase, "Effects of ionization chamber construction on dose measurements in a heterogeneity," *Med. Phys.* 14:653–656 (1987).
387. N. Papanikolaou, "Dose calculation algorihtms in the IMRT era," *Radiother. Oncol.* 61 (Suppl. 1):S12 (2001).
388. N. Papanikolaou, Y. Tsougos, and C. Kappas, "The effect of tissue inhomogeneities in IMRT," Proceed. 44th Annual Meeting ASTRO *Med. Phys.* 28(7) (2001).
389. N. Papanikolaou, J. Penagaricano, and V. Ratanatharathorn, "The effect of lung inhomogeneity in IMRT," *Int. J. Radiat. Oncol. Biol. Phys.* 50(Suppl. 1):302 (2001).
390. R. Jeraj and P. Keall, "The effect of statistical uncertainty on inverse treatment planning based on Monte Carlo dose calculation," *Phys. Med. Biol.* 45:3601–3613 (2000).
391. R. Jeraj, P. J. Keall, and J. V. Siebers, "The effect of dose calculation accuracy on inverse treatment planning," *Phys. Med. Biol.* 47:391–407 (2002).
392. P. J. Keall, J. V. Siebers, R. Jeraj, and R. Mohan, "The effect of dose calculation uncertainty on the evaluation of radiotherapy plans," *Med. Phys.* 27:478–84 (2000).
393. E. K. Butker, D. J. Helton, J. W. Keller, L. L. Hughes, T. Crenshaw, and L. W. Davis, "A totally integrated simulation technique for three-field breast treatment using a CT simulator," *Med. Phys.* 23:1809–14 (1996).

AAPM REPORT SERIES

No. 1 "Phantoms for Performance Evaluation and Quality Assurance of CT Scanners" (1977)
No. 3 "Optical Radiations in Medicine: A Survey of Uses, Measurement and Sources" (1977)
No. 4 "Basic Quality Control in Diagnostic Radiology," AAPM Task Force on Quality Assurance Protocol (1977)
No. 5 "AAPM Survey of Medical Physics Training Programs," Committee on the Training of Medical Physicists (1980)
No. 6 "Scintillation Camera Acceptance Testing & Performance Evaluation," AAPM Nuclear Medicine Committee (1980)
No. 7 "Protocol for Neutron Beam Dosimetry," AAPM Task Group #18 (1980)
No. 8 "Pulse Echo Ultrasound Imaging Systems: Performance Tests & Criteria," P. Carson & J. Zagzebski (1980)
No. 9 "Computer-Aided Scintillation Camera Acceptance Testing," AAPM Task Group of the Nuclear Medicine Committee (1982)
No. 10 "A Standard Format for Digital Image Exchange," Baxter et al. (1982)
No. 11 "A Guide to the Teaching of Clinical Radiological Physics to Residents in Radiology," AAPM Committee on the Training of Radiologists (1982)
No. 12 "Evaluation of Radiation Exposure Levels in Cine Cardiac Catherization Laboratories," AAPM Cine Task Force of the Diagnostic Radiology Committee (1984)
No. 13 "Physical Aspects of Quality Assurance in Radiation Therapy," AAPM Radiation Therapy Committee Task Group #24, with contribution by Task Group #22 (1984)
No. 14 "Performance Specifications and Acceptance Testing for X-Ray Generators and Automatic Exposure Control Devices" (1985)
No. 15 "Performance Evaluation and Quality Assurance in Digital Subtraction Angiography," AAPM Digital Radiology/ Fluorography Task Group (1985)
No. 16 "Protocol for Heavy Charged-Particle Therapy Beam Dosimetry," AAPM Task Group #20 of the Radiation Therapy Committee (1986)
No. 17 "The Physical Aspects of Total and Half Body Photon Irradiation," AAPM Task Group #29 of the Radiation Therapy Committee (1986)
No. 18 "A Primer on Low-Level Ionizing Radiation and its Biological Effects," AAPM Biological Effects Committee (1986)
No. 19 "Neutron Measurements Around High Energy X-Ray Radiotherapy Machines," AAPM Radiation Therapy Task Group #27 (1987)
No. 20 "Site Planning for Magnetic Resonance Imaging Systems," AAPM NMR Task Group #2 (1987)
No. 21 "Specification of Brachytherapy Source Strength," AAPM Radiation Therapy Task Group #32 (1987)
No. 22 "Rotation Scintillation Camera Spect Acceptance Testing and Quality Control," Task Group of Nuclear Medicine Committee (1987)
No. 23 "Total Skin Electron Therapy: Technique and Dosimetry," AAPM Radiation Therapy Task Group #30 (1988)
No. 24 "Radiotherapy Portal Imaging Quality," AAPM Radiation Therapy Task Group #28 (1988)

No. 25 "Protocols for the Radiation Safety Surveys of Diagnostic Radiological Equipment," AAPM Diagnostic X-Ray Imaging Committee Task Group #1 (1988)

No. 26 "Performance Evaluation of Hyperthermia Equipment," AAPM Hyperthermia Task Group #1 (1989)

No. 27 "Hyperthermia Treatment Planning," AAPM Hyperthermia Committee Task Group #2 (1989)

No. 28 "Quality Assurance Methods and Phantoms for Magnetic Resonance Imaging," AAPM Nuclear Magnetic Resonance Committee Task Group #1, Reprinted from *Medical Physics*, Vol. 17, Issue 2 (1990)

No. 29 "Equipment Requirements and Quality Control for Mammography," AAPM Diagnostic X-Ray Imaging Committee Task Group #7 (1990)

No. 30 "E-Mail and Academic Computer Networks," AAPM Computer Committee Task Group #1 (1990)

No. 31 "Standardized Methods for Measuring Diagnostic X-Ray Exposures," AAPM Diagnostic X-Ray Imaging Committee Task Group #8 (1991)

No. 32 "Clinical Electron-Beam Dosimetry," AAPM Radiation Therapy Committee Task Group #25, Reprinted from *Medical Physics*, Vol. 18, Issue 1 (1991)

No. 33 "Staffing Levels and Responsibilities in Diagnostic Radiology," AAPM Diagnostic X-Ray Imaging Committee Task Group #5 (1991)

No. 34 "Acceptance Testing of Magnetic Resonance Imaging Systems," AAPM Nuclear Magnetic Resonance Task Group #6, Reprinted from *Medical Physics*, Vol. 19, Issue 1 (1992)

No. 35 "Recommendations on Performance Characteristics of Diagnostic Exposure Meters," AAPM Diagnostic X-Ray Imaging Task Group #6, Reprinted from *Medical Physics*, Vol. 19, Issue 1 (1992)

No. 36 "Essentials and Guidelines for Hospital Based Medical Physics Residency Training Programs," AAPM Presidential AD Hoc Committee (1992)

No. 37 "Auger Electron Dosimetry," AAPM Nuclear Medicine Committee Task Group #6, Reprinted from *Medical Physics*, Vol. 19, Issue 1 (1993)

No. 38 "The Role of the Physicist in Radiation Oncology," Professional Information and Clinical Relations Committee Task Group #1 (1993)

No. 39 "Specification and Acceptance Testing of Computed Tomography Scanners," Diagnostic X-Ray Imaging Committee Task Group #2 (1993)

No. 40 "Radiolabeled Antibody Tumor Dosimetry," AAPM Nuclear Medicine Committee Task Group #2, Reprinted from *Medical Physics*, Vol. 20, Issue 2, Part 2 (1993)

No. 41 "Remote Afterloading Technology," Remote Afterloading Technology Task Group #41 (1993)

No. 42 "The Role of the Clinical Medical Physicist in Diagnostic Radiology," Professional Information and Clinical Relations Committee Task Group #2 (1994)

No. 43 "Quality Assessment and Improvement of Dose Response Models," (1993).

No. 44 "Academic Program for Master of Science Degree in Medical Physics," AAPM Education and Training of Medical Physicists Committee (1993)

No. 45 "Management of Radiation Oncology Patients with Implanted Cardiac Pacemakers," AAPM Task Group #4, Reprinted from *Medical Physics*, Vol. 21, Issue 1 (1994)

No. 46 "Comprehensive QA for Radiation Oncology," AAPM Radiation Therapy Committee Task Group #40, Reprinted from *Medical Physics*, Vol. 21, Issue 6 (1994)

No. 47 "AAPM Code of Practice for Radiotherapy Accelerators," AAPM Radiation Therapy Task Group #45, Reprinted from *Medical Physics*, Vol. 21, Issue 7 (1994)

No. 48 "The Calibration and Use of Plane-Parallel Ionization Chambers for Dosimetry of Electron Beams," AAPM Radiation Therapy Committee Task Group #39, Reprinted from *Medical Physics*, Vol. 21, Issue 8 (1994)

No. 49 "Dosimetry of Auger-Electron-Emitting Radionuclides," AAPM Nuclear Medicine Task Group #6, Reprinted from *Medical Physics*, Vol. 21, Issue 12 (1994)

No. 50 "Fetal Dose from Radiotherapy with Photon Beams," AAPM Radiation Therapy Committee Task Group #36, Reprinted from *Medical Physics*, Vol. 22, Issue 1 (1995)

No. 51 "Dosimetry of Interstitial Brachytherapy Sources," AAPM Radiation Therapy Committee Task Group #43, Reprinted from *Medical Physics*, Vol. 22, Issue 2 (1995)

No. 52 "Quantitation of SPECT Performance," AAPM Nuclear Medicine Committee Task Group #4, Reprinted from *Medical Physics*, Vol. 22, Issue 4 (1995)

No. 53 "Radiation Information for Hospital Personnel," AAPM Radiation Safety Committee (1995)

No. 54 "Stereotactic Radiosurgery," AAPM Radiation Therapy Committee Task Group #42 (1995)

No. 55 "Radiation Treatment Planning Dosimetry Verification," AAPM Radiation Therapy Committee Task Group #23 (1995), $48, (Includes 2 disks, ASCII format).

No. 56 "Medical Accelerator Safety Considerations," AAPM Radiation Therapy Committee Task Group #35, Reprinted from *Medical Physics*, Vol. 20, Issue 4 (1993)

No. 57 "Recommended Nomenclature for Physical Quantities in Medical Applications of Light," AAPM General Medical Physics Committee Task Group #2 (1996)

No. 58 "Managing the Use of Fluoroscopy in Medical Institutions," AAPM Radiation Protection Committee Task Group #6 (1998)

No. 59 "Code of Practice for Brachytherapy Physics," AAPM Radiation Therapy Committee Task Group #56, Reprinted from *Medical Physics*, Vol. 24, Issue 10 (1997)

No. 60 "Instrumentation Requirements of Diagnostic Radiological Physicists," AAPM Diagnostic X-Ray Committee Task Group #4 (1998)

No. 61 "High Dose Brachytherapy Treatment Delivery," AAPM Radiation Therapy Committee Task Group #59, Reprinted from *Medical Physics*, Vol. 25, Issue 4 (1998)

No. 62 "Quality Assurance for Clinical Radiotherapy Treatment Planning," AAPM Radiation Therapy Committee Task Group #53, Reprinted from *Medical Physics*, Vol. 25, Issue 10 (1998)

No. 63 "Radiochromic Film Dosimetry," AAPM Radiation Therapy Committee Task Group #55, Reprinted from *Medical Physics*, Vol. 25, Issue 11 (1998)

No. 64 "A Guide to the Teaching Of Clinical Radiological Physics To Residents in Diagnostic and Therapeutic Radiology," Revision of AAPM Report #11, AAPM Committee on the Training of Radiologists (January 1999)

No. 65 "Real-Time B-Mode Ultrasound Quality Control Test Procedures," AAPM Ultrasound Task Group #1, Reprinted from *Medical Physics*, Vol. 25, Issue 8 (1998)

No. 66 "Intravascular Brachytherapy Physics," AAPM Radiation Therapy Committee Task Group #60, Reprinted from *Medical Physics,* Vol. 26, Issue 2 (1999)

No. 67 "Protocol for Clinical Reference Dosimetry of High-Energy Photon and Electron Beams," AAPM Task Group #51, Reprinted from *Medical Physics,* Vol. 26, Issue 9 (1999)

No. 68 "Permanent Prostate Seed Implant Brachytherapy," AAPM Medicine Task Group #64, Reprinted from *Medical Physics,* Vol. 26, Issue 10 (1999)

No. 69 "Recommendations of the AAPM on 103Pd Interstitial Source Calibration and Dosimetry: Implications for Dose Specification and Prescription," Report of the Low Energy Interstitial Brachytherapy Dosimetry Subcommittee of the Radiation Therapy Committee, Reprinted from *Medical Physics,* Vol. 27, Issue 4 (2000)

No. 70 "Cardiac Catherization Equipment Performance," AAPM Task Group #17 Diagnostic X-ray Imaging Committee (February 2001)

No. 71 "A Primer for Radioimmunotherapy and Radionuclide Therapy," AAPM Task Group #7 Nuclear Medicine Committee (April 2001)

No. 72 "Basic Applications of Multileaf Collimators," AAPM Task Group #50 Radiation Therapy Committee (July 2001)

No. 73 "Medical Lasers: Quality Control, Safety, Standards, and Regulations," Joint Report of Task Group #6 AAPM General Medical Physics Committee and ACMP (July 2001)

No. 74 "Quality Control in Diagnostic Radiology," Report of AAPM Task Group 12, Diagnostic X-ray Imaging Committee (2002)

No. 75 "Clinical Use of Electronic Portal Imaging," AAPM Radiation Therapy Committee Task Group #58. Reprinted from *Medical Physics,* Vol. 28, Issue 5 (2001)

No. 76 "AAPM Protocol for 40-300 kV X-ray Beam Dosimetry in Radiotherapy and Radiobiology," AAPM Radiation Therapy Committee Task Group #61. Reprinted from *Medical Physics,* Vol. 28, Issue 6 (2001)

No. 77 "Practical Aspects of Functional MRI," AAPM NMR Task Group #8. Reprinted from *Medical Physics,* Vol. 29, Issue 8 (2002)

No. 78 "Proton Magnetic Resonance Spectroscopy in the Brain: Report of AAPM Magnetic Resonance Task Group #9." Reprinted from *Medical Physics,* Vol. 29, Issue 9 (2002)

No. 79 "Academic Program Recommendations For Graduate Degrees In Medical Physics," Revision of AAPM Report No. 44. AAPM Education and Training of Medical Physicists Committee (2002)

No. 80 "The Solo Practice of Medical Physics in Radiation Oncology: Report of TG #1 of the AAPM Professional Information and Clinical Relations Committee" (2003)

No. 81 "Dosimetric Considerations for Patients with Hip Prostheses Undergoing Pelvic Irradiation: Report of the AAPM Radiation Therapy Committee Task Group 63," Reprinted from *Medical Physics*, Vol. 30, Issue 6 (2003)

No. 82 "Guidance Document on Delivery, Treatment Planning, and Clinical Implementation of IMRT: Report of the IMRT subcommittee of the AAPM Radiation Therapy Committee," Reprinted from *Medical Physics*, Vol. 30, Issue 8 (2003)

No. 83 "Quality Assurance for Computed-Tomography Simulators and the Computed-Tomography-Simulation Process: Report of the AAPM Radiation Therapy Committee Task Group No. 66," Reprinted from *Medical Physics*, Vol. 30, Issue 10 (2003)

No. 84 "A Revised AAPM Protocol for Brachytherapy Dose Calculations (Update of AAPM TG 43; Report No. 51)," Report of the Low Energy Interstitial Brachytherapy Subcommittee of the Radiation Therapy Committee, Reprinted from *Medical Physics*, Vol. 31, Issue 3 (2004)

No. 85 "Tissue Inhomogeneity Corrections for Megavoltage Photon Beams," AAPM Task Group #65 Radiation Therapy Committee (July 2004)